

# **A Two Dimensional Model of a Direct Propane Fuel Cell with an Interdigitated Flow Field**

**Hamidreza Khakdaman**

Thesis submitted to the  
Faculty of Graduate and Postdoctoral Studies  
In partial fulfillment of the requirements for the degree of

**Doctor of Philosophy**

In  
**Department of Chemical and Biological Engineering  
Faculty of Engineering  
UNIVERSITY OF OTTAWA**

© Hamidreza Khakdaman, Ottawa, Canada, 2012

## ABSTRACT

Increasing environmental concerns as well as diminishing fossil fuel reserves call for a new generation of energy conversion technologies. Fuel cells, which convert the chemical energy of a fuel directly to electrical energy, have been identified as one of the leading alternative energy conversion technologies. Fuel cells are more efficient than conventional heat engines with minimal pollutant emissions and superior scalability. Proton Exchange Membrane Fuel Cells (PEMFCs) which produce electricity from hydrogen have been widely investigated for transportation and stationary applications.

The focus of this study is on the Direct Propane Fuel Cell (DPFC), which belongs to the PEMFC family, but consumes propane instead of hydrogen as feedstock. A drawback associated with DPFCs is that the propane reaction rate is much slower than that of hydrogen. Two ideas were suggested to overcome this issue: (i) operating at high temperatures (150-230°C), and (ii) keeping the propane partial pressure at the maximum possible value. An electrolyte material composed of zirconium phosphate (ZrP) and polytetrafluoroethylene (PTFE) was suggested because it is an acceptable proton conductor at high temperatures. In order to keep the propane partial pressure at the maximum value, interdigitated flow-fields were chosen to distribute propane through the anode catalyst layer.

In order to evaluate the performance of a DPFC which operates at high temperature and uses interdigitated flow-fields, a computational approach was chosen. Computational Fluid Dynamics (CFD) was used to create two 2-D mathematical models for DPFCs based on differential conservation equations. Two different approaches were investigated to model species transport in the electrolyte phase of the anode and cathode catalyst layers and the membrane layer. In the first approach, the migration phenomenon was assumed to be the only mechanism of proton transport. However, both migration and diffusion phenomena were considered as mechanisms of species transport in the second approach. Therefore, Ohm's law was used in the first approach and concentrated solution theory (Generalized Stefan-Maxwell equations) was used for the second one. Both models are isothermal.

The models were solved numerically by implementing the partial differential equations and the boundary conditions in FreeFEM<sup>++</sup> software which is based on Finite Element Methods. Programming in the C<sup>++</sup> language was performed and the existing library of C<sup>++</sup> classes and tools in FreeFEM<sup>++</sup> were used. The final model contained 60 pages of original code, written specifically for this thesis.

The models were used to predict the performance of a DPFC with different operating conditions and equipment design parameters. The results showed that using a specific combination of interdigitated flow-fields, ZrP-PTFE electrolyte having a proton conductivity of 0.05 S/cm, and operating at 230°C and 1 atm produced a performance (polarization curve) that was (a) far superior to anything in the DPFC published literature, and (b) competitive with the performance of direct methanol fuel cells. In addition, it was equivalent to that of hydrogen fuel cells at low current densities (30 mA/cm<sup>2</sup>).

## **STATEMENT OF CONTRIBUTIONS OF COLLABORATORS**

I hereby declare that I am the sole author of this thesis. I have performed the mathematical modeling, computer programming, and data analysis and I have written all of the chapters contained in this thesis.

My supervisors, Dr. Marten Ternan in the Department of Chemical and Biological Engineering and Prof. Yves Bourgault in the Department of Mathematics and Statistics at the University of Ottawa have provided excellent collaboration and guidance throughout this research. They also contributed with essential editorial comments.

## ACKNOWLEDGEMENTS

I am grateful to my PhD supervisor, Dr. Marten Ternan, for giving me the opportunity to learn and expand my knowledge in chemical engineering, and more specifically, in the field of fuel cells. His vast fundamental knowledge, attention to details, guidance and enthusiasm were essential to develop a complex mathematical model. He has been more than a research supervisor, and I have thoroughly enjoyed my interaction with him during our regular weekly meetings. He inspired me in several aspects of my personal life too. I hope to carry forward the lessons I learnt from Dr. Ternan.

I am thankful to my co-supervisor, Prof. Yves Bourgault, for teaching me the concepts of the finite element methods, computational fluid dynamics and numerical methods. I am proud to be among the few chemical engineers who have the opportunity to be supervised by a knowledgeable mathematician who has a deep understanding of chemical engineering processes and fluid dynamics. He has been always present in our regular weekly meetings.

I am appreciative of Dr. Elena Baranova for giving me the opportunity to attend her electrochemistry course and to visit her electrochemistry laboratories. The course, lab tours and discussions had a great impact on my understanding of electrochemistry.

I would like to thank my colleague in the fuel cell group, Mrs. Amani Al-Othman, for spending considerable amount of her time to teach me how to make proton exchange membranes in our fuel cell laboratory. Furthermore, I gained a lot of insight for my modeling work during our discussions about her experiments.

I am thankful to my officemate, Dr. Jan Haelssig, for his inputs on my research. I reaped the benefit of his great knowledge of mathematical modeling during our discussions.

I express my gratitude to each of the professors in my thesis committee for taking the time to review this dissertation and for their suggestions.

Finally, financial assistance from the Canadian federal government's Natural Sciences and Engineering Research Council and also from the Ontario Fuel Cell Research and Innovation Network (OFCRIN) are sincerely acknowledged. This dissertation would not have been produced without their financial support

## **DEDICATION**

To my wife, Shabnam Salimi, for her company, motivations and patience during my professional career as well as the PhD studies.

To my parents for giving me all great opportunities.

To my son, Faraz, for giving me energy and hope.

# TABLE OF CONTENTS

ABSTRACT .....	ii
STATEMENT OF CONTRIBUTIONS OF COLLABORATORS .....	iv
ACKNOWLEDGEMENTS.....	v
DEDICATION.....	vii
TABLE OF CONTENTS.....	viii
LIST OF TABLES .....	xii
LIST OF FIGURES.....	xiii
CHAPTER 1 .....	1
INTRODUCTION .....	1
1.1. Background and Motivation.....	2
1.2. Research Objective .....	3
1.3. Organization of the Thesis .....	4
1.4. References .....	7
CHAPTER 2 .....	8
LITERATURE REVIEW .....	8
2.1. Fuel Cells .....	8
2.2. PEM Fuel Cell's Components.....	9
2.2.1. Electrolyte Membrane.....	9
2.2.2. Catalyst Layers .....	10
2.2.3. Bi-polar Plates .....	10
2.2.4. Gas Diffusion Layers .....	12
2.3. Hydrogen PEM Fuel Cell's Performance .....	12
2.4. Direct Hydrocarbon Fuel Cells.....	14
2.5. Fuel Cell Models .....	17

2.5.1. Electrolyte Modeling.....	22
2.5.2. Gas Diffusion Layer Modeling.....	24
2.5.3. Catalyst Layer Modeling.....	25
2.5.4. Gas Channel Modeling.....	27
2.6. Nomenclature .....	27
2.7. References .....	29
CHAPTER 3.....	32
DIRECT PROPANE FUEL CELL ANODE WITH INTERDIGITATED FLOW FIELDS: TWO-DIMENSIONAL MODEL .....	32
3.1. Introduction .....	33
3.2. Mathematical Model.....	38
3.3. Computational Method .....	43
3.4. Results and Discussion .....	44
3.5. Conclusion.....	50
3.6. Acknowledgement .....	51
3.7. Nomenclature .....	51
3.8. References .....	53
CHAPTER 4.....	56
COMPUTATIONAL MODELING OF A DIRECT PROPANE FUEL CELL .....	56
4.1. Introduction .....	57
4.2. Model Development .....	59
4.2.1. Governing equations .....	59
4.2.2. Boundary conditions .....	65
4.2.3. Model input parameters.....	67
4.2.4. Numerical procedure.....	68

4.2.5. Model Validation .....	69
4.3. Results and discussion .....	72
4.4. Conclusion.....	81
4.5. Acknowledgements .....	81
4.6. Nomenclature .....	81
4.7. References .....	84
CHAPTER 5 .....	87
MATHEMATICAL MODELING OF PROTON AND WATER TRANSPORT IN THE ELECTROLYTE PHASE OF DIRECT PROPANE FUEL CELLS.....	87
5.1. Introduction .....	88
5.2. Model development .....	90
5.2.1. Governing equations .....	92
5.2.2. Numerical procedure.....	98
5.2.3. Input parameters .....	100
5.2.4. Model Validation .....	102
5.3. Results and discussion .....	103
5.4. Conclusions .....	111
5.5. Acknowledgements .....	111
5.6. Nomenclature: .....	112
5.7. References .....	114
CHAPTER 6 .....	117
GLOBAL SUMMARY AND ANALYSIS .....	117
6.1. Model for the Anode.....	117
6.2. Fuel Cell Model, Simple Approach .....	119
6.3. Fuel Cell Model, Rigorous Approach.....	121

CHAPTER 7 .....	124
CONCLUDING REMARKS.....	124
7.1. Conclusions .....	124
7.2. Contribution to Knowledge.....	126
7.3. Recommendations .....	127
APPENDIX .....	129

## LIST OF TABLES

<b>Table 2.1.</b> Complementary equations required in different layers of a PEM fuel cell.....	21
<b>Table 3.1.</b> LHV energy densities of fuels [3].....	34
<b>Table 3.2.</b> List of equations for the Anode Catalyst Layer (ACL) .....	40
<b>Table 3.3.</b> List of boundary conditions for the Anode Catalyst Layer .....	42
<b>Table 3.4.</b> Numerical values used in computation .....	44
<b>Table 3.5.</b> Correlation for binary diffusion coefficient [28] .....	45
<b>Table 3.6.</b> Summary of various cases .....	46
<b>Table 4.1.</b> List of equations for the anode .....	59
<b>Table 4.2.</b> List of equations for the cathode .....	60
<b>Table 4.3.</b> Parameters for Eq. (4-4) [10] .....	61
<b>Table 4.4.</b> List of boundary conditions for the modeling domain .....	64
<b>Table 4.5.</b> Operational, electrochemical and design parameters for simulations .....	65
<b>Table 5.1.</b> List of equations.....	97
<b>Table 5.2.</b> Operational, electrochemical and design parameters for simulations .....	101

# LIST OF FIGURES

<b>Figure 1.1.</b> The Canadian fuel cell market focus [2].....	2
<b>Figure 2.1.</b> Schematic of a PEMFC showing the various components of the cell.....	9
<b>Figure 2.2.</b> Serpentine flow-fields. The concentration of the reactants decreases along the reaction path .....	11
<b>Figure 2.3.</b> Interdigitated flow-fields. Two separate sets of channels prevent mixing of reactants and products.....	11
<b>Figure 2.4.</b> Generalized polarization curve for a fuel cell.....	13
<b>Figure 2.5.</b> A 3-D schematic of a DPFC showing interdigitated flow-fields at the anode bi-polar plate. A 2-D schematic of the anode bi-polar plate along the dashed line is pictured in Figure 2.6 .....	16
<b>Figure 2.6.</b> A 2-D cross sectional view of a DPFC showing the connection of the feed channel (in red) and the product channel (in blue) through the catalyst layers.....	16
<b>Figure 2.7.</b> Modeling domain and existing phases at the anode, cathode and membrane layers of a DPFC .....	20
<b>Figure 2.8.</b> Parameters that must be solved for in a mathematical model.....	21
<b>Figure 3.1.</b> Polarization curves for direct propane fuel cells. The open squares (Nafion electrolyte) and open triangles (polybenzimidazole-H <sub>2</sub> SO <sub>4</sub> electrolyte) data were measured at 95°C [9]. The solid circles (aqueous H <sub>3</sub> PO <sub>4</sub> electrolyte) data were measured at 150°C [12].....	36
<b>Figure 3.2.</b> Schematic of a PEM fuel cell with interdigitated flow field: cross-sectional view showing the modeling domain.....	38
<b>Figure 3.3.</b> Boundaries in the Anode Catalyst Layer of the fuel cell.....	41
<b>Figure 3.4.</b> Contour lines of constant pressure in the anode catalyst layer for Case 2 in Table 3.6 .....	45
<b>Figure 3.5.</b> Anode overpotential for a direct propane fuel cell operating at 150°C. Psfogiannakis et al. [10] reported the dashed line for a platinum anode catalyst and an aqueous PAFC electrolyte. The solid line was generated in this work for a platinum anode catalyst and a zirconium phosphate electrolyte. ....	47
<b>Figure 3.6.</b> Fractional conversion of propane in the anode of a direct hydrocarbon fuel cell versus residence time [s] in the anode catalyst layer. ....	48

<b>Figure 3.7.</b> Pressure gradient [kPa/mm] and anode overpotential [V] as a function of the thickness of the ACL (anode catalyst layer) [ $\mu\text{m}$ ].	49
<b>Figure 3.8.</b> Electrical potential profile in the electrolyte phase of the anode catalyst layer	50
<b>Figure 4.1.</b> A direct propane fuel cell with interdigitated flow field	60
<b>Figure 4.2.</b> Modeling domain containing anode and cathode catalyst layers and electrolyte layer	60
<b>Figure 4.3.</b> Boundaries in the modeling domain	65
<b>Figure 4.4.</b> Polarization curves of direct propane/oxygen fuel cell using Pt anode and cathode. (a) experimental results [21] using Nafion 117 at 95°C. (b) experimental results [9] using 95% $\text{H}_3\text{PO}_4$ at 200°C. (c) experimental results [9] using $\text{H}_2\text{SO}_4$ doped PBI at 95°C (d). The present model results for a solid ZrP-PTFE electrolyte at 150°C; the base case-study	70
<b>Figure 4.5.</b> Polarization curves of direct propane/oxygen fuel cell showing model results for catalyst thickness of 300 microns at different land widths.	72
<b>Figure 4.6.</b> Polarization curves of direct propane/oxygen fuel cell showing model results for the land width of 4 mm at different catalyst thicknesses.	73
<b>Figure 4.7.</b> Potential profile for the ZrP phase within the cathode and anode catalyst layers and membrane layer	74
<b>Figure 4.8.</b> Potential profiles in the y-direction for the ZrP and Pt/C phases located at the middle of the domain x-direction for the cathode and anode catalyst layers and membrane layer. The arrows point in the direction of the ordinate scale that applies to each of the three curves	75
<b>Figure 4.9.</b> Overpotential profile at the anode and cathode	77
<b>Figure 4.10.</b> (a) Protonic current from anode to cathode in electrolyte phase. The vectors length indicate the current magnitude which varies from 0 to 120 $\text{mA cm}^{-2}$ in this case. (b) Electronic current from cathode to anode in electrolyte phase. The vectors length indicate the current magnitude which varies from 0 to $2\text{e}^{-14}$ $\text{mA cm}^{-2}$ in the same case as Figure 4.10 a.	78
<b>Figure 4.11.</b> Propane and oxygen mole fraction at the anode and cathode respectively	79
<b>Figure 4.12.</b> Velocity vectors showing movement of fluid in the anode and cathode catalyst layers.	80
<b>Figure 4.13.</b> Propane conversion at different anode and cathode land widths	80
<b>Figure 5.1.</b> A 3-D schematic of a DPFC showing interdigitated flow-fields at the anode bi-polar plate	91

<b>Figure 5.2.</b> Boundaries in the modeling domain .....	91
<b>Figure 5.3.</b> Modeling procedure.....	98
<b>Figure 5.4.</b> Polarization curves of direct propane/oxygen fuel cell using Pt anode and cathode; (a) experimental results [31] using Nafion 117 at 95°C; (b) experimental results [32] using 95% H <sub>3</sub> PO <sub>4</sub> at 200°C; (c) the present proton migration and diffusion model results for a solid ZrP-PTFE electrolyte at 150°C. ....	102
<b>Figure 5.5.</b> (a) Proton concentration in the electrolyte phase of the anode, membrane and cathode layers; (b) Electrical potential profile for the electrolyte phase of the anode, membrane and cathode layers; (c) Protonic flux from anode to cathode in the electrolyte phase (The vectors length indicate the flux magnitude which varies from 0 to 17 mA cm <sup>-2</sup> in this case). ....	104
<b>Figure 5.6.</b> Electronic flux from anode to cathode in electrolyte phase. The vectors length indicate the flux magnitude which varies from 0 to 1×10 <sup>-11</sup> mA cm <sup>-2</sup> in the same case as Figure 5.5c. ....	105
<b>Figure 5.7.</b> Electrical potential profiles in the y-direction for the electrolyte and catalyst phases located at the middle of the domain x-direction for the cathode and anode catalyst layers and membrane layer. The arrows point in the direction of the ordinate scale that applies to each of the three curves; (a) Proton migration and diffusion within the electrolyte phase [the present model]; (b) Proton migration only within the electrolyte phase [5]. ....	106
<b>Figure 5.8.</b> Overpotential profile in the anode and cathode along y-axis at the middle of the modeling domain. Solid lines (migration and diffusion). Dashed lines (migration only) [5]. ....	107
<b>Figure 5.9.</b> Propane mole fraction in the gas phase of the anode catalyst layer along the x-direction at the middle of the anode catalyst layer (a) Proton migration and diffusion within the electrolyte phase [the present model] (b) Proton migration only within the electrolyte phase [5]. ....	108
<b>Figure 5.10.</b> Modeling results for polarization curves of direct propane/oxygen fuel cells using a solid ZrP-PTFE electrolyte at 150°C. (a) Proton migration and diffusion within the electrolyte phase [the present model] (b) Proton migration only within the electrolyte phase [5]. ....	109
<b>Figure 5.11.</b> (a), (b) and (c) predicted polarization curves for a direct propane/oxygen fuel cell at different operating temperatures, (d) experimental data for a typical hydrogen/oxygen PEMFC [35], (e) experimental data for the best performed DPFC at 200°C [32]. ....	110

# CHAPTER 1

---

## INTRODUCTION

The emerging energy demands in developing countries such as China and India have accelerated the diminishing of fossil fuels. The limited amount of economically accessible crude oil and natural gas has already been a main concern in providing future energy demands. On the other hand, utilizing fossil fuels has led to serious environmental problems such as climate change and pollution. Renewable energy may be considered as the ultimate alternative for fossil fuels if socially acceptable technologies can be developed to produce energy economically. Meanwhile, developing new energy-conversion technologies with higher efficiencies can postpone the depletion of fossil fuels and can reduce environmental issues. Fuel cells are considered as one of the energy-conversion devices that are more efficient than the conventional heat engines. The number of patent publications for fuel cells exceeded any other advanced energy technology, showing a growth of 57% in 2010 [1]. In terms of actual sales, fuel cell units shipped from North America increased fourfold between 2008 and 2010 [1].

The three main fuel cell sectors are stationary power generation (buildings, uninterruptible power supplies, etc.), transportation (cars, material handling, etc.), and small portable devices (laptops, cell phones, etc.). Figure 1.1 indicates the share the main sectors have in the Canadian fuel cell market [2]. About 36% of the Canadian fuel cell market focuses on small and large stationary power generation. The transportation sector represents the second largest market at 29%.

Stationary power generation is the most established application for fuel cells. In the Canadian fuel cell commercialization roadmap [3], several markets have been proposed for stationary fuel cells such as primary and back-up power for telecommunications facilities, remote industrial operations, data centres, wastewater treatment plants, and combined heat and power for public and commercial buildings. Stationary fuel cells are being used in a considerable number of projects in the US, Japan and South Korea [1]. Fuel cell units for combined heat and power

generation have been installed with 400 kW power per unit and an 80,000-hour warranty [1]. The global market for stationary fuel cells is projected at 16 GW for 2011, with a projected value of \$18 billion [3]. In the transportation sector, material handling (lift trucks) demonstrated a growing market along with cost reduction and ease of operation [4].

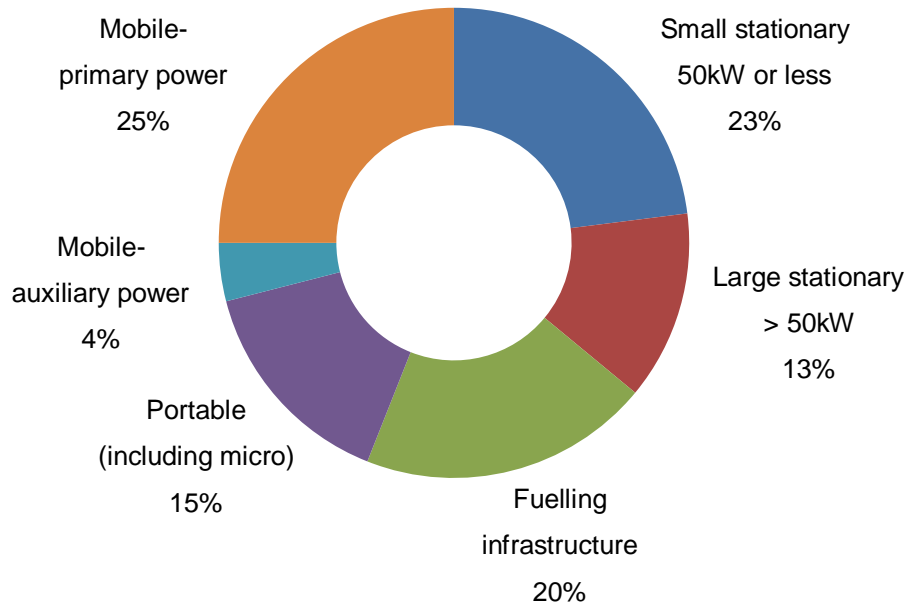


Figure 1.1. The Canadian fuel cell market focus [2]

## 1.1. Background and Motivation

Hydrogen fuel cells are currently the most attractive type of fuel cells because of the unique properties of hydrogen. For instance, the rate of the oxidation reaction for hydrogen is superior to those for other types of fuels. However, cost and durability are the major challenges that hinder the commercialization of all kinds of fuel cells. Nevertheless, hydrogen fuel cells suffer from other disadvantages: fuel processing (hydrogen production), transportation and distribution. Significant capital investment and operational costs for hydrogen production and for infrastructure (hydrogen transport and distribution) are the most pressing problems.

To overcome the fuel processing issues, at least in some fuel cell applications, fuel cells that can be fed by conventional fuels at the anode have been investigated. An extensive effort was made to develop direct hydrocarbon fuel cells during the 1959-1968 period. Three review articles of that period summarized the main achievements and challenges for direct hydrocarbon fuel cells [5-7]. Propane has been identified as one of the most reactive and convenient hydrocarbon fuels [5]. Its distribution infrastructure is already in place. However, the oxidation reaction rate for propane at the anode is several orders of magnitude less than that for hydrogen. Furthermore, during that period all the research projects using direct propane fuel cells (DPFCs) had focused on aqueous electrolytes which are not as convenient for handling as the modern solid electrolytes. These two obstacles were the main reasons for the decreased interest in research on direct propane fuel cells.

The emergence of new materials and methods motivated our research group to try to improve DPFCs. More specifically, Park et al. [8] developed a solid membrane made of zirconium phosphate (ZrP) and polytetrafluoroethylene (PTFE) which showed a high proton conductivity at elevated temperature without dealing with a liquid electrolyte. Moreover, Nguyen [9] developed a nonconventional flow field design, that is now known as interdigitated flow fields. They are able to maintain the propane partial pressure at its maximum value along the entire length of the channel feeding the reaction zone. The high concentration of the reactant (propane) will maximize the propane oxidation reaction at the anode.

## **1.2. Research Objective**

The principal objective of this dissertation is to improve the performance of direct propane fuel cells as an alternative to hydrogen fuel cells, in order to generate power in rural areas. Hydrogen fuel cells have been widely investigated for both transportation and stationary applications. However, hydrogen production and delivery are two of the challenging issues that still postpone the commercialization of hydrogen fuel cells. A possible approach to overcome the fuel processing issue is to develop DPFCs that use propane as the fuel instead of hydrogen.

In support of the principal objective, and in order to speed up the process of improving the performance of DPFCs, a computational model was created. A model based on the mathematical description of physical phenomena occurring in the cell can be used to investigate the prospect of possible improvements. The model can also be used to guide the design of fuel cells before building them and performing experiments. Moreover, it provides insight into the fundamental physical phenomena that govern fuel cell behaviour.

### **1.3. Organization of the Thesis**

This dissertation is presented as a series of articles. The objectives and scope of the work are defined in this chapter, Chapter 1. Chapter 2 includes general topics about fuel cells and fuel cell modeling, while more detailed literature survey has been reported in the papers that have been published or submitted. Chapters 3, 4, and 5 are written in journal article format. Chapter 6 integrates the material addressed in the previous chapters describing the strategy for meeting the primary objective. Chapter 7 presents a brief summary of major contributions to knowledge and suggests some possible research topics for future work.

An isothermal mathematical model for the anode catalyst layer was developed during the first stage of the work. Other parts of the fuel cell, i.e., cathode catalyst layer and the membrane layer were not considered in this preliminary model. The specific objective was to investigate possible improvement in the anodic reaction rate without dealing with a mathematically complex model for the whole fuel cell. The outcome of this step was expected to indicate whether or not DPFCs could be improved in comparison with hydrogen fuel cells.

There are two possible approaches to model the "solid electrolyte phase", i.e., simple approach and rigorous approach. The former has been used in the vast majority of fuel cell models and was also used in this model of the electrolyte phase. In this approach, species transport in the electrolyte phase is described by migration phenomenon only. In other words, electrically charged species such as protons move in the electrolyte phase in response to an electric field (i.e. an electrical potential gradient).

The results showed that a major improvement in the anodic reaction rate is attainable by applying using an interdigitated flow field anode operating at 150°C. The conclusion was that the proposed modified DPFC could be promising as an alternative to hydrogen fuel cells. This investigation was published in a journal paper presented in Chapter 3.

In the second stage of the work, the anode model described in Chapter 3 was expanded to include the entire fuel cell including the three sub-domains, i.e., the anode catalyst layer, the cathode catalyst layer and the membrane layer. Three specific objectives for this development were: to predict the performance of an isothermal DPFCs at different operating conditions, to conduct parametric studies, and to develop a mathematical procedure for sub-domain coupling.

The model, that was developed during this stage of the work, was able to predict polarization curves for a DPFC having interdigitated flow fields, a ZrP-PTFE electrolyte, and an operating temperature of 150°C. The reasonable agreement of the polarization curves indicated that the simple model could be used for overall evaluation of the DPFCs, when polarization curve prediction was the criterion for the validity of the model. However, the simple model was not able to correctly calculate other important variables (overpotential and electrical potential gradient in the electrolyte phase). The reason was attributed to the representation of proton transport by proton migration only and the absence of proton diffusion. Therefore, a more rigorous model that accounted for the proton diffusion phenomena was developed in the last step of the work. The results pertinent to this stage of the research were published in a journal paper presented in Chapter 4.

Although there are problems with migration that were identified in Chapter 4 (the second paper), the problems do not affect polarization curves. Since Chapter 3 (the first paper) did not discuss anything other than polarization curves, the problems identified in Chapter 4 did not have any impact on Chapter 3.

In a more comprehensive model, the transport of ionic species was described in response to both the electrical potential gradient and the concentration gradient. The specific objective for this

stage of the work was to successfully predict the variation of all the desired variables within the fuel cell.

A rigorous approach was employed in order to account for both driving forces involved in proton and water transport in the proton conductor phase, i.e., electrical potential gradient and proton concentration gradient. In this approach, concentrated solution theory was applied by using the generalized Stefan-Maxwell equations. An isothermal model was developed and the results presented in Chapter 5 were submitted to a journal for publication.

The results of the rigorous model showed that the proton flux caused by the electrical potential gradient predicted by the simple models was opposite to the direction known to be correct. Therefore, the electrical potential profile and consequently the overpotential profile in the simple model were incorrect. As the rate of anodic and cathodic reactions are exponential functions of overpotential, a small deviation in overpotential can cause substantial error in the rate of reactions. Consequently, the conversion of propane and oxygen calculated by the simple model had a significant error.

## 1.4. References

- [1] 2010 Fuel Cell Technologies Market Report, Breakthrough Technologies Institute, Inc., Washington, DC. June 2011; <http://www.nrel.gov/docs/fy11osti/51551.pdf>
- [2] The Canadian Hydrogen and Fuel Cell Sector Profile, Industry Canada, 2008; [http://www.ic.gc.ca/eic/site/hfc-hpc.nsf/vwapj/Hydrogenprofile-profilhydrog%C3%A8ne2008\\_eng.pdf/\\$file/Hydrogenprofile-profilhydrog%C3%A8ne2008\\_eng.pdf](http://www.ic.gc.ca/eic/site/hfc-hpc.nsf/vwapj/Hydrogenprofile-profilhydrog%C3%A8ne2008_eng.pdf/$file/Hydrogenprofile-profilhydrog%C3%A8ne2008_eng.pdf)
- [3] Canadian Fuel Cell Commercialization Roadmap, Industry Canada, Dec 2008; [http://www.h2fcc.ca/files/IC\\_FC\\_PDF\\_final.pdf](http://www.h2fcc.ca/files/IC_FC_PDF_final.pdf)
- [4] The U.S. Fuel Cell Council Industry Overview 2010; <http://www.fchea.org/core/import/PDFs/Technical%20Resources/IndustryOverview2010.pdf>
- [5] H.A. Liebhafsky, E.J. Cairns, The direct hydrocarbon fuel cell with aqueous electrolytes, In: Fuel Cells and Fuel Batteries, Wiley, New York, 1968, pp. 458-523.
- [6] J.O. Bockris, S. Srinivasan, Fuel cells: their electrochemistry, In: Electrochemical Combustion of Organic Substances, McGraw-Hill, New York, 1969, pp. 357-411.
- [7] E.J. Cairns, The anodic oxidation of hydrocarbons and the hydrocarbon fuel cell, Adv Electrochem and Electrochem Eng, 8 (1971) 337-391.
- [8] Y. Park, J. Kim, M. Nagai, High proton conductivity in ZrP-PTFE composites, J.Mater.Sci.Lett., 19 (2000) 1735-1738.
- [9] T.V. Nguyen, A gas distributor design for proton-exchange-membrane fuel cells, J.Electrochem.Soc., 143 (1996).

## CHAPTER 2

---

### LITERATURE REVIEW

#### 2.1. Fuel Cells

A fuel cell converts chemical energy of fuels directly into electrical energy. Typically, generation of electricity from fuels involves several energy conversion steps, i.e., fuel combustion, steam generation, conversion of thermal energy to mechanical energy in a heat engine, and finally electricity generation by running a generator. However, a fuel cell can generate electricity in a single step. Several potential advantages have resulted in a vast effort to develop such a device. Potential for an efficient operation, ease of scale-up, variety of fuel sources, and relatively low maintenance cost are some of the expected merits. Fuel cells also have disadvantages that differ from type to type.

One of the most common criteria for categorizing fuel cells is the type of electrolyte membrane they use. Alkaline Fuel Cells (AFC), Polymer Electrolyte Membrane or Proton Exchange Membrane Fuel Cells (PEMFC), Phosphoric Acid Fuel Cells (PAFC), Molten Carbonate Fuel Cells (MCFC), and Solid Oxide Fuel Cells (SOFC) are the main types of fuel cells. Each type has its own applications, merits and demerits.

PEM fuel cells are promising for automotive applications, small-scale distributed stationary power generation and also for portable power applications. PEM fuel cells have drawn the most attention because of their simplicity, quick start-up and various potential applications.

The most conventional PEM fuel cells are fed by hydrogen or methanol at the anode and oxygen or air at the cathode. The electrolyte membrane is a thin (<50 $\mu\text{m}$ ) proton conductive polymer membrane [1]. The catalyst is typically platinum supported on carbon with loadings of about 0.3 mg/cm<sup>2</sup>. Operating temperature is typically between 70 and 85°C.

The following material is divided into three parts. First, conventional PEM fuel cells that use hydrogen as the fuel are described. Direct hydrocarbon fuel cells are the second topic. Fuel cell modeling is discussed in the third part.

## 2.2. PEM Fuel Cell's Components

Figure 2.1 shows different components of a single PEM fuel cell: electrolyte membrane layer, catalyst layers, diffusion layers, and bipolar plates. They are explained in the following sections. The Membrane Electrode Assembly (MEA) is the combination of diffusion layers, catalyst layers, and membrane.

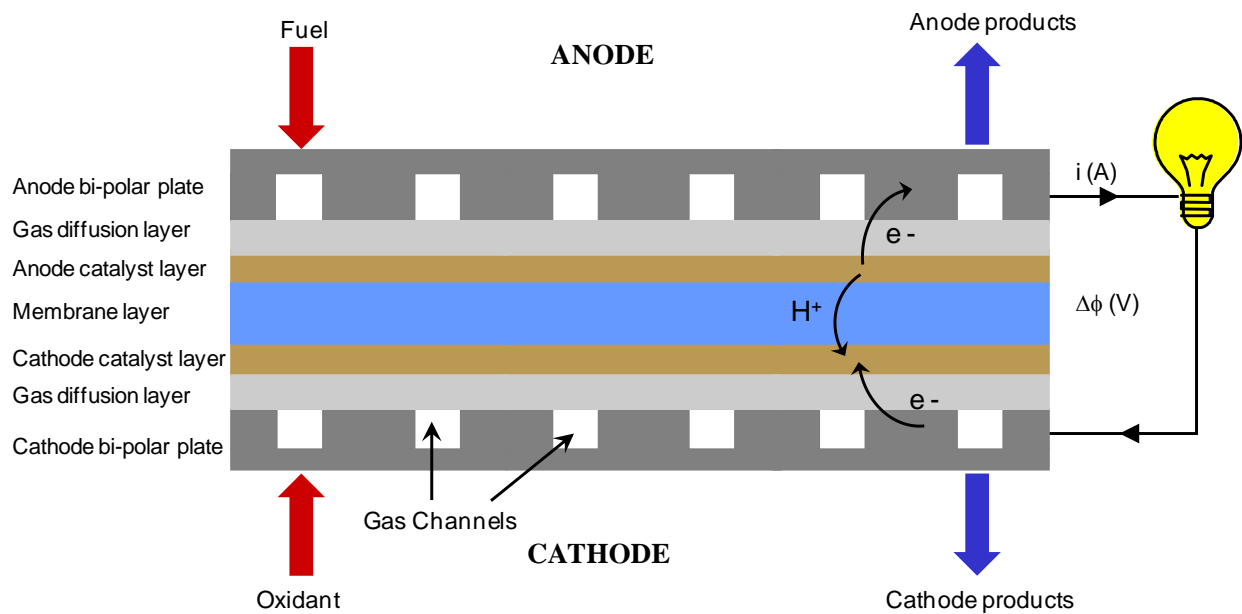


Figure 2.1. Schematic of a PEMFC showing the various components of the cell

### 2.2.1. Electrolyte Membrane

A fuel cell electrolyte membrane must have high proton conductivity, must prevent mixing of gaseous species at the anode with those at the cathode, and must be chemically and mechanically stable at fuel cell operating conditions. Nafion is the membrane used most frequently in PEM

fuel cells. It is made by Dupont. The proton conductivity for Nafion is approximately 0.1 S/cm [2]. In this research, zirconium phosphate/polytetrafluoroethylene (ZrP-PTFE) was chosen to be the electrolyte material because it is capable of operation at greater temperatures than Nafion.

### **2.2.2. Catalyst Layers**

Electrochemical reactions take place at the catalyst layers which are pressed between the membrane and gas diffusion layers in PEMFCs. Since there are three types of species that participate in the electrochemical reactions, i.e., molecules, electrons, and protons, the reactions can only take place at locations where all three species have access to the catalyst layer. Platinum has been used as the catalyst for both hydrogen oxidation and oxygen reduction reactions in PEM fuel cells. Large amounts of platinum catalyst (up to 28 mg/cm<sup>2</sup>) were used during the early stages of PEM fuel cell development [1]. In the late 1990s with the use of catalyst supports this was reduced to 0.3–0.4 mg/cm<sup>2</sup> [1].

### **2.2.3. Bi-polar Plates**

Bi-polar plates consist of an electrically conductive material and gas channels as can be seen in Figure 2.1. The conductive part separates the individual cells in the stack, collects the electrical current, and performs heat management. Gas channels in bi-polar plates are known as flow fields. They distribute fuel and oxidant on the catalyst layers in the fuel cell and remove products. Fuel and oxidant are transported from the gas channels through a gas diffusion layer to the catalyst layers, where they are consumed through an electrochemical reaction. Several types of flow fields have been investigated in the literature: parallel, serpentine, spiral and interdigitated. Each type of flow field has advantages and disadvantages.

Although conventional serpentine flow fields are suitable for hydrogen fuel cells, they have at least one disadvantage for hydrocarbon fuel cells. With serpentine flow fields, the CO<sub>2</sub> formed in the catalyst layer must exit the fuel cell through the same channel that carries the inlet hydrocarbon feed. As a result the concentration of the hydrocarbon feedstock decreases progressively along the length of the channel, as it becomes mixed with progressively more and more CO<sub>2</sub> product (Figure 2.2). In contrast with interdigitated fuel cells, the feedstock enters

through one channel, flows through the catalyst layer (parallel to the electrolyte membrane) where it reacts, and the  $\text{CO}_2$  product leaves through a different channel (Figure 2.3). Thus with interdigitated flow fields the concentration driving force that causes the reactant hydrocarbon to enter the anode catalyst layer can remain large, along the entire length of the channel. Studies of the characteristics of interdigitated flow fields have been reported by Nguyen [3] and Yan et al. [4,5].

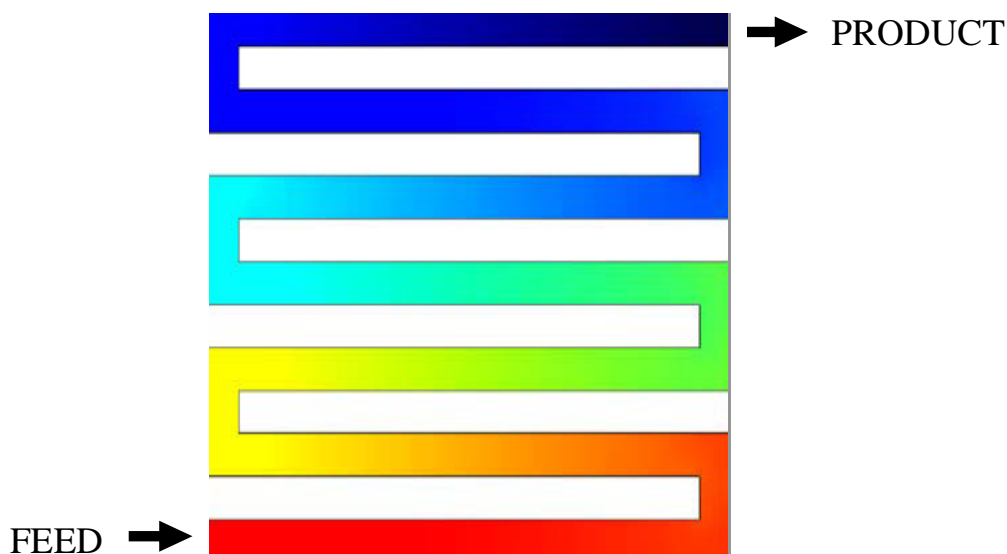


Figure 2.2. Serpentine flow-fields. The concentration of the reactants decreases along the reaction path

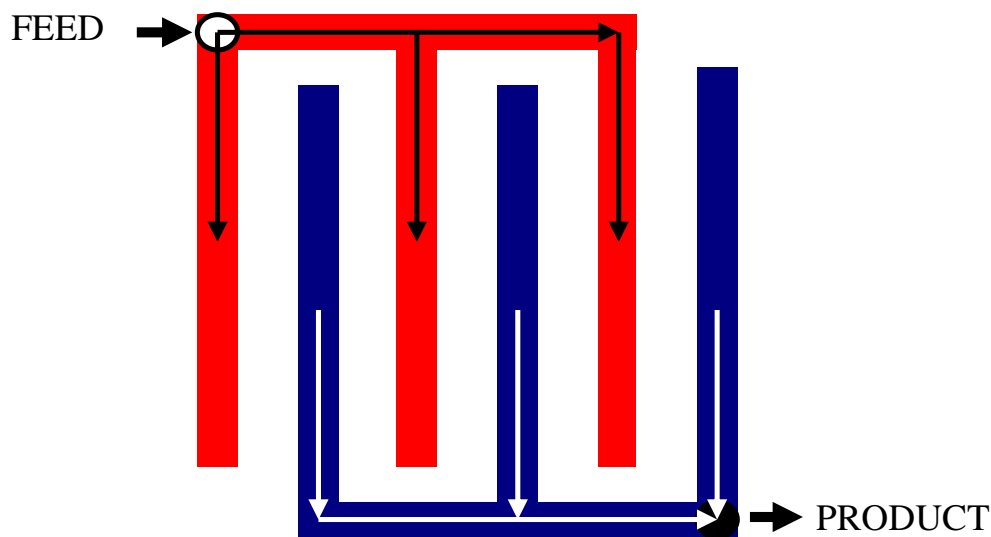


Figure 2.3. Interdigitated flow-fields. Two separate sets of channels prevent mixing of reactants and products

### 2.2.4. Gas Diffusion Layers

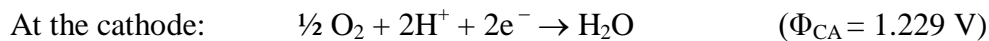
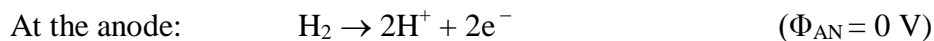
The layer between the catalyst layer and the bipolar plate at the anode and cathode side is called the gas diffusion layer which has the following roles in a PEM fuel cell:

- It distributes reactant gases coming from the gas channels to the entire catalyst layer and not just to that part of the catalyst layer which is adjacent to the channels.
- It provides a pathway for product liquid water from the catalyst layer to the flow field channels
- It electrically connects the catalyst layer to the bipolar plate which allows the electrons to complete the electrical circuit.
- It conducts heat generated in the catalyst layer to the bipolar plate for heat management.

Therefore, the gas diffusion layer must be sufficiently porous to allow the flow of reactants and products through it. It must also be a good electrical and thermal conductor. Carbon fibre paper and woven carbon fabric satisfy such specifications. The thickness of various gas diffusion materials varies between 0.17 to 0.40 mm, and porosity varies between 70% and 80% [1].

### 2.3. Hydrogen PEM Fuel Cell's Performance

The following electrochemical reactions take place in a hydrogen/oxygen fuel cell:



Hydrogen reacts at the catalyst layer of the fuel cell anode electrode to form protons and electrons. Protons travel through the membrane. Electrons flow to the cathode electrode through an external electrical circuit where they perform useful work. The electrons meet the protons that went through the membrane and the oxygen that is fed to the cathode electrode. An electrochemical reaction takes place at the catalyst layer of the cathode electrode to form water. The electrochemical reactions at the anode and cathode take place as long as reactants are fed to the electrodes, and a power consumer draws the electrical current.

If a fuel cell is supplied with reactants, but the electrical circuit is not closed, it will not generate any current. Ideally, the cell potential at this condition would be expected to be equal to the reversible cell potential. However, in practice, this potential, which is called the open circuit voltage (OCV), is considerably lower than the reversible potential (Figure 2.4). Therefore, there are some potential losses in a fuel cell even when no current is being produced. When an electrical circuit containing a resistor is closed, the potential is expected to drop even further as a function of the flowing current. There are different kinds of potential losses in a fuel cell caused by the following factors:

- crossover of reactants
- kinetics of the electrochemical reactions (activation polarization)
- internal electrical and ionic resistance (ohmic polarization)
- mass transfer limitations for the reactants moving to reaction sites, and for the products leaving reaction sites (concentration polarization)

Polarization is the difference between the electrode potential and the equilibrium potential at given temperature, pressure and concentration of reactants. Activation and concentration polarization can occur at both anode and cathode while ohmic polarization occurs in the electrolyte phase.

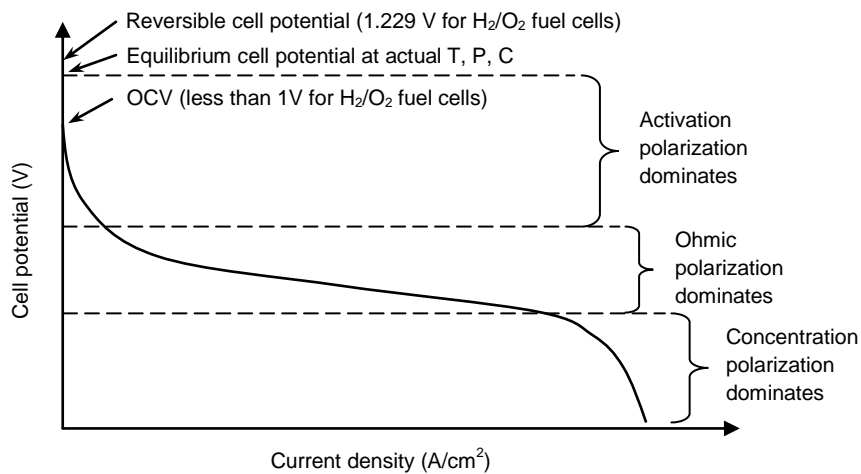


**Figure 2.4. Generalized polarization curve for a fuel cell**

Figure 2.4 shows a typical polarization curve which shows the numerical value of the cell potential at various current densities. Fuel cell performance can be evaluated by recording the polarization curve experimentally.

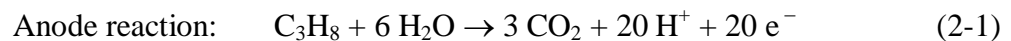
Fuel cell performance (power output) is affected by several parameters that can be classified in two main categories:

- Operating conditions, such as temperature, pressure, feed composition, reactant utilization and current density.
- Design parameters, such as bipolar plate channel size, and thickness and material properties of catalyst and electrolyte layers.

## 2.4. Direct Hydrocarbon Fuel Cells

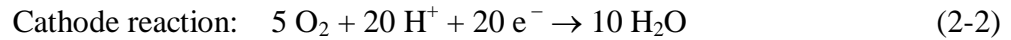
Direct hydrocarbon fuel cells are PEM fuel cells, but they are fed by hydrocarbons instead of hydrogen at their anodes. Liebhafsky and Cairns [6], Bockris and Srinivasan [7], and Cairns [8] have reviewed the majority of fuel cell research in which hydrocarbons have been used as fuel. Different hydrocarbons such as normal paraffin fuel (methane to n-hexadecane), olefins (ethylene, propylene and 1-butene), gasoline and diesel have been investigated as the fuel cell feed. Propane is one of the fuels which is relatively acceptable in reactivity and convenient in application [6].

The electrochemical reactions in a direct propane fuel cell are shown below. For complete conversion at the anode, CO<sub>2</sub> will be the only gaseous species at the anode outlet according to Eq. (2-1). It was assumed that the coke formation did not occur.



In a more realistic case, the products from the anode could include carbon dioxide, methanol, ethanol, propanol, formaldehyde, formic acid, acetaldehyde, acetic acid, propanaldehyde, propanoic acid, and carbon monoxide. However, carbon dioxide has been assumed to be the major product in several previous studies that used a platinum catalyst. If CO<sub>2</sub> is the only product from the anode, the maximum possible electrical current will be obtained from the fuel cell.

Electrons and protons which are produced at the anode catalyst layer through Eq. (2-1) travel by two different paths to reach the cathode catalyst layer. Electrons generate electrical energy as they flow through the external circuit. Protons move through the electrolyte phase (proton conductor phase) to reach the cathode catalyst layer. Protons and electrons reduce oxygen at the cathode catalyst layer as shown in Eq. (2-2)



The overall reaction at a DPFC is shown in Eq. (2-3)



Figure 2.5 shows a three dimensional picture of a DPFC composed of five layers: two bi-polar plates, two catalyst layers, and membrane layer. The interdigitated flow-fields are shown for the anode bi-polar plate. Propane and water are the reactants for the anodic reaction which flow in the feed channels shown in red. CO<sub>2</sub>, un-converted propane and water flow in the product channels which are shown in blue. The gaseous species in the feed channels can reach the product channels by passing through the catalyst phase, as shown in Figure 2.6. This figure provides a two-dimensional cross section of a DPFC along the dashed line in Figure 2.5. The gas diffusion layers, which are common for PEM fuel cells are not used with interdigitated flow-fields. Because the gas diffusion layers provide a route from feed channels to product channels, they will decrease the feed flow rate passing the catalyst layer.

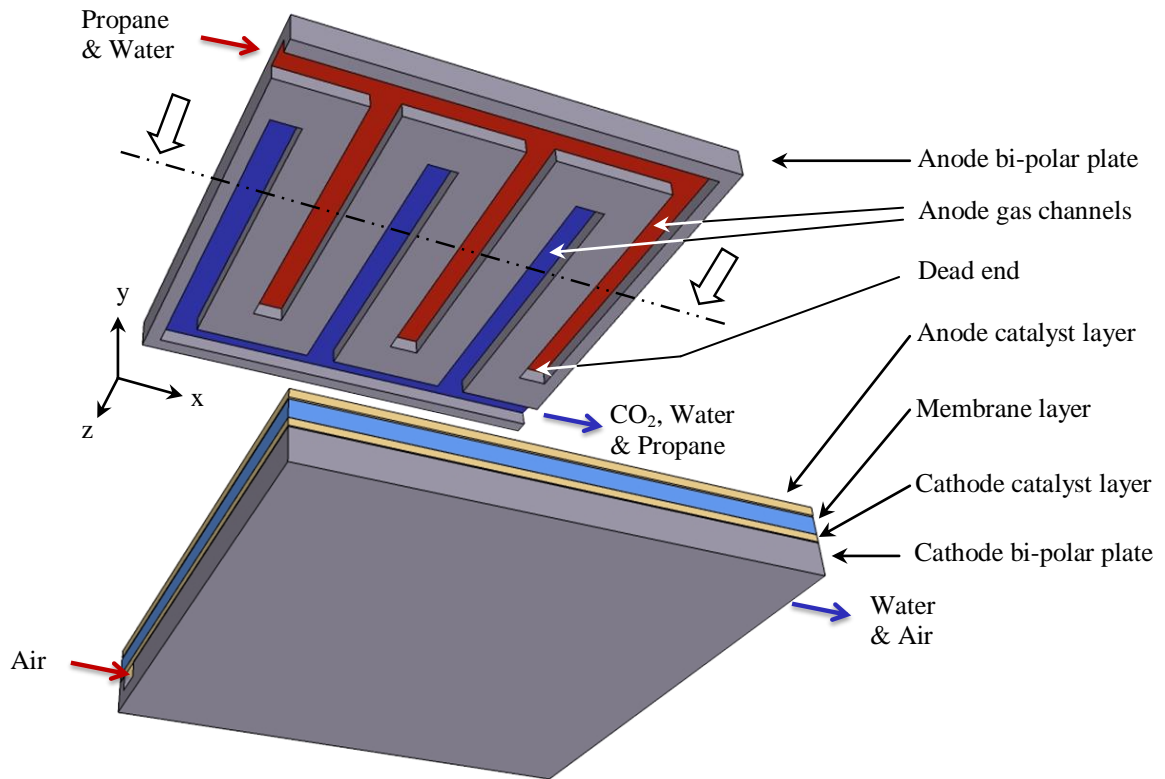


Figure 2.5. A 3-D schematic of a DPFC showing interdigitated flow-fields at the anode bi-polar plate. A 2-D schematic of the anode bi-polar plate along the dashed line is pictured in Figure 2.6

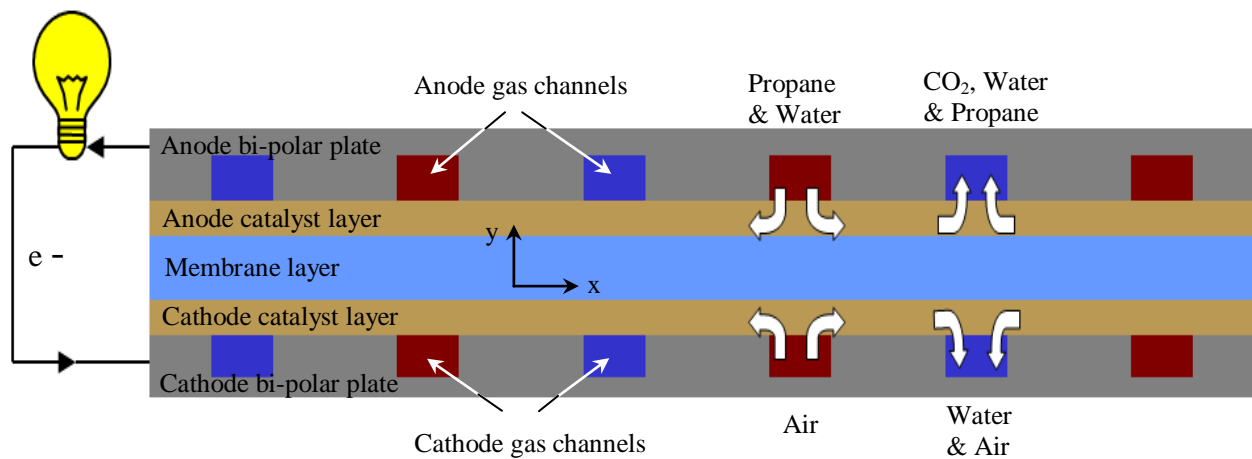


Figure 2.6. A 2-D cross sectional view of a DPFC showing the connection of the feed channel (in red) and the product channel (in blue) through the catalyst layers.

As mentioned before, a serious disadvantage of the DPFCs is that the power generated is very small. This is due to the very slow rate of oxidation reaction at the anode of a DPFC. An attempt to overcome this disadvantage was made through the combination of the following objectives in three PhD projects that are being performed in our research group. The intent is for fuel cell performance to exceed the previously published values:

- 1- Operation at high temperature (150°C). Since the performance of propane fuel cells is limited by the anode catalyst, increasing the temperature is one method of increasing the anode kinetics. This requires an electrolyte that has a reasonable proton conductivity and stability at high temperature. A ZrP-PTFE composite membrane was chosen for this research because it had demonstrated reasonable performance when operated at 120°C in a hydrogen fuel cell [9]. The ZrP-PTFE solid membrane was developed in another project within our group.
- 2- Using interdigitated flow fields. As it was mentioned in section 2.2.3, interdigitated flow fields can permit the concentration driving force of the hydrocarbon reactant at the anode catalyst layer entrance to have large value along the entire length of the channel.
- 3- Using a less expensive catalyst. The conventional anode catalyst, Pt, is needed to resist corrosion when liquid phase water is present. By operating above the boiling point of water, less expensive metals such as nickel were investigated using density functional theory in another project within our group.

## **2.5. Fuel Cell Models**

Mathematical models can play an important role in fuel cell development. An accurate and reliable model can reduce the time needed to understand the real physical and chemical phenomena that are taking place inside the fuel cell. Models can provide valuable information for fuel cell design, optimization, and performance prediction at various operating conditions.

Fuel cell models are split in two main categories, performance models and mechanistic models. The performance models usually fit the experimental data with a single equation to express the potential of a cell versus current density at different operating conditions. The typical form of a

performance model is shown in Eq. (2-4), where the cell potential  $\Phi_{\text{Cell}}$  is a function of open circuit potential  $\Phi_{\text{OCV}}$ , ohmic polarization  $\Delta\Phi_{\text{Ohm}}$ , activation polarization  $\Delta\Phi_{\text{Act}}$ , and concentration polarization  $\Delta\Phi_{\text{Conc}}$ .

$$\Phi_{\text{Cell}} = \Phi_{\text{OCV}} - \Delta\Phi_{\text{Ohm}} - \Delta\Phi_{\text{Act}} - \Delta\Phi_{\text{Conc}} \quad (2-4)$$

The polarization terms are functions of the cell current density and several constant parameters. Various sets of experimental data are required to determine these parameters so that they can be used in Eq. (2-4) for a range of operating conditions. As an example of developing performance models, Kim et al. [10] presented an empirical equation to calculate the cell potential as a function of current density for polymer electrolyte membrane fuel cells. This model is able to predict the cell potential over the entire range of current density (including the mass transfer limiting range), at several temperatures, pressures, and oxygen/inert gas compositions.

The performance models can only be used for existing fuel cells if there are enough experimental data. The disadvantage of the performance models is that they cannot provide fundamental understanding of phenomena occurring inside the cell. This insight is critical to develop new materials, to propose new cell designs or to optimize existing fuel cells.

The principal objective of this research was to be met by developing a mechanistic model because there is not enough experimental data for direct propane fuel cells that use interdigitated flow fields. Furthermore, a new electrolyte material, zirconium phosphate, and non-conventional operating conditions were going to be investigated by this model. Therefore, the rest of Section 2.5 focuses on mechanistic models.

Mechanistic models, which describe fuel cells in detail, can be categorized according to their dimensions. Depending on the target application of the model, it can be a 1-D, 2-D, or 3-D model. Figure 2.5 shows a three-dimensional schematic of a DPFC with interdigitated flow-fields. A 1-D model of interdigitated flow-fields is usually developed along the x- or y-direction, while a 2-D model usually describes the cell in the x-y plane. If the channels are long enough so that the effect of a dead ended channel becomes small, variations along z-direction is negligible

and a 2-D model provides valuable insights. A 3-D model is required to examine the effect of dead ended channels. In serpentine flow-fields, variation along the channels (z-direction) is often significant. Therefore, 3-D models are more common for serpentine flow-fields.

Several one-dimensional mechanistic models were presented to investigate the different layers of fuel cells. Two early models in this area were published by Bernardi and Verbrugge [11] and Springer et al. [12]. Due to the emergence of powerful computers, two and three dimensional models have been developed since the late 1990s and early 2000s.

As shown in Figure 2.1, a typical fuel cell involves seven different layers, i.e., two bipolar plates, two diffusion layers, two catalyst layers for the anode and cathode, and one electrolyte layer. A mechanistic model can consist of a particular single layer [13, 14], several layers [15], or all seven layers [16] regardless of its dimension.

Figure 2.7 shows the modeling domain for interdigitated flow-fields. The symmetry of the interdigitated flow-fields and the need to reduce the computational time were factors that influenced the modeling domain choice: from the middle of a feed channel to the middle of its adjacent product channel. A more detailed picture of the modeling domain is shown on the left hand side of Figure 2.7 demonstrating different phases that exist in the catalyst layers and the membrane layer. Three phases are present in the anode and cathode catalyst layers. Electrochemical reactions take place at the interface between these phases. These three phases are the "gas phase" containing reactants and products, the "solid catalyst phase" containing the carbon support and platinum, and the "solid electrolyte phase". The later consists of stationary zirconium phosphate matrix (ZrP or  $[\text{Zr}(\text{HPO}_4)_2 \cdot \text{H}_2\text{O}]$ ), and species that can move within the ZrP containing mobile  $\text{H}_2\text{O}$  ( $\text{Zr}(\text{HPO}_4)_2 \cdot 2\text{H}_2\text{O}$ ), and  $\text{H}^+$  ( $\text{Zr}(\text{HPO}_4)_2 \cdot \text{H}_3\text{O}^+$ ). The membrane layer is porous PTFE that contains the solid electrolyte phase in its pores. The catalyst phase is an electron conductor and zirconium phosphate is a proton conductor.

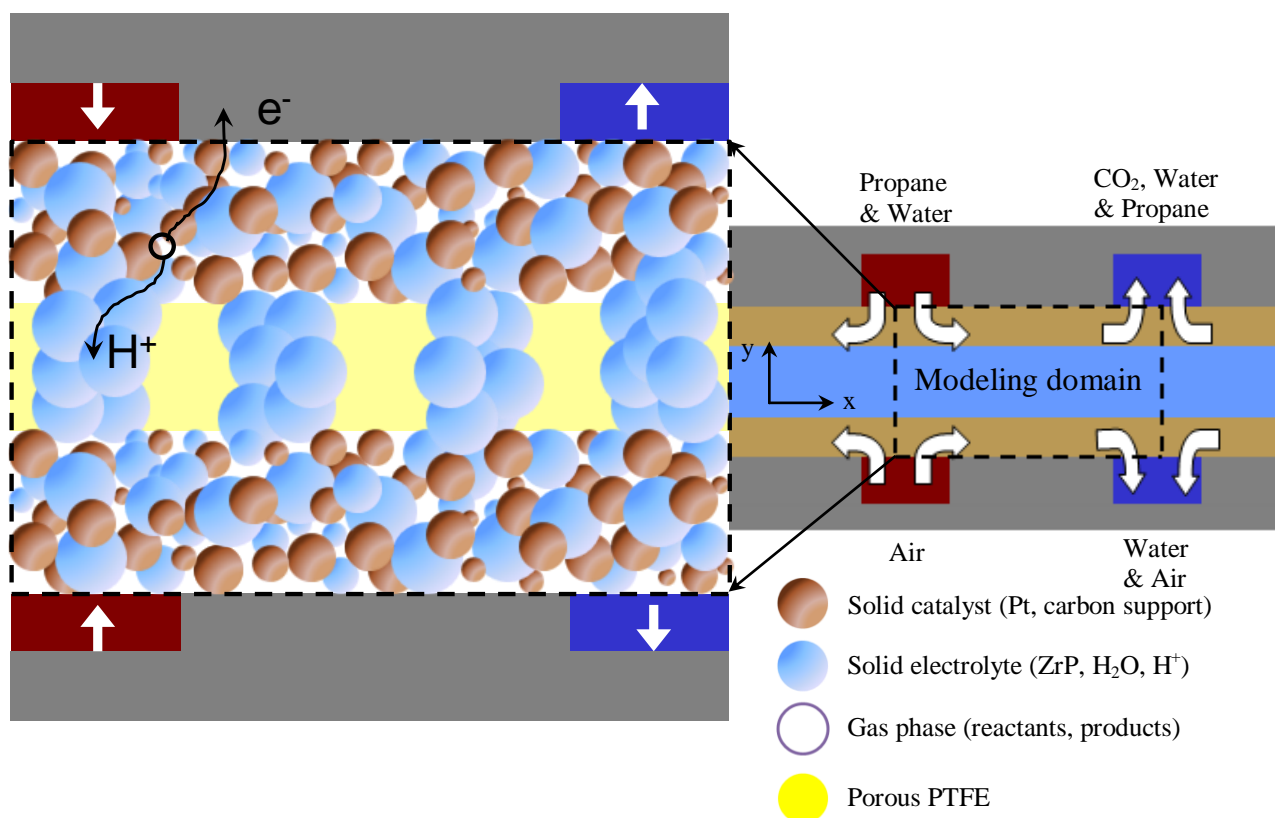


**Figure 2.7. Modeling domain and existing phases at the anode, cathode and membrane layers of a DPFC**

Figure 2.8 shows the local variables that are represented in a mathematical model of a DPFC. Four types of conservation equations are used to calculate these variables: conservation of mass, momentum, non-charged species, and charged species. There are also some parameters in the conservation equations that have to be calculated using constitutive equations and the equations of state. Table 2.1 lists the most common constitutive equations and the equations of state for different layers.

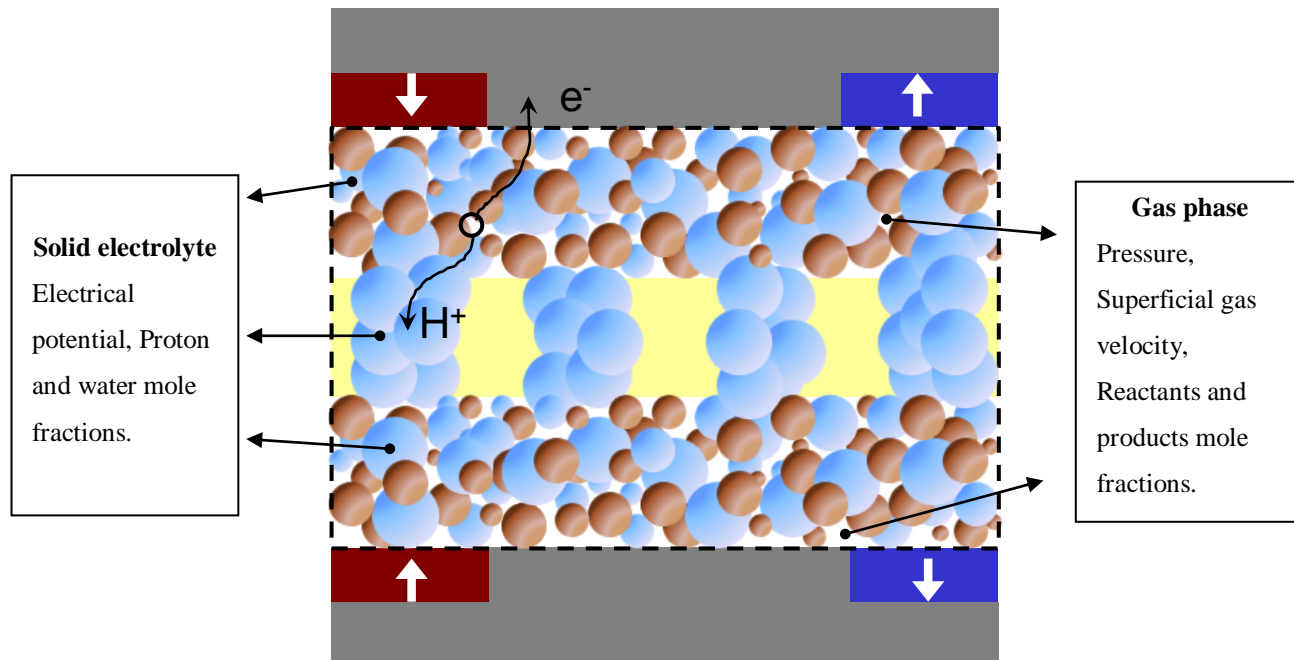


Figure 2.8. Parameters that must be solved for in a mathematical model

Table 2.1. Constitutive equations and the equations of state required in different layers of a PEM fuel cell

Layer	Equations	Example
<b>Anode and cathode catalyst layers</b>	Reaction	Butler-Volmer equation, or complex kinetics expressions
	Mass transport	Fick's law, or Maxwell-Stefan equations
	PVT relation	Ideal gas law, or equation of state
<b>Electrolyte Layer</b>	Mass transport	Nernst-Planck, or Maxwell-Stefan equation
	Membrane swelling	Empirical or thermodynamic models
	PVT relation	Ideal gas law, or equation of state
<b>Anode and cathode diffusion layers</b>	Mass transport	Fick's law, or Maxwell-Stefan equations
	PVT relation	Ideal gas law, or equation of state
<b>Anode and cathode gas channels</b>	Mass transport	Fick's law, or Maxwell-Stefan equations
	PVT relation	Ideal gas law, or equation of state

The remainder of Section 2.5 describes the modeling studies for individual cell components.

### 2.5.1. Electrolyte Modeling

The majority of PEM fuel cell models represent Nafion electrolyte membranes although many other types of membranes have been investigated experimentally. A model developed for the Nafion membrane can sometimes be used for other types of membranes by altering the physical and transport properties. The governing equations remain unchanged.

The electrolyte membrane in the PEM fuel cells have been modeled within two extremes, namely macroscopic and microscopic approaches. Microscopic models are based on *ab initio* quantum chemistry and molecular dynamics. These models provide a fundamental understanding of processes like diffusion in the membrane on a microscopic scale. This subject is beyond the scope of this dissertation, and the readers are referred to a review paper written by Kreuer et al. [17]. Although these models provide valuable information about the single ions and pore-level effects, they are usually too complex and computationally demanding to use in a whole fuel cell model.

The macroscopic mechanistic models are often more practical and focus on predicting water flux and electrical potential drop within the electrolyte phase. Estimating the water flux is essential for the water management in the fuel cell. The calculation of the electrical potential drop is required to predict the polarization curve of the fuel cell. As the macroscopic approach was selected in this research, the following survey focuses on the relevant studies.

Water is produced in the cathode side of a fuel cell. It is also dragged by protons moving from the anode side to the cathode side of the fuel cell. Hence, more water is present on the cathode side of the membrane than on the anode side. Although PEM fuel cells are fed with humidified gases at the anode and cathode, there is usually water vapour on the anode side and liquid water on the cathode side of the membrane. As mentioned before, the water content of a Nafion membrane affects its proton conductivity. On the other hand, membranes exhibit a difference in water content (and therefore other properties). Both vapour and liquid phases of water can be in contact with the membrane [18]. Therefore, the phase of the water plays an important role in the membrane modeling. It also determines the complexity of the model. The macroscopic models for membranes are usually divided into two main categories: those that assume the membrane

exists as a single phase, and those that assume it contains two phases. There is a third category which is the combination of single phase and two phases models [19].

Single phase models treat the electrolyte membrane (composed of a polymer matrix and moving species) as a single homogeneous phase with no real pores. The polymer matrix is stationary while water and protons are dissolved in the polymer matrix and move by diffusion. One approach to express the movement of charged species is using dilute solution theory in which only the interaction between each moving species and the polymer matrix is considered [20]. The Nernst-Planck equation, Eq. (2-5), expresses the movement of the charged species  $i$  within the polymer matrix.

$$\mathbf{N}_{i,ELY} = -z_i u_i F c_{i,ELY} \nabla \Phi_{ELY} - D_i \nabla c_{i,ELY} + c_{i,ELY} \mathbf{u}_{ELY} \quad (2-5)$$

The first term in the expression is a migration term representing the motion of charged species that results from a potential gradient. The second term relates the diffusive flux of the charged species to their concentration gradient. The final term is a convective term and represents the movement of species due to the bulk motion of the solvent. In one-phase systems, the solvent is the stationary polymer matrix, and thus,  $\mathbf{u}_{ELY} = 0$ .

In Eq. (2-5), mobility  $u_i$  and diffusion coefficient  $D_i$  are transport properties and can be related to each other at infinite dilution via the Nernst-Einstein equation, Eq. (2-6):

$$D_i = RTu_i \quad (2-6)$$

Eq. (2-5) reduces to Fick's law for water movement in the membrane because it is a neutral species and  $z_w = 0$ . However, another transport mechanism for water movement in the polymer matrix can be considered in Eq. (2-5). It is called electro-osmotic drag. As protons move across the membrane, they drag water molecules in the same direction causing an electro-osmotic flux. Electro-osmotic flux is proportional to the current density and can be added to the diffusive flux to calculate the overall flux of water which gives Eq. (2-7).

$$N_{w,ELY} = \xi \frac{j}{F} - D_w \nabla c_{w,ELY} \quad (2-7)$$

Kulikovsky [21] developed a model of water transport in a membrane electrode assembly of a polymer electrolyte fuel cell where a macroscopic single phase approach was chosen to model the membrane. Nguyen and White [22] also developed a model for water and heat management in a PEMFC using the single phase approach. Their model can calculate the required humidification to maintain high proton conductivity in the membrane, and the amount of heat that has to be removed from a PEM fuel cell. It is also able to predict the effects of various design and operating parameters on the performance of a PEM fuel cell. The same approach has been applied by Cheddie and Munroe [23] to model higher temperature membranes, such as polybenzimidazole (PBI). They reported a one dimensional mathematical model that predicted the polarization performance of a PEMFC having a PBI membrane.

In two-phase models, the membrane is assumed to have pores that are filled with liquid water. Thus, the two phases are liquid water and membrane material. As the operating temperature for the membrane in this research is above the boiling temperature of the water, the membrane contains one phase only.

### 2.5.2. Gas Diffusion Layer Modeling

Gas diffusion layers allow a more uniform distribution of fuel and oxidant to the catalyst layers, but they cause a resistance for the transport of species. Therefore, the focus of mathematical modeling is to calculate the species concentration distribution. Fick's law of diffusion is applied for fuel cells with two components in their anode and cathode. The Stefan-Maxwell equations, Eq. (2-8) are used for more than two components in the anode and cathode [24]:

$$\nabla y_i = \sum_{\substack{j=1 \\ j \neq i}}^n \frac{y_i N_j - y_j N_i}{c_T D_{ij}} \quad i = 1, 2, \dots, n - 1 \quad (2-8)$$

### 2.5.3. Catalyst Layer Modeling

Electrochemical reactions take place at the catalyst layers of the fuel cell. Catalyst layers are porous media composed of a gas phase, an electrolyte phase and a solid catalyst phase (i.e. platinum on carbon support). Fuel, oxidant and reaction products flow through the pores of the catalyst layers. Therefore, momentum transport (material flow through the porous media), mass transport (concentration distribution of non-charged species within the porous media, and that of charged species within the electrolyte phase), and electrochemical reactions at the interface of three phases (gas, catalyst, and electrolyte) are the main phenomena that have to be considered. In other words, the electrolyte and diffusion layer models (Sections 2.5.1 and 2.5.2) can be used in the catalyst layer along with additional kinetics expressions for the electrochemical reactions at the catalyst layer.

Microscopic and macroscopic catalyst models of PEM fuel cells have been developed, similar to the electrolyte models. In the microscopic approach, quantum mechanical methods are employed. Using these methods, the electrochemical reaction mechanisms can be predicted, the rate constant and the activation energy of the rate limiting step can be determined, and a proper catalyst for a specific reaction can be identified. This subject is beyond the scope of this dissertation, and the readers are referred to [25].

Based on the length scale of the model, the macroscopic models for fuel cell catalyst can be categorized into the following four types: (a) interface models, (b) macro-homogeneous models, (c) thin film models, and (d) agglomerate models. Each category is suitable for specific applications and dictates the amount of complexity.

The interface models treat the catalyst layer as an infinitely thin interface between the gas diffusion medium and the membrane layer. These models are used when the catalyst structure can be ignored, and the emphasis is on the membrane performance or on the water balance. In this approach, Faraday's law is used as a generation/consumption term in the boundary condition for the conservation of mass at the interface of the gas diffusion layer and the membrane interface. This approach cannot be applied to study the structural parameters of the catalyst layer such as the catalyst loading.

The macro-homogeneous models assume that the catalyst layer is a homogeneous solid structure composed of metal catalyst, carbon support, and the electrolyte phase without gas pores. The gas species dissolve and diffuse within the electrolyte phase, and as a result, the diffusion rate is low. These models account for variations across the catalyst layer but ignore micro-structural details. For example, variation of current density within the catalyst layer can be investigated, but this variation at the agglomerate scale is neglected.

Thin film models are similar to the macro-homogeneous models except that the gas pores are assumed to exist and that the catalyst particles (metal catalyst and carbon support) are covered by a thin film of electrolyte phase. All phases exist in all volume elements. Like the macro-homogeneous models, the thin film models describe the transport phenomena within the catalyst layer. The major difference between the macro-homogeneous models and the thin film models is the value of the diffusion coefficients because the species diffuse in the gas phase for the thin film models and in the electrolyte phase for the macro-homogeneous models. There were two groups that were the pioneers in such mechanistic modeling of PEM fuel cells [12,13]. They and other researchers who follow their approach use the film model for catalyst modeling.

In the agglomerate models, the variation of the physical variables in the agglomerate scale is not ignored, and the characteristic length is the radius of the agglomerate. The reactants diffuse through the electrolyte phase surrounding the agglomerate to reach the catalyst active sites where reactions occur, and product diffuses back through the electrolyte phase to the gas phase. Therefore, there is a concentration and potential distribution inside the agglomerate [14].

As the film model does not include pore scale modeling, it cannot describe the flow of immiscible fluids in pores [26]. In other words, it assumes that gas and liquid flow through two types of pores. This distinction is acceptable at low current densities that produce a small amount of water. However, at high current densities that produce a significant amount of water, gas and liquid will flow together in a pore. Therefore, the agglomerate model should be used to predict phenomena related to flooding. It is worth mentioning that film models fail to predict concentration polarization in a polarization curve, because they cannot take water flooding into account [26].

For the high temperature DPFCs there is only gas phase flowing through the pores. Therefore, there is no need to apply the agglomerate model to predict the water flooding.

#### 2.5.4. Gas Channel Modeling

Since gas channels were not modeled in this work, the comment on gas channels will be general in nature.

Two common approaches in gas channel modeling are homogeneous concentration and plug flow [27]. In the homogeneous concentration approach, the species composition along the gas channel is assumed to be uniform and equal to the value at the outlet of the channel. This assumption is applicable in 1-D and 2-D models that are not "along-the-gas channel" (z-direction in Figure 2.5). However, to predict the variations along the gas channel it is necessary to use a plug flow approach in which molar flux of species is a function of the z-direction.

## 2.6. Nomenclature

$c_T$ : total concentration of the gas mixture [gmole/m<sup>3</sup>]

$c_{i, ELY}$ : concentration of charged species  $i$  in the electrolyte phase [gmole/m<sup>3</sup>]

$D_i$ : diffusion coefficient of species  $i$  [m<sup>2</sup>/s]

$D_{ij}$ : diffusion coefficient of species  $i$  in species  $j$  [m<sup>2</sup>/s]

$F$ : Faraday's constant, 96485 [Coulombs/mol charge]

$i$ : current [A]

$\mathbf{j}$ : current density [mA cm<sup>-2</sup>]

$N_{i, ELY}$ : flux of species  $i$  in the electrolyte phase [gmol/m<sup>2</sup>s]

$N_i$ : flux of species  $i$  in the gas phase [gmol/m<sup>2</sup>s]

$N_j$ : flux of species  $j$  in the gas phase [gmol/m<sup>2</sup>s]

$P$ : total pressure [Pa]

$R$ : universal gas constant [ J/(mol K) ]

$T$ : temperature [K]

$u_i$ : mobility of species  $i$  [m<sup>2</sup>.mol/J.s]

$\mathbf{u}_{ELY}$ : velocity of the electrolyte phase [m/s]

$y_i$ : mole fraction of species  $i$  in the gas phase [-]

$z_i$ : charge number of species  $i$

**Greek letters:**

$\xi$ : electro-osmotic coefficient [-]

$\Phi$ : electrical potential [V]

$\Phi_{\text{ELY}}$ : electrical potential in the electrolyte phase [V]

$\Phi_{\text{Cell}}$ : cell potential [V]

$\Phi_{\text{OCV}}$ : open circuit potential [V]

$\Delta\Phi$ : electrical potential difference [V]

$\Delta\Phi_{\text{Act}}$ : activation polarization [V]

$\Delta\Phi_{\text{Conc}}$ : concentration polarization [V]

$\Delta\Phi_{\text{Ohm}}$ : ohmic polarization [V]

**Subscripts and Superscripts:**

AN: anode

CA: cathode

CO<sub>2</sub>: carbon dioxide

ELY: electrolyte layer

$i$ : species; propane, water, CO<sub>2</sub>, and H<sup>+</sup>

P: propane

W: water

**Abbreviations:**

DPFC: direct propane fuel cell

MEA: membrane electrode assembly

OCV: open circuit voltage

PEM: polymer electrolyte membrane or proton exchange membrane

PEMFC: polymer electrolyte membrane or proton exchange membrane fuel cell

PTFE: polytetrafluoroethylene

PVT: pressure-volume-temperature

ZrP: zirconium phosphate

## 2.7. References

- [1] F. Barbir, PEM fuel cells : theory and practice, Elsevier Academic Press, Burlington, MA; 2005, pp. 433.
- [2] P. Zapata, P. Basak, J. Carson Meredith, High-throughput screening of ionic conductivity in polymer membranes, *Electrochim.Acta*, 54 (2009) 3899-3909.
- [3] T.V. Nguyen, A gas distributor design for proton-exchange-membrane fuel cells, *J.Electrochem.Soc.*, 143 (1996).
- [4] W. Yan, S. Mei, C. Soong, Z. Liu, D. Song, Experimental study on the performance of PEM fuel cells with interdigitated flow channels, *J.Power Sources*, 160 (2006) 116-122.
- [5] W. Yan, C. Yang, C. Soong, F. Chen, S. Mei, Experimental studies on optimal operating conditions for different flow field designs of PEM fuel cells, *J.Power Sources*, 160 (2006) 284-292.
- [6] H.A. Liebhafsky, E.J. Cairns, The direct hydrocarbon fuel cell with aqueous electrolytes, In: *Fuel Cells and Fuel Batteries*, Wiley, New York, 1968, pp. 458-523.
- [7] J.O. Bockris, S. Srinivasan, Fuel cells: their electrochemistry, In: *Electrochemical Combustion of Organic Substances*, McGraw-Hill, New York, 1969, pp. 357-411.
- [8] E.J. Cairns, The anodic oxidation of hydrocarbons and the hydrocarbon fuel cell, *Adv Electrochem and Electrochem Eng*, 8 (1971) 337-391.
- [9] Y. Si, R. Jiang, J. Lin, H.R. Kunz, J.M. Fenton, CO tolerance of carbon-supported platinum-ruthenium catalyst at elevated temperature and atmospheric pressure in a PEM fuel cell, *J.Electrochem.Soc.*, 151 (2004) A1820-A1824.
- [10] J. Kim, S. Lee, S. Srinivasan, C.E. Chamberlin, Modeling of proton exchange membrane fuel cell performance with an empirical equation, *J.Electrochem.Soc.*, 142 (1995) 2670-2674.
- [11] D.M. Bernardi, M.W. Verbrugge, Mathematical model of a gas diffusion electrode bonded to a polymer electrolyte, *AIChE J.*, 37 (1991) 1151-1163.
- [12] T.E. Springer, T.A. Zawodzinski, S. Gottesfeld, Polymer electrolyte fuel cell model, *J.Electrochem.Soc.*, 138 (1991) 2334-2342.

- [13] P. Hu, L. Peng, W. Zhang, X. Lai, Optimization design of slotted-interdigitated channel for stamped thin metal bipolar plate in proton exchange membrane fuel cell, *J.Power Sources*, 187 (2009) 407-414.
- [14] N.P. Siegel, M.W. Ellis, D.J. Nelson, M.R. von Spakovsky, Single domain PEMFC model based on agglomerate catalyst geometry, *J.Power Sources*, 115 (2003) 81-89.
- [15] D.F. Cheddie, N.D.H. Munroe, A two-phase model of an intermediate temperature PEM fuel cell, *International Journal of Hydrogen Energy*, 32 (2007) 832-841.
- [16] J.J. Baschuk, X. Li, A comprehensive, consistent and systematic mathematical model of PEM fuel cells, *Appl.Energy*, 86 (2009) 181-193.
- [17] K. Kreuer, S.J. Paddison, E. Spohr, M. Schuster, Transport in proton conductors for fuel-cell applications: Simulations, elementary reactions, and phenomenology, *Chem.Rev.*, 104 (2004) 4637-4678.
- [18] A.Z. Weber, J. Newman, Transport in polymer-electrolyte membranes. I. Physical model, *J.Electrochem.Soc.*, 150 (2003).
- [19] A.Z. Weber, J. Newman, Modeling transport in polymer-electrolyte fuel cells, *Chem.Rev.*, 104 (2004) 4679-4726.
- [20] J. Newman, K.E. Thomas-Alyea, *Electrochemical Systems*, 3rd ed., Wiley-Interscience, New Jersey, USA; 2004, pp. 672.
- [21] A.A. Kulikovskiy, Quasi-3D modeling of water transport in polymer electrolyte fuel cells, *J.Electrochem.Soc.*, 150 (2003).
- [22] T.V. Nguyen, R.E. White, Water and heat management model for proton-exchange-membrane fuel cells, *J.Electrochem.Soc.*, 140 (1993) 2178-2186.
- [23] D. Cheddie, N. Munroe, Mathematical model of a PEMFC using a PBI membrane, *Energy Convers.Manage.*, 47 (2006) 1490-1504.
- [24] R.B. Bird, W.E. Stewart, E.N. Lightfoot, *Transport phenomena*, 2nd ed., J. Wiley, New York; 2002, pp. 895.
- [25] W. Vielstich, A. Lamm, H.A. Gasteiger (Eds.), *Handbook of Fuel Cells: Fundamentals, Technology, and Applications Vol. 2: Electrocatalysis*, In: , John Wiley & Sons, New York, 2003.
- [26] L. Pisani, G. Murgia, M. Valentini, B. D'Aguzzo, A working model of polymer electrolyte fuel cells comparisons between theory and experiments, *J.Electrochem.Soc.*, 149 (2002).

[27] K.Z. Yao, K. Koran, K.B. McAuley, P. Oosthuizen, B. Peppley, T. Xie, A review of mathematical models for hydrogen and direct methanol polymer electrolyte membrane fuel cells, *Fuel Cells*, 4 (2004) 3-29.

## CHAPTER 3

---

# DIRECT PROPANE FUEL CELL ANODE WITH INTERDIGITATED FLOW FIELDS: TWO-DIMENSIONAL MODEL<sup>1</sup>

H. Khakdaman, Y. Bourgault, M. Ternan

### ABSTRACT

The first two-dimensional model of a direct propane fuel cell (DPFC) anode was developed and used to investigate materials and operating conditions that resulted in improved DPFC anode performance. The software used, FreeFEM<sup>++</sup>, is open source and is based on the finite element method. The anode catalyst layer (ACL) was composed of three phases. One solid phase was the platinum catalyst supported on porous carbon (an electron conductor). The second solid phase consisted of solid zirconium phosphate (a proton conductor at 150°C). The gas phase was located within the pores of the carbon and between the solid particles. Operation at 150°C allowed the propane gas phase concentration to be in direct contact with the catalyst at the entrance to the ACL. This was an important advantage compared to previous DPFC operations at conditions where aqueous liquids are present (PEMFC at temperatures less than 100°C and direct propane PAFC). When aqueous liquids surround the catalyst, the propane concentration in contact with the catalyst at the ACL entrance is much smaller because the solubility of propane in aqueous liquids is small. The one-third improvement in the anode overpotential was attributed to this difference. By using interdigitated flow fields with the propane feed in one set of channels and the carbon dioxide product in another set of channels, there was no mixing of the two so that the maximum propane concentration was always present at the entrance to the ACL. The residence time could be chosen, by adjusting the distance between the feed and the product channels (width

---

<sup>1</sup> This paper was published in *Ind. Eng. Chem. Res.* 49, 2010, 1079–1085

of land plus channel), to obtain large values of conversion and large values of fuel utilization. It was shown that the larger pressure drops often associated with interdigitated flow fields compared to conventional serpentine flow fields were diminished by increasing the thickness of the catalyst layer. In addition, the thicker catalyst layer permitted the Pt catalyst to be spread over a greater thickness of carbon catalyst support, thereby ensuring better catalyst dispersion and improved catalyst performance.

### **3.1. Introduction**

Although the concept of a fuel cell for the conversion of the chemical energy in a fuel into electrical energy has been known for more than 150 years, it is only recently that commercial fuel cell products have become available. Our focus is on the application of fuel cells for the production of electrical energy in rural areas. Work in our laboratory is directed toward the development of commercial fuel cells in which a hydrocarbon such as propane is the fuel that reacts directly on the anode of the fuel cell. Propane was chosen as the particular hydrocarbon fuel for several reasons. (1) Existing infrastructure: Liquefied petroleum gas, LPG, whose principal component is propane, is currently used as a fuel for heating purposes in many rural areas. In principle, trucks can deliver LPG to any location that is accessible by road. (2) Capital cost: Utility companies incur much greater costs when supplying electrical power to rural clients than to urban clients. Therefore the acceptable purchase cost for fuel cells will be greater for rural markets than for urban markets. (3) Fuel cell performance: Although hydrogen and methanol fuels are much more reactive (have greater current densities) in fuel cells than any of the hydrocarbon fuels, among the hydrocarbons the performance of propane has been found to be slightly superior to other low molecular weight alkanes.

The electrochemical reaction of hydrocarbon fuels directly at the anode of a fuel cell has several advantages compared to hydrogen or methanol as the fuel. Hydrocarbons, specifically methane in natural gas, must be converted to form hydrogen and methanol. (1) By using the hydrocarbons directly in fuel cells, the capital cost for processing equipment needed to produce hydrogen or methanol can be eliminated. (2) Furthermore the conversion energy inefficiencies (e.g. endothermic heat required for steam reforming) are also eliminated. (3) The infrastructure to deliver hydrocarbons is already in place (natural gas pipelines in urban areas and commercial

trucking systems for delivery of LPG and diesel fuel in rural areas). A substantial additional capital cost for delivery systems would be required if hydrogen and/or methanol were to become equally accessible. (4) There is a greater energy loss, caused by the reversible entropy change, when hydrogen is the fuel than when the fuel is a hydrocarbon. (5) Hydrogen has a smaller energy density than hydrocarbons, as can be seen in Table 3.1 where lower heating values are compared. Note that LPG (propane) is stored as a liquid (typically less than 10 atmospheres at ambient temperature). For transportation applications the energy density determines the amount of energy that can be stored in a fuel tank of a particular size. (6) There are energy losses associated with hydrogen storage that do not occur during the storage of most liquid hydrocarbons (energy to compress gaseous hydrogen to 200 – 700 atm [1], or the boil-off of liquid hydrogen stored at  $-253^{\circ}\text{C}$ ). (7) Although there are safety issues with hydrocarbons, safety is often a greater concern with hydrogen. For example, hydrogen has a much larger range of Explosive/Flammable Limits (4 – 75%) than hydrocarbons (e.g. propane 2.1 – 10.1%). There are also safety concerns with methanol. For example, methanol has a toxic effect on the nervous system, particularly the optic nerve [2].

**Table 3.1. LHV energy densities of fuels [3]**

<b>Fuel</b>	<b>energy density (MJ/m<sup>3</sup> at 200 atm., 15°C) gas</b>	<b>energy density (MJ/m<sup>3</sup> at 690 atm., 15°C) gas</b>	<b>energy density (MJ/m<sup>3</sup> of Liquid)</b>
Hydrogen	1,825	4,500	8,491
Methanol			15,800
Propane			23,488
Gasoline			31,150

Although hydrocarbons have many advantages they also have one major disadvantage compared to hydrogen or methanol. In fuel cells, hydrocarbon reaction rates (current densities) are more than one order of magnitude slower than those of hydrogen or methanol. Work in our laboratory is directed toward both the identification of the phenomena that influence fuel cell current densities and the suggestion of alternative materials / operating conditions. If the current density

limitation could be improved sufficiently, then direct hydrocarbon fuel cells might become competitive with hydrogen and with methanol fuel cells.

Propane fuel cells emit carbon dioxide at the fuel cell location. Both the hydrogen and the methanol used in fuel cells are produced from natural gas. Therefore both hydrogen fuel cells and methanol fuel cells are responsible for carbon dioxide emissions at the locations where natural gas is used to produce the hydrogen or methanol. The type of fuel cell with the greatest energy efficiency will emit the smallest quantity of carbon dioxide per Watt of electrical power produced. At the current state of development, both hydrogen and methanol fuel cells have greater energy efficiencies than hydrocarbon fuel cells. In contrast the maximum theoretical energy efficiencies for hydrocarbon fuel cells are almost 30% greater than those for hydrogen and methanol fuel cells. If hydrocarbon fuel cells could be improved sufficiently, it is possible that they could become more energy efficient than either hydrogen or methanol fuel cells, and therefore have smaller carbon dioxide emissions.

The vast majority of fuel cell research with hydrocarbons as the fuel was performed in the 1959 – 1968 period. That work has been summarized in three reviews, Liebhafsky and Cairns [4], Bockris and Srinivasan [5], and Cairns [6]. A few of the studies that have been performed since that time include the following: A reaction network for methane electrochemical oxidation has been proposed by Bagotzky et al. [7]. Experiments measuring the species adsorbed on a platinum anode during methane electrochemical oxidation have been reported by Hahn and Melendres [8]. The use of propane in a Nafion polymer electrolyte membrane (PEM) fuel cell was reported by Savadogo and Varela [9]. Modeling work in our laboratory has been focused both on the fuel cell as a reactor, Psoginakis et al. [10] and on the fuel cell catalyst Psoginakis et al. [11].

The polarization curves in Figure 3.1 are typical of the best performance that has been obtained using direct propane fuel cells. Aqueous phosphoric acid fuel cells (PAFC) are probably typical of other types of direct propane fuel cells having conventional electrolytes. Two types of polymer electrolyte membrane fuel cells (PEMFC) are also shown. One is a Nafion membrane that is commonly used in hydrogen fuel cells. The other is polybenzimidazole (PBI) impregnated with sulphuric acid. The PAFC results [12] at 150°C are comparable to the Nafion membrane

results [9] at 95°C at low current densities. Fuel cells having Nafion or sulphuric acid electrolytes are normally operated at temperatures less than 100°C, while PAFC are normally operated above 100°C. In this work, fuel cell materials (platinum anode catalyst and zirconium phosphate electrolyte) and operating conditions (150°C) were chosen in an attempt to obtain fuel cell performance that exceeds the typical state-of-the-art values shown in Figure 3.1.

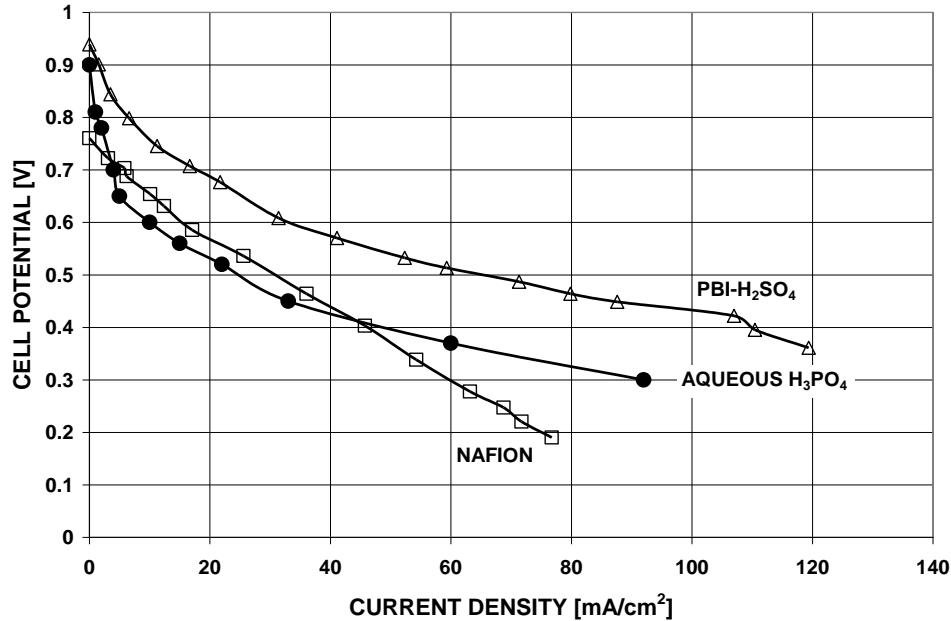


Figure 3.1. Polarization curves for direct propane fuel cells. The open squares (Nafion electrolyte) and open triangles (polybenzimidazole-H<sub>2</sub>SO<sub>4</sub> electrolyte) data were measured at 95°C [9]. The solid circles (aqueous H<sub>3</sub>PO<sub>4</sub> electrolyte) data were measured at 150°C [12].

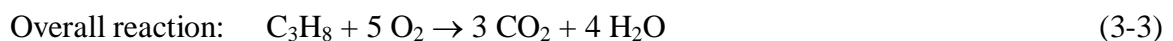
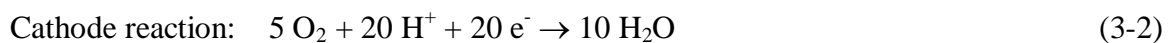
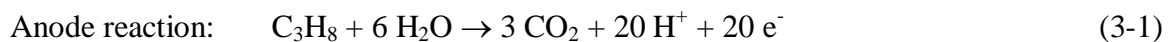
Zirconium phosphate (ZrP) was chosen to be the electrolyte material because it is capable of operation at greater temperatures than Nafion, the electrolyte most commonly used in PEM (polymer electrolyte membrane) fuel cells. Since the performance of propane fuel cells is limited by the anode electro-catalyst, increasing the temperature is one method of increasing the anode kinetics. The characteristics of PEM fuel cell components when operating at higher temperatures have been reviewed recently [13]. As the temperature is increased towards the boiling point of water, the performance of Nafion membranes declines substantially. Furthermore the glass transition temperature, which affects the morphology of a solid, is less than 160°C for Nafion. Zirconium phosphate was deemed to be a promising electrolyte for at least two reasons. First,

although the proton conductivity is small ( $10^{-6}$  S/cm) for the pure material [14], when ZrP is combined with PTFE (polytetrafluoroethylene) its conductivity has been reported to exceed  $10^{-3}$  S/cm [15]. The reason suggested for the improvement in proton conductivity was surface conductivity. Second, fuel cells having ZrP-PTFE composite membranes have demonstrated reasonable performance when operated at a  $120^{\circ}\text{C}$  when hydrogen was the fuel [16].

Our model of the anode was based on the properties of Vulcan XC72 as the carbon black support for the platinum catalysts. In practice the rate of carbon black corrosion at  $150^{\circ}\text{C}$  for the cathode may be excessive. Hence it may be necessary to replace the carbon black with a more corrosion resistant graphitized carbon support, as has been reported for phosphoric acid fuel cells [17] that operate at  $200^{\circ}\text{C}$ .

Although conventional serpentine flow fields are suitable for hydrogen fuel cells, they have at least one disadvantage for hydrocarbon fuel cells. With serpentine flow fields, the  $\text{CO}_2$  formed in the catalyst layer must exit the fuel cell through the same channel that carries the inlet hydrocarbon feed. As a result the concentration of the hydrocarbon feedstock decreases progressively along the length of the channel, as it becomes mixed with progressively more and more  $\text{CO}_2$  product. In contrast with interdigitated fuel cells, the feedstock enters through one channel, flows through the catalyst layer (parallel to the electrolyte membrane) where it reacts, and the  $\text{CO}_2$  product leaves through a different channel. Thus with interdigitated flow fields the concentration driving force that causes the reactant hydrocarbon to enter the anode catalyst layer can remain large along the entire length of the channel. Studies of the characteristics of interdigitated flow fields have been reported by Wood et al. [18] and Yan et al. [19].

This work describes the first two-dimensional model of a direct propane fuel cell having an interdigitated flow field. A schematic diagram is shown in Figure 3.2. The reactions in the fuel cell are shown below:



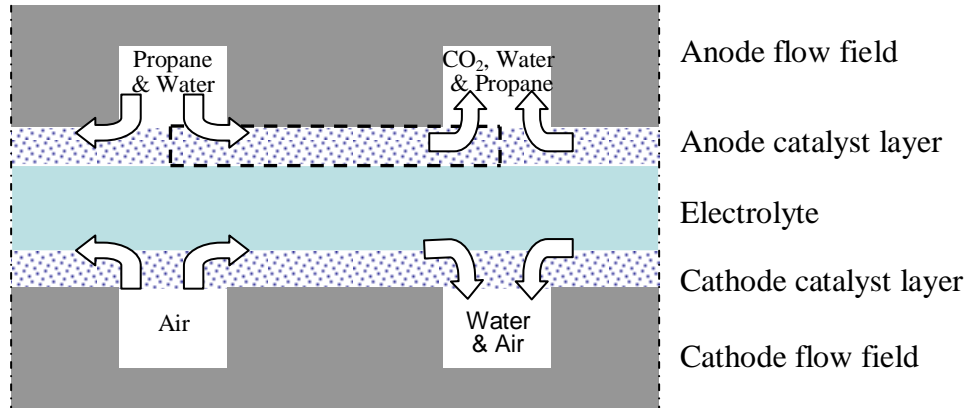


**Figure 3.2. Schematic of a direct propane fuel cell with interdigitated flow field: cross-sectional view showing the modeling domain with the dashed line**

### 3.2. Mathematical Model

The equations used to represent the anode of the propane fuel cell were solved for an operating temperature of 150°C. The anode catalyst layer described in this work was composed of porous carbon black (surface area 255 m<sup>2</sup>/g), platinum catalyst, and zirconium phosphate. The volumetric fractions of the gas phase and the two solid phases were:  $\epsilon_{GAS} = 0.6$ ,  $\epsilon_{ZrP} = 0.2$ , and  $\epsilon_{Pt/C} = 0.2$ .

The anode catalyst layer contained a solid proton conductor, zirconium phosphate. There are two possible phases of zirconium phosphate. The  $\alpha$ -phase contains a single water of hydration molecule, Troup and Clearfield [20]. The  $\gamma$ -phase contains two hydrated water molecules, Poojary et al. [21]. Park et al. [22] have reported on their conductivity in composites of zirconium phosphate and polytetrafluoroethylene. The proton conductivity of the zirconium phosphate was obtained from the work of Silva et al. [23]. The proton diffusivity in zirconium phosphate was obtained from the work of Sang and Huang [24]. The anode catalyst layer was adjacent to an electrolyte composed of a porous polytetrafluoroethylene (PTFE) membrane, whose pores were filled with zirconium phosphate. Unlike the membrane electrolytes shown in Figure 3.1, the ZrP-PTFE membrane is capable of operating above 100°C. This has two advantages. First, rates of reaction improve as the temperature increases. A second advantage is being above the boiling point of water to ensure that no liquid phase water is present around the platinum

catalyst particles. When there is a film of liquid water around catalyst reaction sites, the propane must first dissolve in the liquid phase water and then diffuse from the liquid water surface to the reaction sites on the catalyst. The solubility of propane in liquid water is small. Therefore when liquid phase water is present, the concentration driving force from the surface of the liquid water to the surface of the catalyst is very small. The earlier work by Psfogiannakis et al. [10] accounted for the liquid film of water around the catalyst particles using a modified flooded agglomerate model. That was the appropriate model for a PAFC. It would also be relevant to a direct propane PEMFC with water being fed to the anode at temperatures less than 100°C. In contrast at 150°C there will be no liquid water and no liquid film. Therefore the use of the flooded agglomerate model would be inappropriate. For our study, the entire pressure of the gas phase will be in direct contact with the reaction sites on the anode catalyst.

The mathematical equations used in the two-dimensional numerical model are shown in Table 3.2. Eq. (3-4) is a transient mass balance for Eq. (3-1). Because the ACL is essentially a packed bed, the pressure drop was described using the linear form of the Ergun equation, Eq. (3-5). Mass balances for each of the individual gas phase species, propane (P), water (W), and carbon dioxide (CO<sub>2</sub>) accounted for convection, diffusion (Fick's Law), and reaction, as shown in Eq. (3-6a) to Eq. (3-6c). The mass balance for protons that occurred in the electrolyte phase within the ACL accounted for diffusion, migration, and reaction as shown in Eq. (3-6d). The protons formed in the ACL are a charge carrier and they respond to Ohm's law as is also shown in Eq. (3-7).

The electrochemical reaction was described using the Butler-Volmer equation, Eq. (3-8). The rate of production of protons per unit volume,  $(r_{\text{Prot}})_{\text{AN}}$ , in Eq. (3-8) was multiplied by the volume of the ACL to obtain the total reaction rate. When the thickness of the catalyst layer changed, the volume of the ACL also changed. Therefore the number of catalyst sites changed as the ACL volume changed and as the catalyst layer thickness changed. The reaction mechanism for the electrochemical conversion of propane contains many steps. As an example, the Bagotsky mechanism [7] used to describe the electrochemical conversion of methane, a simpler molecule, has at least 14 steps. More steps occur in propane conversion. For the methane conversion reaction, quantum mechanical computations by Psfogiannakis et al. [11] have shown that the

initial reaction, the dissociative chemisorption of methane is rate limiting. All steps in a reaction mechanism will proceed at the same rate as the rate limiting step. For the anodic electrochemical

**Table 3.2. List of equations for the Anode Catalyst Layer (ACL)**

Equations	Eq. No.
<b>A) Conservation of Mass (equation of continuity)</b>	3-4
$\partial (\varepsilon \rho) / \partial t = - \nabla \cdot (\varepsilon \rho \mathbf{u}) - MW_P (r_{Prot})_{AN} / n_c F - 6 MW_W (r_{Prot})_{AN} / n_c F$ $+ 3 MW_{CO_2} (r_{Prot})_{AN} / n_c F$	
<b>B) Conservation of Momentum (Ergun equation)</b>	3-5
$- \nabla P = 150 [\mu (1 - \varepsilon)^2 / D_p^2 \varepsilon^3] \mathbf{u}$	
<b>C) Conservation of Species</b>	3-6
i) gas phase:	
$\partial (\varepsilon c y_P) / \partial t = - \nabla \cdot (\varepsilon c \mathbf{u} y_P) + \nabla \cdot (\varepsilon c D_{P-M} \nabla y_P) - (r_{Prot})_{AN} / n_c F$	(a)
$\partial (\varepsilon c y_W) / \partial t = - \nabla \cdot (\varepsilon c \mathbf{u} y_W) + \nabla \cdot (\varepsilon c D_{W-M} \nabla y_W) - 6 (r_{Prot})_{AN} / n_c F$	(b)
$\partial (\varepsilon c y_{CO_2}) / \partial t = - \nabla \cdot (\varepsilon c \mathbf{u} y_{CO_2}) + \nabla \cdot (\varepsilon c D_{CO_2-M} \nabla y_{CO_2}) + 3 (r_{Prot})_{AN} / n_c F$	(c)
The conservation equation for CO <sub>2</sub> does not need to be solved as CO <sub>2</sub> concentration can be calculated from the following equation:	
$y_{CO_2} = 1 - y_P - y_W$	
<b>D) Conservation of Charge</b>	3-7
For ionic current:	$\nabla \cdot (\sigma_{ZrP}^{EFF} \nabla \Phi_{ZrP}) = - (r_{Prot})_{AN}$
<b>E) Butler-Volmer equation</b>	3-8
$(r_{Prot})_{AN} = A_{av} j_0 [\exp(\alpha_A F \eta / RT) - \exp(\alpha_C F \eta / RT)]$	

Note:  $r_{Prot}$  in Chapter 3 is shown by  $j$  in Chapters 4 and 5.

conversion of propane the reaction step that is used in the Butler Volmer equation, Eq. (3-9), involves the reaction of dissociated hydrogen radicals that are adsorbed on platinum, H(Pt), and proton vacancies in the zirconium phosphate phase (ZrP) to form protons in the zirconium phosphate phase,  $H^+(ZrP)$  and electrons in the Pt/C phase,  $e^-(Pt/C)$ :



For this work the exchange current density,  $j_0$ , used in the Butler Volmer equation was  $1 \times 10^{-4} \text{ A/m}^2$ . That is the same value that was obtained by Psogiannakis et al. [10] from the data of Grubb and Michalske [12] and used in the earlier modeling of a propane PAFC [10]. Bockris et al. [25] measured almost the same value,  $9 \times 10^{-5} \text{ A/m}^2$ , specifically for the anodic oxidation of propane. The rate of reaction of gas phase propane to form adsorbed species on the platinum catalyst will be identical to every other step in the reaction mechanism including the rate limiting step and will have the same value as  $(r_{Prot})_{AN}$ , the reaction rate for proton formation in Eq. (3-9).

Figure 3.3 is a diagram showing the locations where the boundary conditions are specified. For the anode modeling being described here, the boundaries 1 to 6 around the ACL are pertinent. Boundary 1 is the interface between the feed gas phase and the ACL. Boundary 2 is a line within the ACL that defines the location at which 50% of the feed gas flows in one horizontal direction,  $z_1$ , and the other 50% flows in the opposite direction. It is a symmetry condition. Boundary 3 is the interface between the ACL and the electrolyte, ZrP-PTFE. Boundary 4 is a symmetry condition for the product gas at the exit of the ACL. Boundary 5 is the interface between the ACL and the product gas. Boundary 6 is the interface between the ACL and the land of the graphite bipolar plate. The values of the boundary conditions are shown in Table 3.3.

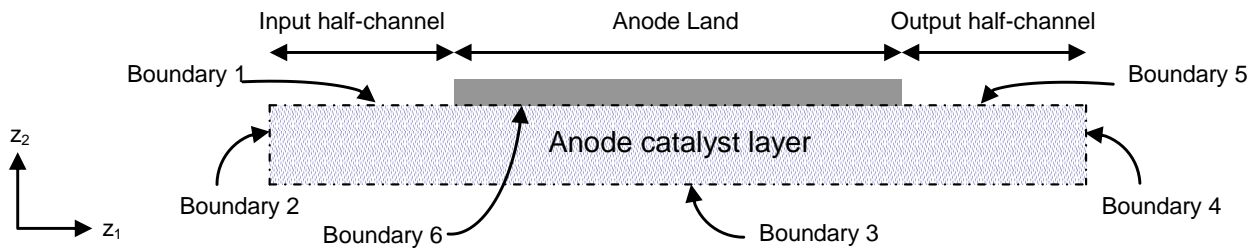


**Figure 3.3. Boundaries in the Anode Catalyst Layer of the fuel cell**

**Table 3.3. List of boundary conditions for the Anode Catalyst Layer**

Equations	Eq. No.
<p>Boundary (1) in Figure 3.3</p> $\partial\Phi_{\text{ACL}} / \partial z_2 = 0 \quad v_{z2} = 0.001 \text{ to } 0.005 \text{ m/s} \quad y_{\text{P}} = 0.07 \quad y_{\text{W}} = 0.93$ <p><math>\Phi_{\text{ACL}}</math>: electric potential in the electrolyte phase of the ACL [V]  <math>z_2</math>: distance in the <math>z_2</math> direction [m]  <math>v_{z2}</math>: velocity in the <math>z_2</math> direction [m/s]  <math>y_{\text{P}}</math>: inlet propane concentration [mol fraction]  <math>y_{\text{W}}</math>: inlet water concentration [mol fraction]</p>	3-10
<p>Boundary (2) in Figure 3.3</p> $v_{z1} = 0 \quad \partial\Phi_{\text{ACL}} / \partial z_1 = 0$ $\partial y_{\text{P}} / \partial z_1 = 0 \quad \partial y_{\text{W}} / \partial z_1 = 0$ <p><math>v_{z1}</math> : velocity in the <math>z_1</math> direction [ m/s]  <math>z_1</math> = distance in the <math>z_1</math> direction [m]</p>	3-11
<p>Boundary (3) in Figure 3.3</p> $v_{z2} = 0 \quad \Phi_{\text{ACL}} = 0.1 \text{ to } 0.5 \text{ V}$ $\partial y_{\text{P}} / \partial z_2 = 0 \quad \partial y_{\text{W}} / \partial z_2 = 0$	3-12
<p>Boundary (4) in Figure 3.3</p> $v_{z1} = 0 \quad \partial\Phi_{\text{ACL}} / \partial z_1 = 0$ $\partial y_{\text{P}} / \partial z_1 = 0 \quad \partial y_{\text{W}} / \partial z_1 = 0$	3-13
<p>Boundary (5) in Figure 3.3</p> $P = 101.3 \text{ kPa} \quad \partial\Phi_{\text{ACL}} / \partial z_2 = 0$ $\partial y_{\text{P}} / \partial z_2 = 0 \quad \partial y_{\text{W}} / \partial z_2 = 0$	3-14
<p>Boundary (6) in Figure 3.3</p> $v_{z2} = 0 \quad \Phi_{\text{ACL}} = 0.0 \text{ V}$ $\partial y_{\text{P}} / \partial z_2 = 0 \quad \partial y_{\text{W}} / \partial z_2 = 0$	3-15

### 3.3. Computational Method

The software used to solve the two-dimensional equations was FreeFEM<sup>++</sup>, developed by Hecht et al. [26]. It is open-source software that is based on the Finite Element Method (FEM). It uses arbitrary finite element (FE) spaces on unstructured bi-dimensional meshes. For their implementation in FreeFEM<sup>++</sup>, the partial differential equations, Eq. (3-4) to Eq. (3-8) and the boundary conditions Eq. (3-10) to Eq. (3-15) are rewritten into variational forms, using the Euler time-stepping scheme to discretize in time and the FEM to discretize in space. All variables are approximated by linear FE, except for the pressure which uses quadratic FE. The velocity field is calculated by differentiation of the pressure field. No numerical stabilization of any type was required to obtain nice numerical solutions on sufficiently fine meshes. Grid independence of the solution was achieved by computing solutions on successively refined meshes. The resulting nonlinear system is solved as a sequence of linear systems starting from Eqs. (3-8) and (3-7); then to the joint Eqs. (3-4) and (3-5); to finish with Eqs. (3-6). These equations were linearized in all nonlinear terms, by using dependent variables (density, concentrations, pressure, etc) at the previous time step. For instance, the overpotential  $\eta$  in the nonlinear Butler-Volmer reaction rate (Eq. (3-8)) is evaluated at the previous time step while Eq. (3-7) involving this reaction rate is solved for the potential  $\Phi_{ZrP}$  at the current time step. This strategy greatly reduced the complexity of a full nonlinear solution, such as with the Newton-Raphson method, at the expense of the several time steps required to reach a steady solution, or the smaller time steps needed to analyze transient fuel cell operation. A sufficient number of time steps must be made to reach the steady state solution of the fully coupled nonlinear system of equations. Convergence is achieved when the change in the average propane conversion from one time step to the next is five orders of magnitude less than the value of average propane conversion itself.

Because the time-stepping method is part of the numerical method, the model could be extended to simulate transient operations. The numerical values of the parameters used in the model are shown in Tables 3.4 and 3.5.

**Table 3.4. Numerical values used in computation**

<b>Parameter</b>	<b>Value</b>	<b>Unit</b>
Anode catalyst face area per unit of reactor volume, $A_{av}$	$3.302 \times 10^{-7}$	$m^{-1}$
Catalyst thickness	0.04 to 1	mm
Catalyst length	2 to 10	mm
Void fraction in the ACL, $\varepsilon$	0.6	-
Electrolyte (ZrP) fraction in the ACL, $\varepsilon_{ZrP}$	0.2	-
Metal catalyst (Pt) fraction in the ACL, $\varepsilon_{Pt}$	0.2	-
Effective particle diameter, $D_p$	$5 \times 10^{-6}$	M
Effective ionic conductivity in the electrolyte phase of the ACL [23], $\sigma_{ZrP}^{EFF}$	4.25	S/m
Diffusivity of proton in ZrP phase of ACL [24], $D_{H^+}$	$3 \times 10^{-12}$	$m^2/s$
Exchange current density [25], $j_0$	$9 \times 10^{-5}$	$A/m^2$
Anodic and cathodic charge transfer coefficients [27], $\alpha_A$ & $\alpha_C$	1.0	-
Mass density of propane (at 1 atm and 150°C), $\rho_P$	1.26	$kg/m^3$
Mass density of CO <sub>2</sub> (at 1 atm and 150°C), $\rho_{CO_2}$	1.25	$kg/m^3$
Mass density of water (at 1 atm and 150°C), $\rho_W$	0.52	$kg/m^3$

### 3.4. Results and Discussion

Molecules in the gas phase must flow through the ACL until they arrive at a reaction site. The pressure drop along the length of the ACL when using interdigitated flow fields is much greater than the pressure drop across the much smaller thickness of the ACL when using serpentine flow fields. For our study, contour lines of constant pressure are shown in Figure 3.4. One half of the entrance channel is represented by the 0.5 mm space at the top left of the Figure 3.4. One half of the exit channel is represented by the 0.5 mm space at the top right of the Figure 3.4.

The large pressure drops in interdigitated flow fields are a negative attribute and have contributed to a disinterest in their use. That perception is correct for anode catalyst layers of conventional thickness, 40  $\mu m$ , (Case 1 in Table 3.6). However by increasing the anode catalyst thickness to 400  $\mu m$ , (Case 2 in Figure 3.3), the pressure drop from the entrance channel to the exit channel was 0.129 kPa.

**Table 3.5. Correlation for binary diffusion coefficient [28]**

$$D_{ij} = 1.0 \times 10^{-9} T^{1.75} (1/MW_i + 1/MW_j)^{1/2} / P[(\Sigma v)_i^{1/3} + (\Sigma v)_j^{1/3}]^2$$

$$D_{i\text{-mixture}} = (1 - y_i) / \Sigma(y_j / D_{ij}) \text{ , summation for } j, j \neq i$$

MW <sub>P</sub>	44.1 g/gmol
MW <sub>CO2</sub>	44.01 g/gmol
MW <sub>W</sub>	18.02 g/gmol
(Σv) <sub>P</sub>	65.34 × 10 <sup>-3</sup> m <sup>3</sup> /kgatom [20]
(Σv) <sub>CO2</sub>	26.90 × 10 <sup>-3</sup> m <sup>3</sup> /kgatom [20]
(Σv) <sub>W</sub>	12.70 × 10 <sup>-3</sup> m <sup>3</sup> /kgatom [20]

$D_{ij}$ : diffusivity of component  $i$  in component  $j$  [m<sup>2</sup>/s]  
 $D_{i\text{-mixture}}$ : diffusivity of component  $i$  in mixture [m<sup>2</sup>/s]  
 $\Sigma(v_k)$ : sum of the atomic volumes for each of the  $k$  species [m<sup>3</sup>/kgatom]  
 $MW_i$ : molecular weight of species  $i$  [g/gmole]  
 $P$ : total pressure [Pa]  
 $T$ : temperature [K]  
 $y_i$ : mole fraction of species  $i$  in the gas phase of ACL [-]

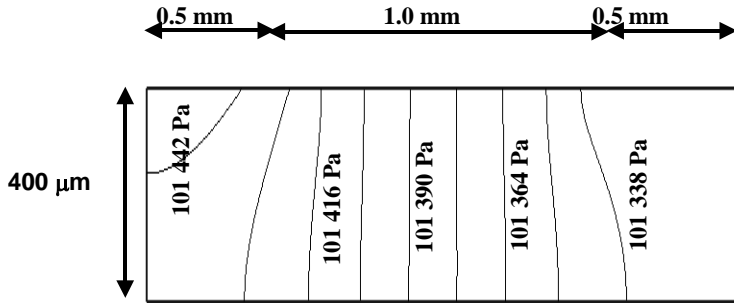


**Figure 3.4. Contour lines of constant pressure in the anode catalyst layer for Case 2 in Table 3.6**

It is worth mentioning that by increasing the catalyst thickness the amount of ZrP and Pt/C were increased. In all cases feed flow rate was kept constant.

**Table 3.6. Summary of various cases**

<b>Case No.</b>	<b>Channel + land width [mm]</b>	<b>Catalyst layer thickness</b>	<b>Half channel width [mm]</b>	<b>Pressure in – out <math>P_{IN} - P_{OUT}</math> [kPa]</b>
1	2	40 $\mu\text{m}$	0.5	1.28
2	2	400 $\mu\text{m}$	0.5	0.129
9	2	1 mm	0.5	0.058
3	11	40 $\mu\text{m}$	0.5	7.85
4	11	400 $\mu\text{m}$	0.5	0.72
8	11	1 mm	0.5	0.23

Although these calculations were made for the anode catalyst layer, it is likely that the same effect might be found for the cathode catalyst layer. That suggests that a cathode catalyst layer thickness could be selected that did not require an excessive amount of parasitic power to operate the air blower.

The electrochemical portion of a fuel cell's performance is indicated by its overpotential. Because the anode overpotentials with hydrocarbons are much larger than those for hydrogen, the performance of direct hydrocarbon fuel cells have been vastly inferior to that of hydrogen fuel cells. Our previous model of a direct propane PAFC [10] showed that the propane anode overpotential was greater than any of the other resistances including the cathode oxygen overpotential. Therefore any change that caused a decrease in the propane anode overpotential would also cause an improvement in fuel cell performance.

Figure 3.5 compares the propane anode overpotential calculated in this work with the previously calculated value for a DPFC having a phosphoric acid electrolyte. In the previous DPFC modeling work, a phosphoric acid electrolyte was chosen for two reasons. The experimental results with a phosphoric acid electrolyte were among the very best obtained in the literature for DPFCs. Second, hydrogen PAFCs are the type of fuel cells with the longest large-scale commercial history. The propane anode overpotential calculated in this work is approximately one-third less than that for the previous PAFC computation. The improvement is attributed to the absence of a film of liquid water around the catalyst site. While this improvement will permit

larger current densities for a given potential, the improvement is not nearly enough to be comparable to hydrogen fuel cells.

One of the important issues in direct hydrocarbon fuel cells is the utilization of the hydrocarbon feedstock. In principle, any unused fuel in the product streams of a hydrogen fuel cell could be used as a heat source for the reforming step needed to produce the hydrogen. There is no such readily available need for unused fuel from a direct hydrocarbon fuel cell. Therefore large values of fuel utilization, propane conversion in this case, are essential. Because the interdigitated flow-fields have the propane feed located in one set of channels and the carbon dioxide product in another set of channels, the feed and product did not mix in the channels so that the maximum propane feedstock was always present at the ACL entrance. Furthermore, the residence time could be chosen, by adjusting the distance between the feed channel and the product channels (width of land plus channel), to obtain large values of conversion and large values of fuel utilization.

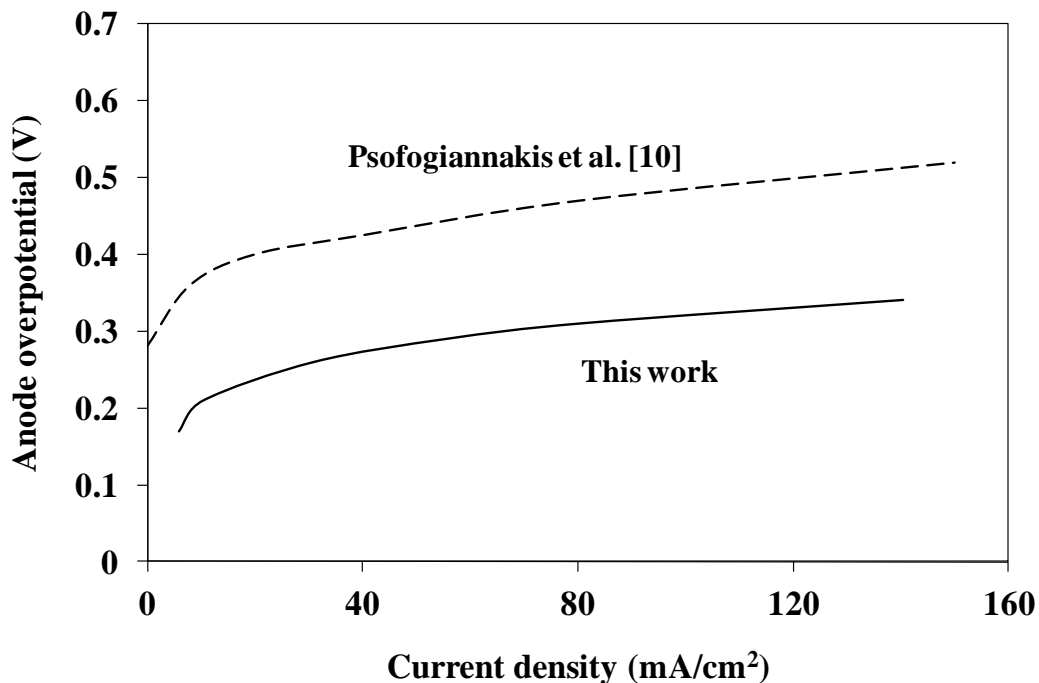


**Figure 3.5. Anode overpotential for a direct propane fuel cell operating at 150°C. Psfogiannakis et al. [10] reported the dashed line for a platinum anode catalyst and an aqueous PAFC electrolyte. The solid line was generated in this work for a platinum anode catalyst and a zirconium phosphate electrolyte.**

Figure 3.6 shows that large values of propane conversion can be obtained by increasing the fuel residence time in the ACL. The calculations are for an ACL with 10 mm land width and 1 mm thickness while it generates 140 mA/cm<sup>2</sup> current density. Longer residence times mean smaller flow-rates of feed gas per unit fuel cell size. For a given flow rate of feed gas, the size of the fuel cell equipment and the capital cost will increase as the flow-rate per unit size of fuel cell decreases.

The thickness of the anode catalyst layer was examined further. Figure 3.7 shows both the pressure gradient  $dP/dL$  in the ACL and the anode overpotential as a function of the ACL thickness. The land length is 10 mm in all cases and overpotential is calculated at the middle of the ACL, i.e. 5mm from the entrance channel. As the thickness of the ACL increases its cross-sectional area for flow perpendicular to the thickness dimension also increases. Therefore the pressure gradient decreases as the ACL thickness increases.

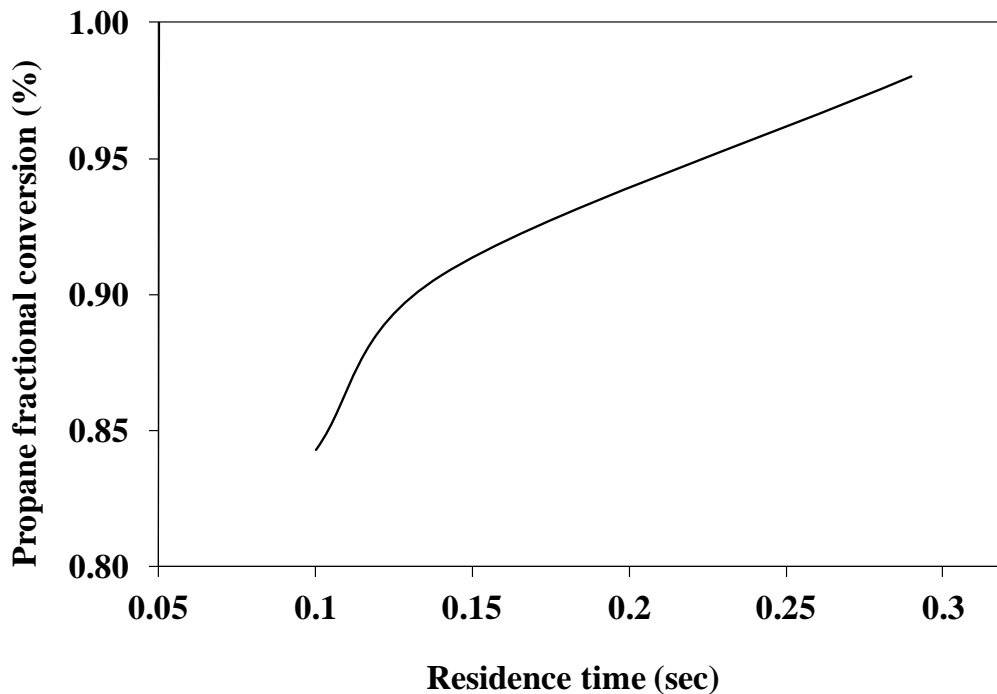


Figure 3.6. Fractional conversion of propane in the anode of a direct hydrocarbon fuel cell versus residence time [s] in the anode catalyst layer at 140 mA/cm<sup>2</sup>

The response of the propane anode overpotential was more complicated. As the ACL thickness increased from 40 to 400  $\mu\text{m}$  the propane anode overpotential decreased. We attribute this result to the presence of a larger quantity of zirconium phosphate in the ACL. Although the ionic current density at the electrolyte interface will be the same for all values of ACL thickness, the number of protons at any cross-sectional position along the  $z_1$  direction will decrease as the ACL thickness increases. Proton hopping between water molecules that are hydrated within the zirconium phosphate is generally accepted as the dominant mechanism for proton conduction. As the quantity of zirconium phosphate in the ACL increases, the quantity of hydrated water (in zirconium phosphate) available for hopping will also increase. That would be expected to decrease the resistance for proton conduction and therefore decrease the anode overpotential. For values of anode thickness, in Figure 3.7, greater than 400  $\mu\text{m}$  the overpotential increased as the ACL thickness increased. This was attributed to the increase in path length that the protons must travel from the reaction site at which they are formed to the electrolyte.

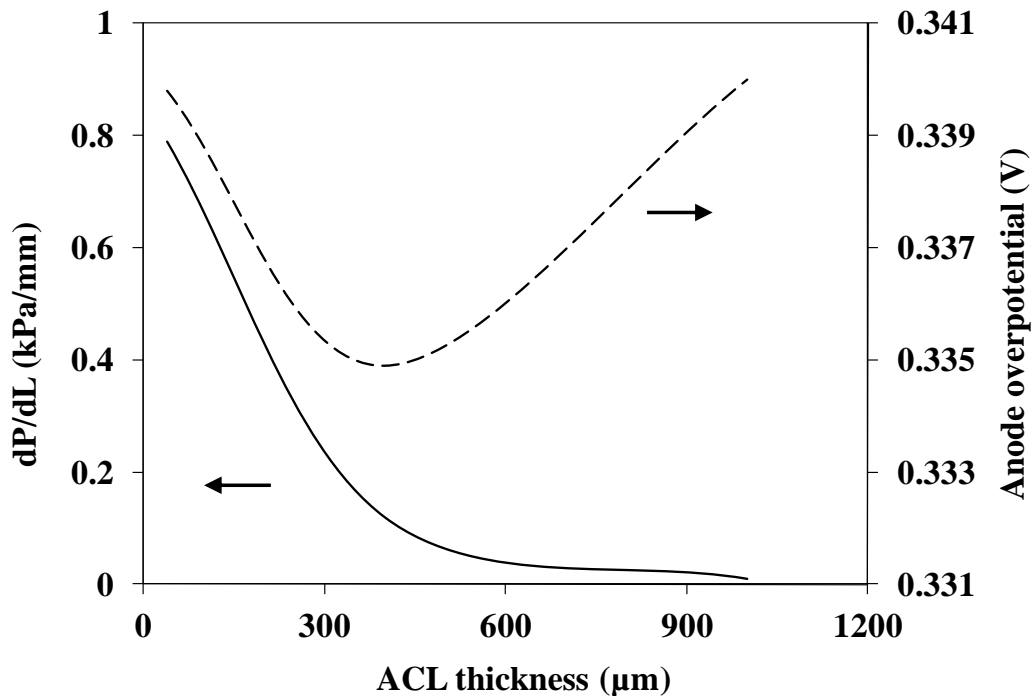
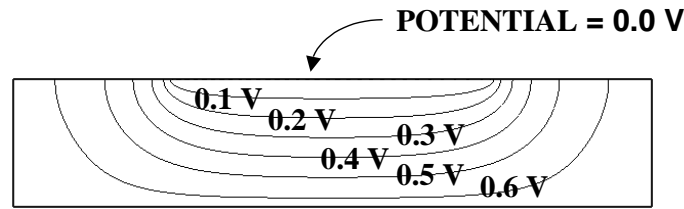


Figure 3.7. Pressure gradient [kPa/mm] and anode overpotential [V] as a function of the thickness of the ACL (anode catalyst layer) [ $\mu\text{m}$ ].

The electrical potential in the electrolyte phase within the anode catalyst layer is shown in Figure 3.8. Since the anode is the electrode where ionization of hydrogen atoms occurs, it has been



assigned the potential of the hydrogen half-cell reaction, 0.0 V. The constant potential contours are located symmetrically in the anode catalyst layer.

**Figure 3.8. Electrical potential profile in the electrolyte phase of the anode catalyst layer**

### 3.5. Conclusion

The particular DPFC anode modeled in this work was shown to have improved performance compared to previous DPFC results (experimental and modeling). The model described here was for the same reaction (propane oxidation), with the same catalyst (platinum), and the same reaction parameters (same  $j_0$  value at the same temperature) as for the previous model [10]. Different reaction conditions (100% gas phase at 150°C), different electrolyte (zirconium phosphate), and a different reactor configuration (interdigitated flow-fields and a thicker catalyst layer) were used. The observed one-third decrease in the anode overpotential was attributed primarily to the absence of aqueous liquids at the 150°C operating temperature. A necessary requirement for this achievement was the acceptable proton conductivity of the zirconium phosphate electrolyte at 150°C. A large fuel-utilization (in excess of 95% propane conversion) was obtained. One factor was the use of interdigitated flow-fields that prevented the carbon dioxide product from diluting the propane concentration at the inlet to the ACL. The other factor was the adjustment of the propane residence time in the ACL. A small pressure drop along the length of the ACL was achieved by increasing the thickness of the ACL (and thereby increasing the cross-sectional area for gas flow). The other benefit of increased catalyst thickness was that the same amount of catalyst was spread more thinly over a larger surface area, thereby creating additional catalyst sites.

### 3.6. Acknowledgement

Financial assistance from the Natural Sciences and Engineering Research Council of Canada and the Ontario Ministry of Research and Innovation (OFCRIN) is gratefully acknowledged.

### 3.7. Nomenclature

$A_{av}$ : anode catalyst face surface area per unit of reactor volume, [ $m^{-1}$ ]

$c$ : total concentration of the gas mixture [ $gmole/m^3$ ]

$c_{H^+}$ : concentration of proton in the electrolyte phase of ACL [ $gmole/m^3$ ]

$D_p$ : effective particle diameter [m]

$D_{ij}$ : diffusivity of component i in component j [ $m^2/s$ ]

$D_{i-mixture}$ : diffusivity of component i in mixture [ $m^2/s$ ]

$D_{P-M}$ : diffusivity of propane in the gas mixture [ $m^2/s$ ]

$D_{CO_2-M}$ : diffusivity of CO<sub>2</sub> in the gas mixture [ $m^2/s$ ]

$D_{W-M}$ : diffusivity of water in the gas mixture [ $m^2/s$ ]

$D_{H^+}$ : diffusivity of proton in ZrP phase of ACL [ $m^2/s$ ]

$F$ : Faraday's constant, 96485 [Coulombs/mol charge]

$j_0$ : exchange current density [ $A/m^2$ ]

$MW_i$ : molecular weight of species i [g/gmole]

$n_c$ : moles of charges per mole of species involved in the overall reaction [mol charge/mol species]

$P$ : total pressure [Pa]

$(r_{Prot})_{AN}$ : rate of production of protons in the anode per unit volume [ $A/m^3$ ]

$R$ : universal gas constant [ J/(mol K) ]

$T$ : temperature [K]

$t$ : time [s]

$u$ : velocity of gas mixture [m/s]

$y_i$ : mole fraction of species i in the gas phase of ACL [-]

#### Greek letters:

$\alpha_A$  and  $\alpha_C$ : anodic and cathodic charge transfer coefficients,

$\eta$ : overpotential at the anode [Volt]

$\varepsilon$ : void fraction in the ACL

$\varepsilon_{ZrP}$ : ZrP fraction in the ACL

$\rho$ : mass density of gas mixture [ $\text{kg}/\text{m}^3$ ]

$\rho_K$  = mass density of species k [ $\text{kg}/\text{m}^3$ ]

$\mu$ : dynamic viscosity of gas mixture [ $\text{kg}/\text{m}\cdot\text{s}$ ]

$\sigma_{ZrP}^{EFF}$ : effective ionic conductivity in the electrolyte phase of the ACL [S/m]

$\Phi_{ZrP}$  : electrical potential in the electrolyte phase of the ACL [Volt]

$\Sigma(v_K)$ : sum of the atomic volumes for each of the k species [ $\text{m}^3/\text{kgatom}$ ]

### **Subscripts and Superscripts:**

A: anode

C: cathode

$\text{CO}_2$ : carbon dioxide

EFF: effective

i: species

P: propane

W: water

### **Abbreviations:**

ACL: anode catalyst layer

DPFC: direct propane fuel cell

FEM : finite element method

PAFC : phosphoric acid fuel cells

PEM: polymer electrolyte membrane or proton exchange membrane

PEMFC: polymer electrolyte membrane or proton exchange membrane fuel cell

PTFE: polytetrafluoroethylene

ZrP: zirconium phosphate

### 3.8. References

- (1) Anonymous Honda FCX Clarity - Vehicle Specifications - Official Web Site. <http://automobiles.honda.com/fcx-clarity/specifications.aspx> (accessed 5/27/2009, 2009).
- (2) Sax, N.I.; Dangerous properties of industrial materials, 5<sup>th</sup> ed. Van Nostrand – Reinhold, New York, p. 806.
- (3) Gupta, Ram B.; Edited by, In *Hydrogen fuel: production, transport, and storage*; CRC Press: New York, 2009; page 10.
- (4) Liebhafsky, H.A.; E.J. Cairns, E.J. The Direct Hydrocarbon Fuel Cell with Aqueous Electrolytes, in *Fuel Cells and Fuel Batteries*, Wiley, New York, 1968, pp. 458-523.
- (5) Bockris, J.O'M.; Srinivasan, S. Electrochemical Combustion of Organic Substances, in *Fuel Cells: Their Electrochemistry*, McGraw-Hill, New York, 1969, pp. 357-411.
- (6) Cairns, E.J. The Anodic Oxidation of Hydrocarbons and the Hydrocarbon Fuel Cell, *Adv. Electrochem. Electrochem. Eng.* **1971**, 8, 337-391.
- (7) Bagotzky, V.S.; Vassiliev, Yu.B.; Khazaova, O.A. Generalized scheme of chemisorption, electrooxidation and electroreduction of simple organic compounds on platinum group metals. *J. Electroanal. Chem.* **1977**, 81, 229–238.
- (8) Hahn, F.; Melendres, C.A. Anodic oxidation of methane at noble metal electrodes: an 'in-situ' surface enhanced spectroelectrochemical study. *Electrochim. Acta*, **2001**, 46, 3525–3534.
- (9) Savadogo, O.; Varela, F.J.R. Low-temperature direct propane polymer electrolyte membranes fuel cell (DPFC). *J. New Mater. Electrochem. Sys.* **2001**, 4, 93–97.
- (10) Psfogiannakis, G.; Bourgault, Y.; Conway, B.E.; Ternan, M. Mathematical model for a direct propane fuel cell. *J. Appl. Electrochem.* **2006**, 36, 115–130.
- (11) Psfogiannakis, G.; St. Amant, A.; Ternan, M. Methane oxidation mechanism on Pt(111): A cluster model DFT study. *J. Phys. Chem. B.* **2006**, 24593–24605.
- (12) Grubb, W.T.; Michalske, C.J. A high performance propane fuel cell operating in the temperature range of 150 - 200°C. *J. Electrochem. Soc.* **1964**, 111, 1015–1019.
- (13) Zhang, J.; Zhong, X.; Zhang, J.; Tnag, Y.; Song, C.; Navessin, T.; Shi, Z.; Song, D.; Wang, H.; Wilkenson, D.; Liu, Z.S.; Holdcroft, S.; High temperature PEM fuel cells. *J. Power Sources* **2006**, 160, 872-891.

- (14) Thakkar, R.; Heemanshu, P.; Chudasama, U.; A comparative study of proton transport properties of zirconium phosphate and its metal exchanged phases. *Bull. Mater. Sci.* **2007**, *30*, 205-209.
- (15) Park, Y.I.; Kim, J.D.; Nagai, M.; High proton conductivity in ZrP-PtFE composites. *J. Mater. Sci.* **2000**, *19*, 1735-1738.
- (16) Si, Y.; Jiang, R.; Lin, J.C.; Kunz, H.R.; Fenton, J.M.; *J. Electrochem. Soc.* **2004**, *151*, 1820-1824.
- (17) Mathias, M.F.; Makhari, R.; Gasteiger, H.A.; Conley, J.J.; Fuller, T.J.; Gittleman, C.J.; Kocha, S.S.; Miller, D.P.; Mittelsteadt, C.K.; Xie, T.; Yan, S.G.; Yu, P.T. Two fuel cell cars in every garage. *Interface*, **2005**, *14*(3), 24 – 35.
- (18) Wood, D.L.; Yi, J.S.; Nguyen, T.V. Effect of direct liquid water injection and interdigitated flow field on the performance of proton exchange membrane fuel cells. *Electrochim. Acta* **1998**, *24*, 3795–3809.
- (19) Yan, W.M.; Mei, S.C.; Soong, C.Y.; Liu, Z.S.; Song, D. Experimental study on the performance of PEM fuel cells with interdigitated flow channels. *J. Power Sources* **2006**, *160*, 166–122.
- (20) Troup, J.M.; Clearfield, A. On the mechanism of ion exchange in zirconium phosphates: Refinement of the crystal structure of  $\alpha$ -zirconium phosphate. *Inorg. Chem.* **1977**, *16*, 3311-3314.
- (21) Poojay, D.M.; Shpeizer, B.; Clearfield, A. X-ray powder structure and Rietveld refinement of  $\gamma$ -zirconium phosphate,  $Zr(PO_4)(H_2PO_4) \cdot 2H_2O$ . *J. Chem. Soc. Dalton Trans.* 1995, 111-113.
- (22) Park, Y.I.; Kim, J.D.; Nagai, M. High proton conductivity in ZrP-PTFE composites. *J. Mater. Sci. Lett.* **2000**, *19*, 1735-1738.
- (23) Silva, V. S.; Ruffmann, B.; Vetter, S.; Mendes, A.; Madeira, L. M.; Nunes, S. P. Characterization and application of composite membranes in DMFC. *Catal Today* **2005**, *104*, 205-212.
- (24) Sang, S.; Wu, Q.; Huang, K. J. Preparation of zirconium phosphate (ZrP) / Nafion 1135 composite membrane and  $H^+/VO^{2+}$  transfer property investigation. *J. Membr. Sci.* **2007**, *305*, 118-124.

- (25) Bockris, O'M.; Gileadi, E.; Stoner, G.E. Anodic oxidation of saturated hydrocarbons. Mechanistic study. *J. Phys. Chem.* 1969, 73, 427-434.
- (26) Hecht, F.; Pironneau, O.; LeHyaric, A. ; Ohtsuka, K. FreeFEM<sup>++</sup> Version 2.24-2-2, [http : // www . freefem . org / ff++](http://www.freefem.org/ff++).
- (27) Bernadi, D.M.; Verbrugge, M.W. A mathematical model of the solid-polymer-electrolyte fuel cell. *J., Electrochem. Soc.* **1992**, 139, 2477-2491.
- (28) Fuller, E.N.; Shettler, P.D.; Giddings, J.C. New method for the prediction of binary gas-phase diffusion coefficients. *Ind. Eng. Chem.* **1966**, 58 [May], 19-27.

## CHAPTER 4

---

# COMPUTATIONAL MODELING OF A DIRECT PROPANE FUEL CELL<sup>1</sup>

H. Khakdaman, Y. Bourgault, M. Ternan

### ABSTRACT

The first two dimensional mathematical model of a complete direct propane fuel cell (DPFC) is described. The governing equations were solved using FreeFEM<sup>++</sup> software that uses finite element methods. Robin boundary conditions were used to couple the anode, membrane, and cathode sub-domains successfully. The model showed that a polytetrafluoroethylene (PTFE) membrane having its pores filled with zirconium phosphate (ZrP-PTFE), in a DPFC at 150°C performed much the same as other electrolytes: Nafion, aqueous H<sub>3</sub>PO<sub>4</sub>, and H<sub>2</sub>SO<sub>4</sub> doped polybenzimidazole, when they were used in DPFCs. One advantage of ZrP-PTFE at 150°C is that it operates without liquid phase water. As a result corrosion will be much less severe and it may be possible for non-precious metal catalysts to be used. Computational results showed that the thickness of the catalyst layer could be increased sufficiently so that the pressure drop between the reactant and product channels of the interdigitated flow fields is small. By increasing the width of the land and therefore the reactant's contact time with the catalyst it was possible to approach 100% propane conversion. Therefore fuel cell operation with a minimum concentration of propane in the product stream should be possible. Finally, computations of the electrical potential in the ZrP phase, the electron flux in the Pt/C phase, and the overpotential in both the anode and cathode catalyst layers showed that serious errors in the model occurred because proton diffusion, caused by the proton concentration gradient, was neglected in the equation for the conservation of protons.

---

<sup>1</sup> This paper was published in *Journal of Power Sources* 196, 2011, 3186–3194

#### 4.1. Introduction

Several advantages are obtained when hydrocarbons are the fuel used directly at the anode of a fuel cell. The capital cost for processing equipment needed to produce hydrogen or methanol can be eliminated. The infrastructure to deliver hydrocarbons is already in place (natural gas pipelines in urban areas and commercial trucking systems for delivery of LPG and diesel fuel in rural areas). A substantial additional capital cost for delivery systems would be required if hydrogen and/or methanol were to become equally accessible. Furthermore, the conversion energy inefficiencies (e.g. endothermic heat required for steam reforming) are eliminated. Storage of liquid hydrocarbons is also much more energy efficient and convenient than that of hydrogen.

Although hydrocarbons have many advantages they also have one major disadvantage compared to hydrogen or methanol. Hydrocarbon reaction rates (current densities) in fuel cells are more than one order of magnitude slower than those of hydrogen or methanol.

Extensive fuel cell research using hydrocarbons as the fuel was performed in the 1959– 1968 period. That work has been summarized in three reviews, Liebhafsky and Cairns [1], Bockris and Srinivasan [2], and Cairns [3]. Different hydrocarbons such as normal paraffins (methane to n-hexadecane), olefins (ethylene, propylene and 1-butene), gasoline and diesel have been investigated as the fuel cell feed. An overview [1] of work during the 1959 – 1968 period shows that: (1) normal alkanes have been the most frequently used fuels; (2) most electrolytes were aqueous acids; (3) platinum has been the favourite electrocatalyst; and (4) cell potentials have been low, which is a serious drawback.

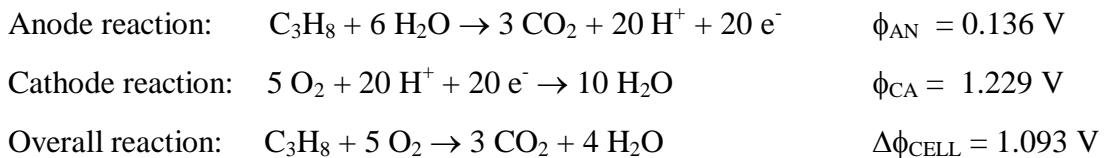
Work in our laboratory is directed toward improving the viability of direct hydrocarbon fuel cells by combining several strategies:

- 1- The first is the selection of a membrane that is capable of operation at a temperature of at least 150°C to ensure that no water is present in the liquid phase. The membrane is composed of two components, a porous polytetrafluoroethylene (PTFE) that contains zirconium phosphate (ZrP) in its pores. It was chosen for this research because it has demonstrated reasonable performance when operated at a 120°C in a hydrogen fuel cell

[4]. In the absence of liquid water, corrosion problems are expected to decrease dramatically and it may be possible to replace precious metal catalysts with less expensive ones. The model described here uses Pt/C catalysts for both anode and cathode because reaction rate data were available in the literature. If the ZrP-PTFE membrane investigated here is shown to be suitable, then a future search for non-precious metal catalysts may be appropriate.

- 2- The use of interdigitated flow fields has at least two desirable features [5,6]. First, the partial pressure of the reactants all along the feedstock channels can be maintained constant at their values in the feedstock. In the more common serpentine flow-fields, reactants are diluted by the products that enter the same channel. Therefore, the partial pressures of the reactants decrease as reaction proceeds and more products are produced. Second, the width of the catalyst layer can be increased thereby increasing the reactor length and the residence time in contact with the catalyst. In principle, the conversion could approach 100%, thereby minimizing the concentration of un-reacted hydrocarbons in the product stream.

This work describes the first two-dimensional model of a complete direct propane fuel cell (DPFC). Both anode and catalyst layers contain two solid phases, a Pt/C phase that conducts electrons and a ZrP phase that conducts protons. The ZrP-PTFE membrane conducts protons through the ZrP that fills the pores. There are no other components in the membrane layer. The following reactions proceed in a DPFC assuming complete propane conversion. The electrical potential values shown are the standard reversible electrochemical potentials at 25°C:



The generation of electrical energy in rural areas is our target application for DPFCs. The cost of delivering electrical energy to rural areas is substantially greater than to urban areas, because longer transmission lines are required to serve a comparatively small number of customers.

Therefore more costly fuel cells can be justified for rural areas than for urban areas. In addition, the infrastructure to deliver liquefied petroleum gas (LPG) or propane to rural areas already exists, because LPG is one of the fuels used for heating in rural areas.

## 4.2. Model Development

A schematic of a typical DPFC is illustrated in Figure 4.1. The cell is composed of two bi-polar plates, two catalyst layers and a membrane layer. The cathode bi-polar plate in Figure 4.1 shows two sets of channels, one for reactants and one for products that are connected to each other through the catalyst layer. The catalyst layers can be thicker when using interdigitated flow fields than when using serpentine flow fields. Thicker catalyst layers make it possible to have a better dispersion of catalyst (more reaction sites).

A cross sectional view of the cell is shown in Figure 4.2. Because of the symmetry of the interdigitated flow field, the modeling domain is defined to be from the middle of a feed channel to the middle of its adjacent product channel. It contains the membrane electrode assembly (MEA) including both the anode and cathode catalyst layers and the membrane layer.

### 4.2.1. Governing equations

Anode and cathode catalyst layers are composed of three phases: reactants and products in the gas phase, solid ZrP electrolyte, and solid catalyst (Pt/C). The membrane layer also contains solid ZrP as well as PTFE. Because different variables in different phases are of interest, a multi-fluid volume averaging method has been used [8]. In this method, spatial averaging is performed for each single phase within a multiphase control volume. Also, the extensive phase-averaged quantities are related to the intensive phase-averaged amounts and phase fractions. For example, the phase-averaged density for the gas phase in a control volume can be calculated by multiplying the gas phase density by its volume fraction in the control volume, as written in Eq. (4-1)

$$\rho_{G, av} = \varepsilon_G \times \rho_G \quad (4-1)$$

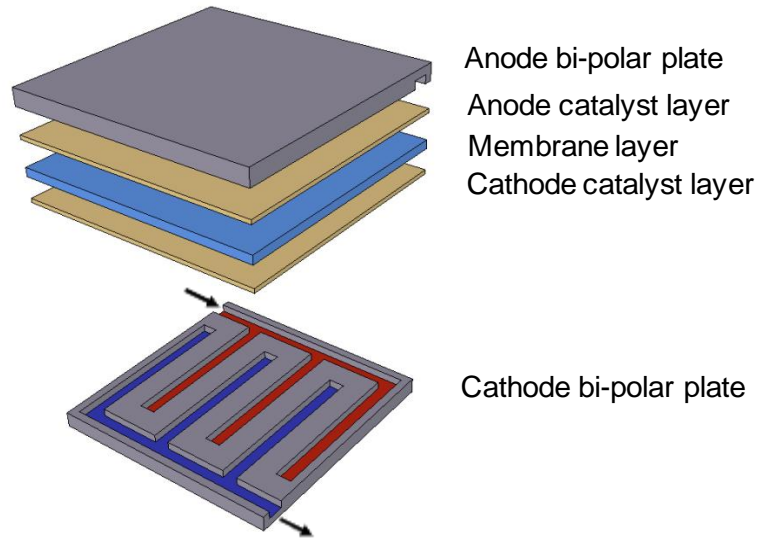


**Figure 4.1. A direct propane fuel cell with interdigitated flow field**

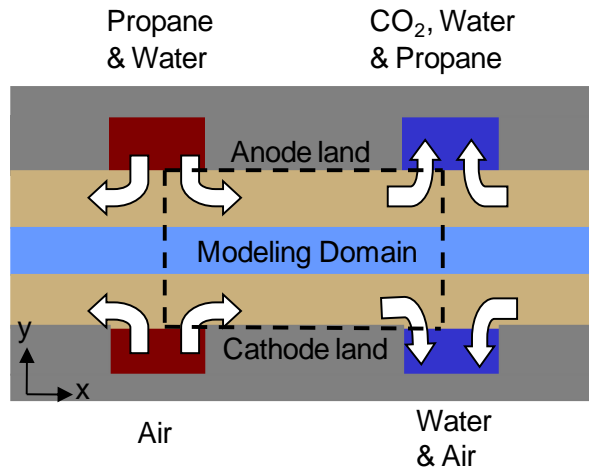


**Figure 4.2. Modeling domain containing anode and cathode catalyst layers and electrolyte layer**

Therefore, phase-averaged quantities were used in the governing equations for the solid and gas phases. Conservation of mass, momentum, and species for the gas phases in the anode and cathode are shown in Tables 4.1 and 4.2 respectively. These tables also include equations for the conservation of protons in the ZrP solid phase in each of the layers. The conservation of protons is the only equation that has to be solved for the membrane layer. Because of the relatively large electron conductivity of the Pt/C solid catalyst (the electron conducting phase), conservation of

electrons in the Pt/C phase was not considered. Instead it is assumed that the electrical potential in the Pt/C phase was constant.

**Table 4.1. List of equations for the anode**

<b>Equations</b>	<b>Eq. No.</b>
<b>Conservation of mass:</b>	
$\partial (\varepsilon_G \rho_G) / \partial t = -\nabla \cdot (\varepsilon_G \rho_G \mathbf{u}) - MW_{C3} j_A / zF - 6MW_{H2O} j_A / zF + 3MW_{CO2} j_A / zF$	(4-2)
<b>Conservation of momentum:</b>	
$-\nabla P = 150 [\mu_G (1 - \varepsilon_G)^2 / D_p^2 \varepsilon_G^3] \mathbf{u}$	(4-3)
<b>Conservation of non-charged species:</b>	
Gas phase:	
$\partial (\varepsilon_G c_G y_{C3}) / \partial t = -\nabla \cdot (\varepsilon_G c_G \mathbf{u} y_{C3}) - \nabla \cdot (J_{C3}) - j_A / zF$	(4-4)
$\partial (\varepsilon_G c_G y_{H2O}) / \partial t = -\nabla \cdot (\varepsilon_G c_G \mathbf{u} y_{H2O}) - \nabla \cdot (J_{H2O}) - 6 j_A / zF$	(4-5)
<b>Conservation of charge:</b>	
For ionic current: $\nabla \cdot (\varepsilon_{ELY} \sigma_{ELY} \nabla \Phi_{ELY, A}) = -j_A$	(4-6)
<b>Butler-Volmer equation:</b>	
$j_A = j_{0,A} A_{Pt} [\exp(\alpha_A F \eta_A / RT) - \exp(-\alpha_C F \eta_A / RT)]$	(4-7)
where, $j_{0,A} = j_{0-ref, C3Ox} (p_{C3} / p_{C3, ref}) \exp[(\Delta G_{C3Ox}^\ddagger / R)(1/T_{ref} - 1/T)]$	(4-8)
$\eta_A = \Delta \Phi_A - \Delta \Phi_{EQ, A} = (\Phi_{Pt, A} - \Phi_{ELY, A}) - (\Phi_{Pt-EQ, A} - \Phi_{ELY-EQ})$	(4-9)

Note:  $j$  in Chapters 4 and 5 were shown by  $r_{Prot}$  in Chapter 3.

**Table 4.2. List of equations for the cathode**

<b>Equations</b>	<b>Eq. No.</b>
<b>Conservation of Mass:</b>	
$\partial (\varepsilon_G \rho_G) / \partial t = -\nabla \cdot (\varepsilon_G \rho_G \mathbf{u}) - 5MW_{O_2} j_C / zF + 10MW_{H_2O} j_C / zF$	(4-10)
<b>Conservation of Momentum:</b>	
$-\nabla P = 150 [\mu_G (1 - \varepsilon_G)^2 / D_p^2 \varepsilon_G^3] \mathbf{u}$	(4-11)
<b>Conservation of Species:</b>	
Gas phase:	
$\partial (\varepsilon_G c_G y_{O_2}) / \partial t = -\nabla \cdot (\varepsilon_G c_G \mathbf{u} y_{O_2}) - \nabla \cdot (\mathbf{J}_{O_2}) - 5j_C / zF$	(4-12)
$\partial (\varepsilon_G c_G y_{N_2}) / \partial t = -\nabla \cdot (\varepsilon_G c_G \mathbf{u} y_{N_2}) - \nabla \cdot (\mathbf{J}_{N_2})$	(4-13)
<b>Conservation of Charge:</b>	
For ionic current: $\nabla \cdot (\varepsilon_{ELY} \sigma_{ELY} \nabla \Phi_{ELY, C}) = -j_C$	(4-14)
<b>Butler-Volmer equation:</b>	
$j_C = j_{0,C} A_{Pt} [\exp(\alpha_A F \eta_C / RT) - \exp(-\alpha_C F \eta_C / RT)]$	(4-15)
where, $j_{0,C} = j_{0-ref, O_2Rd} (p_{O_2} / p_{O_2, ref}) \exp[(\Delta G_{O_2Rd}^\ddagger / R)(1/T_{ref} - 1/T)]$	(4-16)
$\eta_C = \Delta \Phi_C - \Delta \Phi_{EQ, C} = (\Phi_{Pt, C} - \Phi_{ELY, C}) - (\Phi_{Pt-EQ, C} - \Phi_{ELY-EQ})$	(4-17)

The linear form of the Ergun equation has been used to describe momentum conservation because the catalyst layers are essentially packed beds. Conservation of non-charged species in the gas phase accounts for diffusion, convection and reaction phenomena. The consumption rate of the reactant species,  $S_i$ , is related to the volumetric current density,  $j$ , through Faraday's law:

$$S_i = -v_i j / z F \quad (4-18)$$

with  $j$  given by the Butler-Volmer equation:

$$j = j_0 A_{Pt} [\exp(\alpha_A F \eta / RT) - \exp(-\alpha_C F \eta / RT)] \quad (4-19)$$

Where  $j_0$ , the exchange current density, is a function of the reference exchange current density,  $j_{0-ref}$ , and operating temperature and pressure. The reference exchange current density for propane oxidation on platinum has been reported in the literature [9]. In order to calculate the exchange current density at different temperatures the Arrhenius-type expression suggested by Psofogiannakis et al. [10] was used:

$$j_0 = j_{0-ref} \exp [(\Delta G^\ddagger / R)(1/T_{ref} - 1/T)] \quad (4-20)$$

The parameters required to calculate  $j_0$  for propane oxidation at the anode and oxygen reduction at the cathode are reported in Table 4.3. The final expressions for the exchange current densities at the anode and cathode are shown in Eqs. (4-8) and (4-16), respectively.

**Table 4.3. Parameters for Eq. (4-4) [10]**

<b>Parameter</b>	<b>Anode</b>	<b>Cathode</b>
$T_{ref}$ (K)	423	298
$P_{ref}$ (kPa)	101.3	101.3
$j_{0-ref}$ (A cm <sup>-2</sup> Pt)	$1.0 \times 10^{-8}$	$3.8 \times 10^{-13}$
$\Delta G^\ddagger$ (kJ mol <sup>-1</sup> )	90	92

Three mechanisms, diffusion, migration, and convection, are involved in the transport of protons through the electrolyte phase as shown by Nernst-Planck equation [11]:

$$\mathbf{N}_{i, ELY} = - z_i u_i F c_{i, ELY} \nabla \Phi_{ELY} - D_i \nabla c_{i, ELY} + c_{i, ELY} \mathbf{u}_{ELY} \quad (4-21)$$

The first term in Eq. (4-21) describes the migration of protons for which the driving force is the electrical potential gradient. The second term describes the diffusive flux of protons for which the driving force is the concentration gradient (related to the chemical potential gradient). The final term describes the convective flux of protons that is caused by the bulk motion of the solvent. For the stationary membrane of the present system,  $\mathbf{u}_{ELY} = 0$ . Some of the more rigorous models have included both migration and diffusion terms [12-14]. However, the majority of

PEM fuel cell models neglect the concentration gradient and therefore the diffusion term [15-17]. In other words the majority of PEM fuel cell models combine migration and diffusion into a single term for which the driving force is the electrical potential gradient. This work also ignored the concentration gradient and described proton flux as a single term for which the electrical potential gradient was the driving force. That choice had some undesirable consequences that will be discussed in a subsequent section of this communication.

Movement of charged species in the ZrP electrolyte phase produces current that can be quantified by Eq. (4-22): [18]

$$\mathbf{j} = F \sum_i z_i \mathbf{N}_{i, \text{ELY}} \quad (4-22)$$

Substitution of Eq. (4-21) in Eq. (4-22) for a stationary membrane in the absence of a concentration gradient results in:

$$\mathbf{j} = -\sigma_{\text{ELY}} \nabla \Phi_{\text{ELY}} \quad (4-23)$$

where

$$\sigma_{\text{ELY}} = F^2 \sum_i z_i^2 u_i c_{i, \text{ELY}} \quad (4-24)$$

is the conductivity of the ZrP electrolyte.

Electro-neutrality of the entire domain can be expressed by Eq. (4-25):

$$\sum_i \nabla \cdot \mathbf{j}_i = 0 \quad (4-25)$$

As the charged species are electrons and protons, Eq. (4-25) at any location in the domain can be written as:

$$\nabla \cdot \mathbf{j}_{\text{H}^+} = -\nabla \cdot \mathbf{j}_{\text{e}^-} = \mathbf{j} \quad (4-26)$$

where  $j$  is the rate of reaction (volumetric current density) given by the Butler-Volmer equation. Therefore, an equation for the conservation of protons in the absence of electrochemical reactions, which is the situation in the membrane layer, can be written as:

$$\nabla \cdot (\sigma_{\text{ELY}} \nabla \Phi_{\text{ELY, ML}}) = 0 \quad (4-27)$$

The combination of Eqs. (4-23) and (4-26) is shown for the anode as Eq. (4-6) and for the cathode as Eq. (4-14).

#### 4.2.2. Boundary conditions

Figure 4.3 shows the four types of boundary conditions that were used to model the domain; inlets, outlets, walls of the lands, and symmetry boundaries. Table 4.4 shows the values for the boundary conditions. The Ergun equation was solved using the boundary condition values in Table 4.4 for the velocities at the inlets (calculated from inlet flow rates) and the atmospheric pressure boundary condition at the outlets. At the interface between the catalyst layers and lands, (referred to as the wall), the flux of gaseous species is zero. That is also true for the proton flux because protons are not transferred from the catalyst layers to the lands. Instead, a potential difference is set between lands for electrons. The zero flux condition has been applied at the symmetry boundaries, assuming the fuel cell repeats by reflection through these boundaries at the left and right of the computational domain. This reflection is a natural assumption for interdigitated channels.

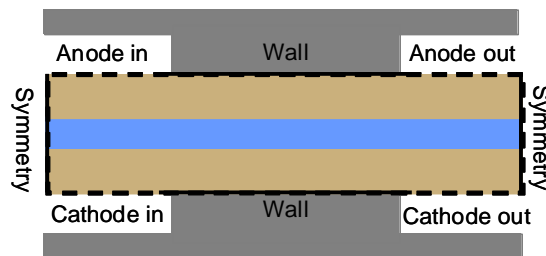


Figure 4.3. Boundaries in the modeling domain

**Table 4.4. List of boundary conditions for the modeling domain**

<b>Anode inlet:</b>			
$u_y = 0.001 - 0.005 \text{ m s}^{-1}$		$\partial \Phi_{\text{ELY}} / \partial y = 0$	
$y_{\text{C}_3} = 0.10$		$y_{\text{H}_2\text{O}} = 0.90$	
<b>Anode outlet:</b>			
$P = 101.3 \text{ kPa}$	$\partial \Phi_{\text{ELY}} / \partial y = 0$	$\partial y_{\text{C}_3} / \partial y = 0$	$\partial y_{\text{H}_2\text{O}} / \partial y = 0$
<b>Cathode inlet:</b>			
$u_y = 0.001 - 0.005 \text{ m}^{-1}$		$\partial \Phi_{\text{ELY}} / \partial y = 0$	
$y_{\text{O}_2} = 1.00$		$y_{\text{H}_2\text{O}} = 0.00$	
<b>Cathode outlet:</b>			
$P = 101.3 \text{ kPa}$		$\partial \Phi_{\text{ELY}} / \partial y = 0$	$\partial y_{\text{O}_2} / \partial y = 0$
<b>Anode/land interface (wall):</b>			
$u_y = 0$	$\partial \Phi_{\text{ELY}} / \partial y = 0$	$\partial y_i / \partial y = 0$	$\Phi_{\text{Pt}} = 0.15 - 0.50 \text{ V}$
<b>Cathode/land interface (wall):</b>			
$u_y = 0$	$\partial \Phi_{\text{ELY}} / \partial y = 0$	$\partial y_i / \partial y = 0$	$\Phi_{\text{Pt}} = 0.9 - 1.2 \text{ V}$
<b>Zero flux boundaries:</b>			
$u_x = 0$		$\partial \Phi_{\text{ELY}} / \partial x = 0$	$\partial y_i / \partial x = 0$
<b>Anode/membrane interface:</b>			
$\epsilon_{\text{ELY}, A} \sigma_{\text{ELY}, A} (\partial \Phi_{\text{ELY}, A} / \partial y) = \sigma_{\text{ML}} (\partial \Phi_{\text{ML}} / \partial y)$			$\Phi_{\text{ELY}, A} = \Phi_{\text{ML}}$
$u_y = 0$			$\partial y_i / \partial y = 0$
<b>Cathode/membrane interface:</b>			
$\sigma_{\text{ML}} (\partial \Phi_{\text{ML}} / \partial y) = \epsilon_{\text{ELY}, C} \sigma_{\text{ELY}, C} (\partial \Phi_{\text{ELY}, C} / \partial y)$			$\Phi_{\text{ELY}, C} = \Phi_{\text{ML}}$
$u_y = 0$			$\partial y_i / \partial y = 0$

The feed composition is known at the inlet of the catalyst layers. It is assumed that no change in the composition of gaseous species will occur after the gas mixture leaves the catalyst bed. Therefore, the gradient of the composition is zero in the direction normal to the catalyst surface at the outlet boundaries. Also, the electrical current is zero in the normal direction of the inlet and outlet boundaries, both for protons and electrons.

### 4.2.3. Model input parameters

The parameters used for the simulations are shown in Table 4.5. To calculate platinum surface area per catalyst volume,  $A_{Pt}$ , that is used in the Butler-Volmer equation it is assumed that a fraction,  $f_{Pt/CAT}$ , of catalyst support surface area,  $A_{CAT}$ , is covered by platinum. Therefore  $A_{Pt}$  can be calculated using Eq (4-28):

$$A_{Pt} = f_{Pt/CAT} \times A_{CAT} \times \rho_{CAT} \quad (4-28)$$

**Table 4.5. Operational, electrochemical and design parameters for simulations**

Property	Value
Temperature, T	423 K
Pressure, P	101.3 k Pa
Charge transfer coefficients, $\alpha_A$ and $\alpha_C$	1.0 [10]
Electrolyte ionic conductivity for ZrP-PTFE, $\sigma_{ELY}$	5.0 S m <sup>-1</sup>
Equilibrium potential of conductor phase at the anode, $\Phi_{Pt-EQ, A}$	0.136 V [1]
Equilibrium potential of conductor phase at the cathode, $\Phi_{Pt-EQ, C}$	1.229 V
Equilibrium potential of electrolyte phase, $\Phi_{ELY-EQ}$	0.136 V
Apparent bulk density of catalyst support, $\rho_{CAT}$	0.259 g <sub>catalyst</sub> mL <sup>-1</sup> <sub>catalyst</sub>
Specific surface area of catalyst support in the anode and cathode, $A_{CAT}$	255 m <sup>2</sup> <sub>catalyst</sub> g <sup>-1</sup> <sub>catalyst</sub>
Gas phase volume fraction in anode and cathode, $\varepsilon_G$	0.5
Electrolyte phase volume fraction in anode and cathode, $\varepsilon_{ELY}$	0.4
Effective particle diameter in anode and cathode, $D_p$	5 $\mu$ m
Land width, $L_w$	1– 6 mm
Anode and cathode thickness, $Th_A$ , $Th_C$	200 – 400 $\mu$ m
Membrane thickness, $Th_M$	100 $\mu$ m
Fluid channels width in bi-polar plates	0.4 mm

#### 4.2.4. Numerical procedure

The software used to solve the two-dimensional partial differential equations is FreeFEM<sup>++</sup>, which was developed by Hecht et al. [19]. It is open-source software based on the Finite Element Method which is capable of handling multi-variable, multi-equation, two and three-dimensional systems and steady state or time dependent problems. In addition, the results calculated using FreeFEM<sup>++</sup>, can be easily exported to ParaView software [20] for post-processing. ParaView is open-source software used for visualization that is quite powerful.

The partial differential equations and the required boundary conditions discussed in sections 4.2.1 and 4.2.2 respectively are rewritten into variational form, and discretized by the Finite Element Method in space. The Euler time stepping method is used to discretize the equations in time with all nonlinear reaction terms taken explicitly and linearized differential terms taken implicitly to increase stability. The partial differential equations are solved one after another in a decoupled fashion. Time steps are performed until a steady-state solution of the fully coupled system of nonlinear equations is reached, usually of the order of a few hundred time-steps. Grid independence of the solution was achieved by computing solutions on sufficiently refined meshes.

A special method was required to couple the solutions on all the layers. One of the main difficulties is the solution of the potential equations for protons over the three layers while matching potentials and fluxes of protons at the membrane-catalyst layer interfaces. Moreover, proton fluxes are zero at the exterior boundary of the whole computational domain suggesting that the rate of proton production in the anode is equal to the rate of proton consumption in the cathode. In an attempt to couple the anode with the membrane, and the membrane with the cathode, the anode and the cathode are coupled together as well. A domain decomposition method with Robin boundary conditions on the potential has been employed successfully to solve the potential equations in the anode, membrane and cathode. In the Robin method, linear combinations of the unknown potentials and their fluxes are used as boundary conditions. For example, Eqs. (4-29) and (4-30) are used as boundary conditions at the anode/membrane interface to solve potential equations in the anode and membrane domains:

$$\varepsilon_{\text{ELY, A}} \sigma_{\text{ELY, A}} (\partial \Phi_{\text{ELY, A}} / \partial y) + \alpha_1 \Phi_{\text{ELY, A}} = \sigma_{\text{ML}} (\partial \Phi_{\text{ML}} / \partial y) + \alpha_1 \Phi_{\text{ML}} \quad (4-29)$$

$$- \sigma_{\text{ML}} (\partial \Phi_{\text{ML}} / \partial y) + \alpha_2 \Phi_{\text{ML}} = - \varepsilon_{\text{ELY, A}} \sigma_{\text{ELY, A}} (\partial \Phi_{\text{ELY, A}} / \partial y) + \alpha_2 \Phi_{\text{ELY, A}} \quad (4-30)$$

where  $\alpha_1$  and  $\alpha_2$  are relaxing parameters which will be eliminated by adding or subtracting equations (4-29) and (4-30). Therefore, the values of these parameters are not physically meaningful. However, in order to enhance the numerical calculations,  $\alpha_1$  and  $\alpha_2$  are considered as the inverse of the anode and membrane volume respectively.

The layers were solved sequentially, with a single iteration of the coupling method at each time step. A Newton method was used to force equal proton production/consumption rates at the anode and cathode.

#### 4.2.5. Model Validation

The model predicts the performance of a DPFC having interdigitated flow fields and a solid ZrP-PTFE electrolyte operating at temperatures of at least 150°C. In order to validate the model, two sets of published experimental data have been chosen for comparison purposes. Savadogo and Varela [21] reported polarization curves for DPFCs with several modified solid electrolytes operating at low temperatures. Grubb and Michalske [9] presented polarization curve data for DPFCs using phosphoric acid as the electrolyte operating at temperatures as high as 200°C.

Figure 4.4 compares the modeling results with the experimental data. Graph (a) in Figure 4.4 shows the performance of a DPFC with a non-modified Nafion 117 solid electrolyte. Although Nafion has a proton conductivity approaching  $10 \text{ S m}^{-1}$ , it has to be used at temperatures of 80°C or less. At elevated temperatures both the liquid phase water content of Nafion membranes and their performance decline substantially. Graph (b) in Figure 4.4 shows Grubb's best results obtained using a DPFC having a liquid phosphoric acid electrolyte. Because there are no experimental data for direct propane fuel cells having zirconium phosphate electrolytes, a comparison was made between results from our model having a zirconium phosphate electrolyte and experimental data obtained with other electrolytes. The comparison in Figure 4.4 indicates

that the zirconium phosphate electrolyte would have results that are somewhat comparable to the other electrolytes. Although the variation in results among the electrolytes shown in Figure 4.4 for direct propane fuel cells are significant, they are minor when they are compared to results from a hydrogen fuel cell.

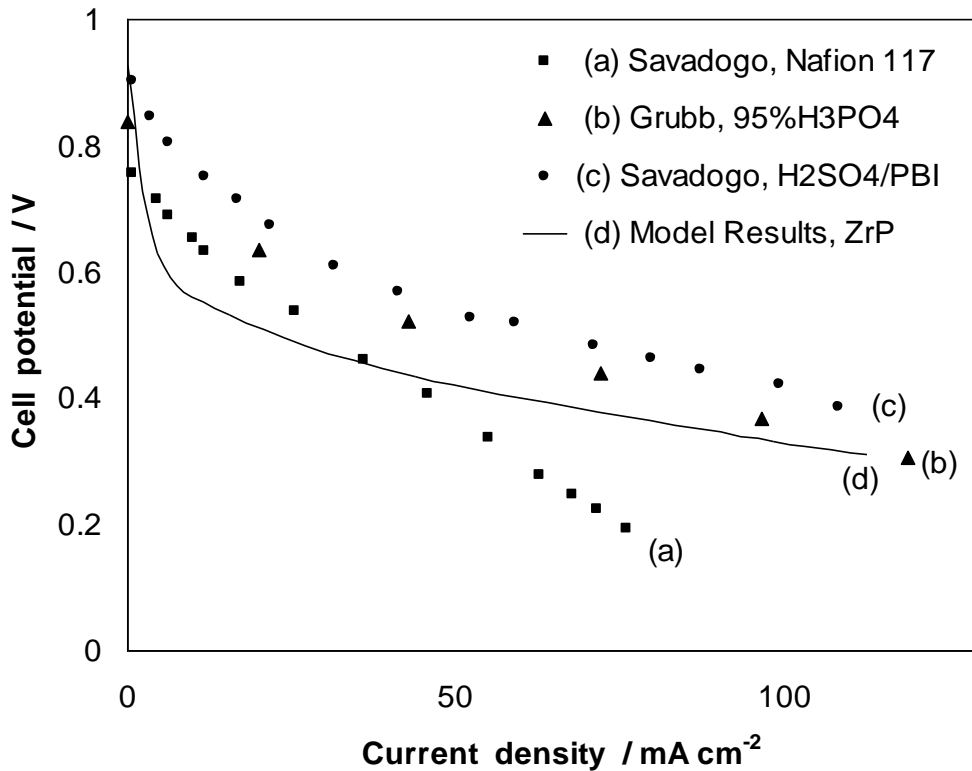


Figure 4.4. Polarization curves of direct propane/oxygen fuel cell using Pt anode and cathode. (a) experimental results [21] using Nafion 117 at 95°C. (b) experimental results [9] using 95% H<sub>3</sub>PO<sub>4</sub> at 200°C. (c) experimental results [21] using H<sub>2</sub>SO<sub>4</sub> doped PBI at 95°C. (d) The present model results for a solid ZrP-PTFE electrolyte at 150°C; the base case study

The different results obtained with the different electrolytes may be related to the various electrolyte conductivities. The proton conductivity of phosphoric acid electrolyte depends on its concentration and on the operating temperature. Dobos has reported the proton conductivity of phosphoric acid at 298K and its temperature variations [22]. Proton conductivity of a 95% H<sub>3</sub>PO<sub>4</sub> at 200 °C is equal to 35 S m<sup>-1</sup>. The best experimental conductivity achieved for ZrP in our

laboratory was approximately  $5 \text{ S m}^{-1}$ . The greater proton conductivity values for Nafion 117 and 95%  $\text{H}_3\text{PO}_4$  result in higher cell potentials at low current densities compared to the ZrP-PTFE electrolyte modeled in this study. However, as current densities increase, the experimental cell potential results decrease more rapidly for Nafion 117 and 95%  $\text{H}_3\text{PO}_4$  compared to the ZrP-PTFE model results. One explanation is that both Nafion and 95%  $\text{H}_3\text{PO}_4$  have at least a partial liquid film around the Pt/C catalyst sites. This leads to larger Ohmic losses compared to a DPFC with solid ZrP-PTFE electrolyte at  $150^\circ\text{C}$  where there is no liquid phase water and no liquid film is present to create a diffusion resistance.

The model prediction in Figure 4.4 indicates that a ZrP-PTFE membrane will give a polarization curve that is generally of the same order of magnitude as those obtained with  $\text{H}_3\text{PO}_3$ , Nafion, and  $\text{H}_2\text{SO}_4$  doped polybenzimidazole (PBI). The difference is that ZrP-PTFE does not need liquid phase water, whereas the others do. Acceptable operation in the absence of liquid water suggests that the highly corrosive environment can be avoided and that a search for a non-precious metal catalyst to replace Pt/C may be warranted.

### 4.3. Results and discussion

The model was employed for two purposes. The effects of some of the physical characteristics of the flow fields (land width) and the MEA (catalyst layer thickness) were examined. It was also used in an attempt to understand proton transport in the ZrP electrolyte phase and electron transport in the Pt/C phase. In addition, the variation of some of the gas phase variables was investigated. These studies are described in this section.

Figure 4.5 shows the effect of land width, i.e. the distance between inlet and outlet channels, on the cell performance. It is apparent that increasing the land width has a small negative effect on the polarization curve. As the reactants flow from an inlet channel towards its adjacent outlet channel within the catalyst layer, the partial pressure of the reactants decreases and that leads to a lower reaction rate and a smaller current production. This can be explained by the dependence of exchange current density on the partial pressure of the reactants in the Butler-Volmer equation.

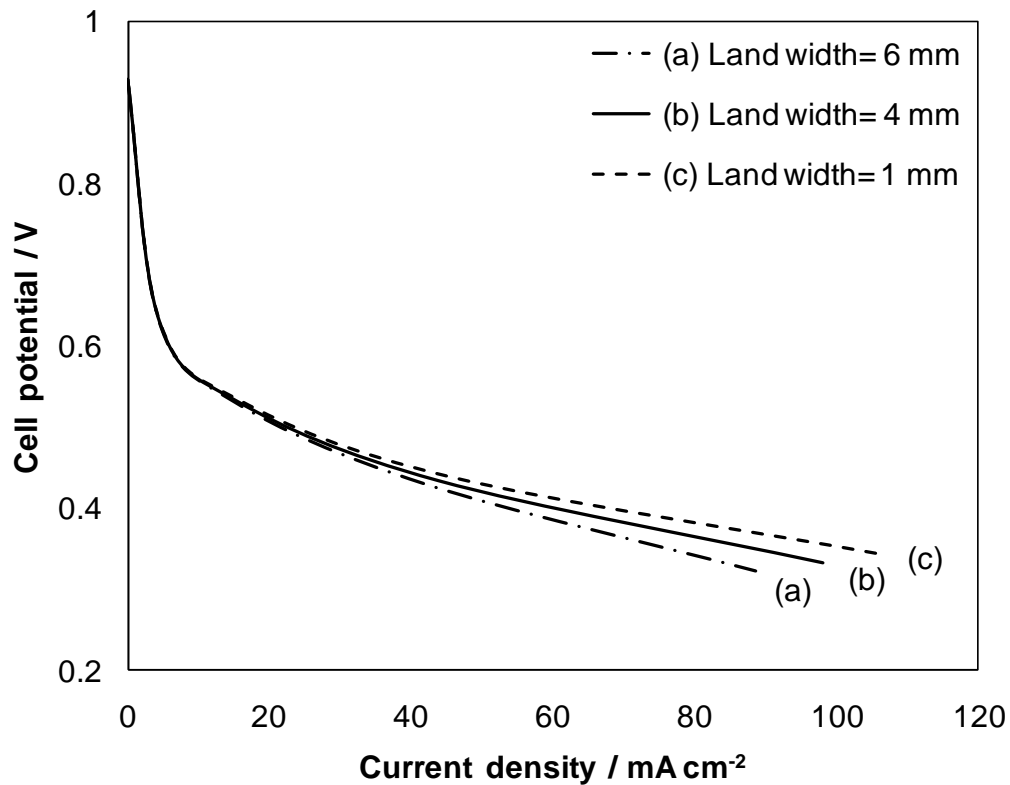


Figure 4.5. Polarization curves of direct propane/oxygen fuel cell showing model results for catalyst thickness of 300 microns at different land widths.

A major concern about the interdigitated flow fields is their higher pressure-drop compared to the conventional serpentine flow fields. However, it has been shown that with interdigitated flow fields, thicker catalyst layers have smaller pressure drops [7]. Large pressure drops are a serious drawback for interdigitated flow fields. This perception is correct for serpentine flow fields using conventional anode catalyst layers of 40  $\mu\text{m}$ . However, by increasing the thickness of the anode catalyst layer to 400  $\mu\text{m}$ , the pressure drop along the land width will decrease. Moreover, an increase in the catalyst thickness results in an improvement in the polarization curve as can be seen in Figure 4.6. Improved dispersion of the metal catalyst should be obtained using a thicker catalyst layer without changing the total amount of catalyst used. An increased dispersion would correspond to a larger number of reaction sites.

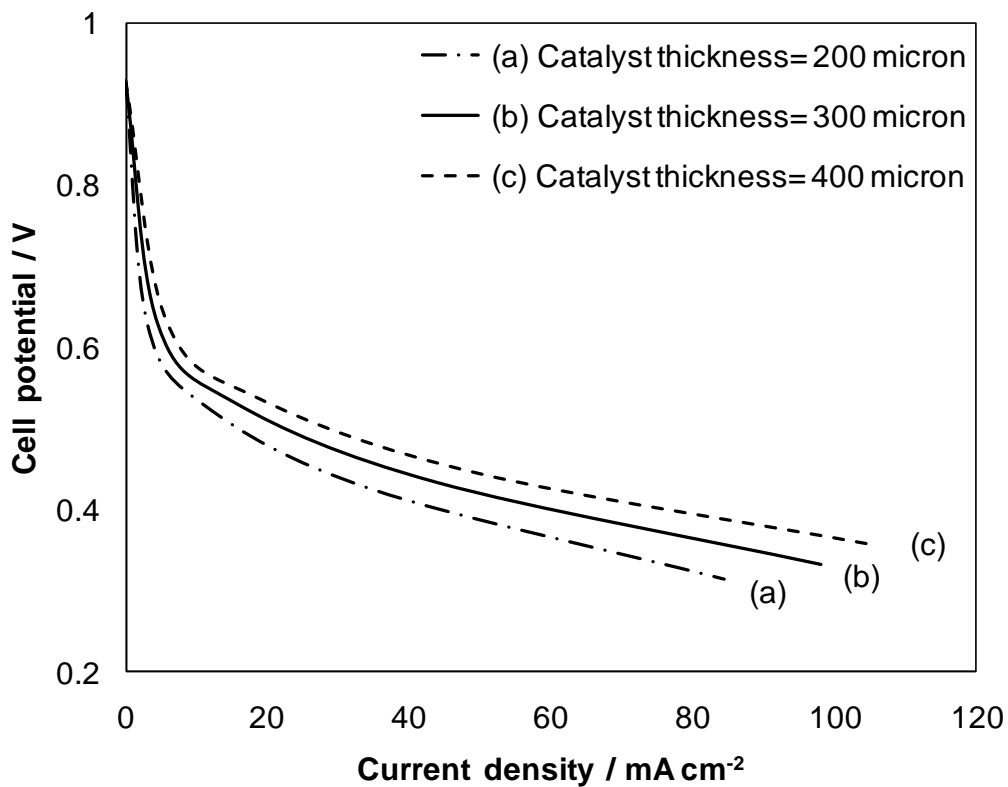
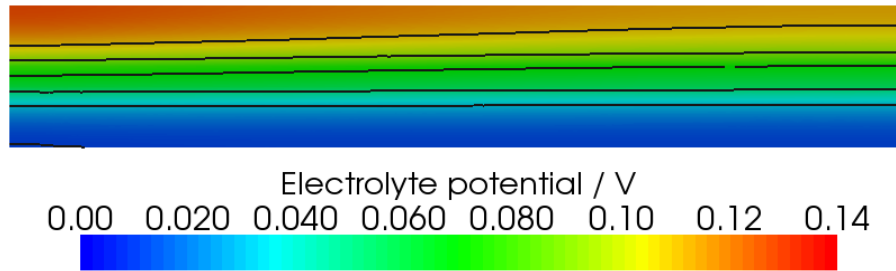


Figure 4.6. Polarization curves of direct propane/oxygen fuel cell showing model results for the land width of 4 mm at different catalyst thicknesses.

Figure 4.7 shows the two-dimensional variation of the electrical potential in the ZrP phase of the entire domain, that is the anode catalyst layer, the membrane layer, and the cathode catalyst layer. The electrical potential at the anode catalyst layer is greater than that at the cathode catalyst layer causing a proton flux from the anode to the cathode. A cross-section of Figure 4.7 is shown in Figure 4.8, where the electrical potential in the ZrP phase is compared with that in the Pt/C phase.



**Figure 4.7. Potential profile for the ZrP phase within the cathode and anode catalyst layers and membrane layer.**

Figure 4.8 shows the following MEA profiles in the y-direction (as defined in Figure 4.2): (a) a comparison of the electrical potential in the Pt/C solid phase with that in the ZrP phase for the anode catalyst layer, (b) the same comparison as in (a) but for the cathode catalyst layer, and (c) the electrical potential profile of the ZrP phase in the membrane layer. As the electrical conductivity in the Pt/C phases is very high, the electrical potential in both of the Pt/C phases in their respective anode and cathode layers are almost constant, as shown by the horizontal dashed lines in Figure 4.8. However, the electrical potential in the ZrP phase varies according to the Eqs. (4-6) and (4-14), as shown by the solid line in Figure 4.8.

The model uses this electrical potential gradient to account for proton migration from the ZrP phase in the anode catalyst layer, through the ZrP phase in the membrane layer, and into the ZrP phase in the cathode catalyst layer. As mentioned previously, neglecting the diffusion term in Eqs. (4-6) and (4-14) is a common assumption used in most PEM fuel cell models.

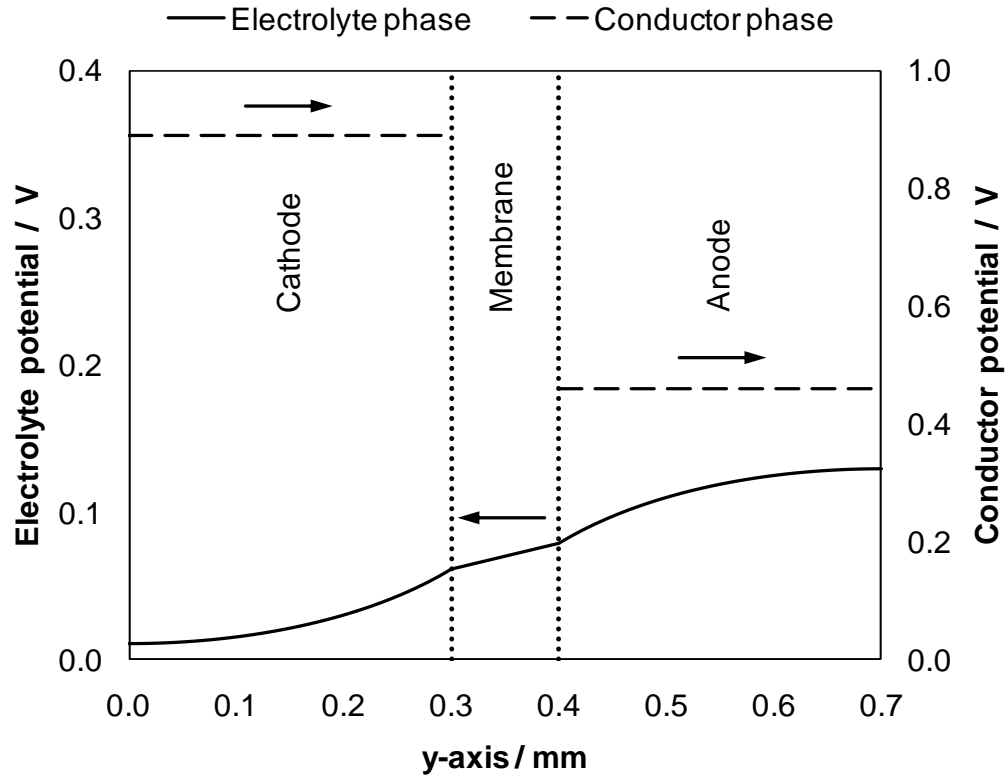


Figure 4.8. Potential profiles in the y-direction for the ZrP and Pt/C phases located at the middle of the domain x-direction for the cathode and anode catalyst layers and membrane layer. The arrows point in the direction of the ordinate scale that applies to each of the three curves

Reasonable predictions of the fuel cell polarization curve were obtained using this assumption, as shown in Figs. 4.4 to 4.6. However, one of the undesirable consequences of this assumption is that the slope of electrical potential in the ZrP phases in the three layers is positive. It should be negative. The correct sign of the slope can be understood from the following reasoning: The potential gradient between anode and cathode drives electrons from the Pt/C phase of the anode to the Pt/C phase of the cathode via the external circuit. If the fuel cell had an aqueous electrolyte, the electrical double layer would have described the difference in electrical potential between the catalyst layers and the electrolyte. Since ZrP has semi-conducting properties [23] the difference in electrical potential between Pt/C and ZrP will be described by a space charge region [24]. As a result the electrical potential in the ZrP phases will be directly related to the electrical potentials in the Pt/C phases that are shown as the dashed lines in Figure 4.8. Therefore the electrical potential in the ZrP phase of the anode catalyst layer must be less than that in the

ZrP phase of the cathode catalyst layer. Therefore the opposite trend, shown in Figure 4.8, cannot be correct. Since negatively charged electrons are driven from the anode to the cathode by the electrical potential gradient (in the Pt/C phases) the corresponding gradient (in the ZrP phases), when correctly calculated, must provide a driving force for positively charged protons from the cathode to the anode. As the electrochemical reaction proceeds protons will accumulate (in the ZrP phase) at the anode until the proton concentration gradient from the anode to the cathode is sufficient to overcome the electrical potential gradient (in the ZrP phases). When that condition is attained, protons will flow through the ZrP phases from the anode to the cathode. The conclusion is that Figure 4.8 has an incorrect sign for the slope of the electrical potential gradient (in the ZrP phase). If the model had included the diffusion term with its concentration gradient in Eq. (4-21) then the sign of the slope in Figure 4.8 would have been correct.

There is an additional issue. From the model there is a small leak of electrons from the cathode to the anode (electron conductivity of membrane is  $10^{-16}$  S/m). Since the electrons are produced at the anode, it might be expected that the leak would be in the opposite direction. Therefore, this feature of the model may be questionable.

It is worth mentioning that the solid line in Figure 4.8 for the electrolyte phase potential shows that the condition of zero proton flux at the lands has been satisfied, and coupling at the membrane/catalyst layers interfaces has been done perfectly.

Figure 4.9 shows that the overpotential predicted by the model at both the membrane/catalyst interfaces is greater than that at their corresponding lands. This prediction by the model is incorrect, as can be seen from the following reasoning at the anode: the overpotential at the anode is given by Eq. (4-9),  $\eta_A = (\Phi_{Pt, A} - \Phi_{ELY, A}) - (\Phi_{Pt-EQ, A} - \Phi_{ELY-EQ}) = (\Phi_{Pt, A} - \Phi_{ELY, A})$  when the equilibrium potential of the ZrP electrolyte,  $\Phi_{ELY-EQ}$ , is been defined to be equal to the equilibrium potential in the Pt/C catalyst  $\Phi_{Pt-EQ, A}$ . According to Figure 4.8, the potential difference  $\Phi_{Pt, A} - \Phi_{ELY, A}$  is greater at the anode catalyst-membrane interface than at the anode catalyst-land interface. That is consistent with the overpotential in Figure 4.9. However, if proton diffusion driven by the proton concentration gradient had been included in the model, then the

electrical potential gradient in the ZrP phases in Figure 4.8 would have been reversed. That would also reverse the slope of the overpotential gradients in Figure 4.9.

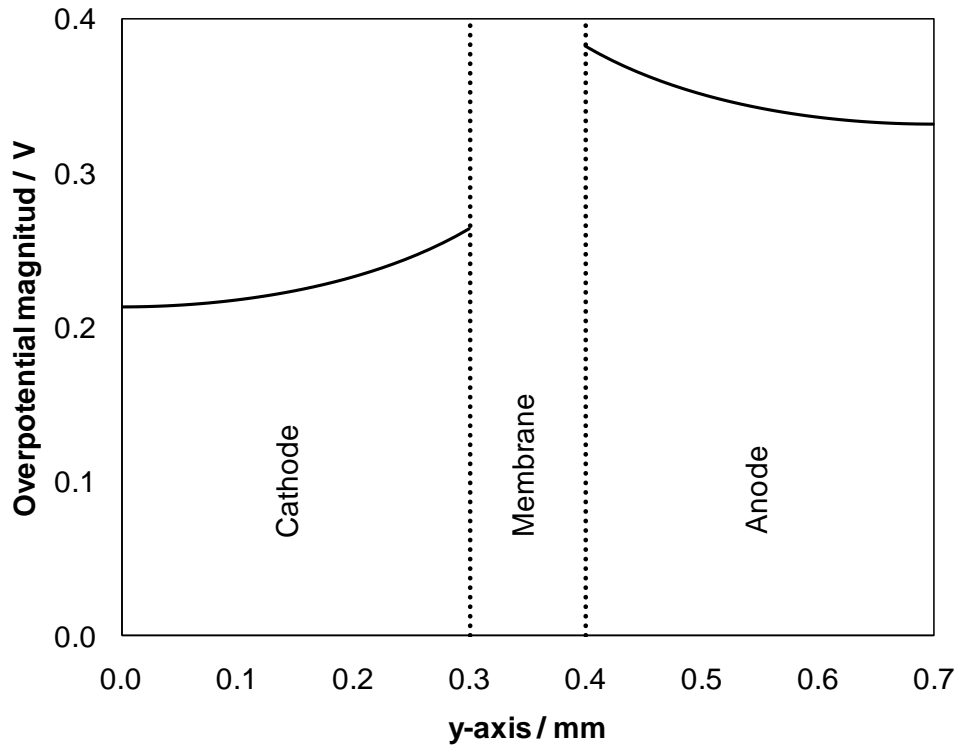


**Figure 4.9. Overpotential profile at the anode and cathode**

Figures 4.10a and 4.10b show the magnitude and direction of proton and electron fluxes respectively. Protons and electrons are produced in the anode and consumed in the cathode. Protons travel through the ZrP-PTFE electrolyte phase from anode to cathode, as shown in Figure 4.10a. Protons are produced throughout the anode catalyst layer. The arrow's length in Figure 4.10a correctly indicate that the proton flux increases as the position in the anode's y-direction changes from the anode catalyst-land interface to the membrane-anode catalyst interface.

Electrons travel from anode to cathode via the external circuit although there is a very small amount of electronic current through the membrane layer. Electron transport also occurs in the Pt/C phase of the catalyst layers. It is the electron transport in the Pt/C phase that is shown in Figure 4.10b. However, the electron flux in Figure 4.10b is shown in the wrong direction. Neglecting the diffusion term in the proton conservation equation caused this incorrect result, as was described previously.

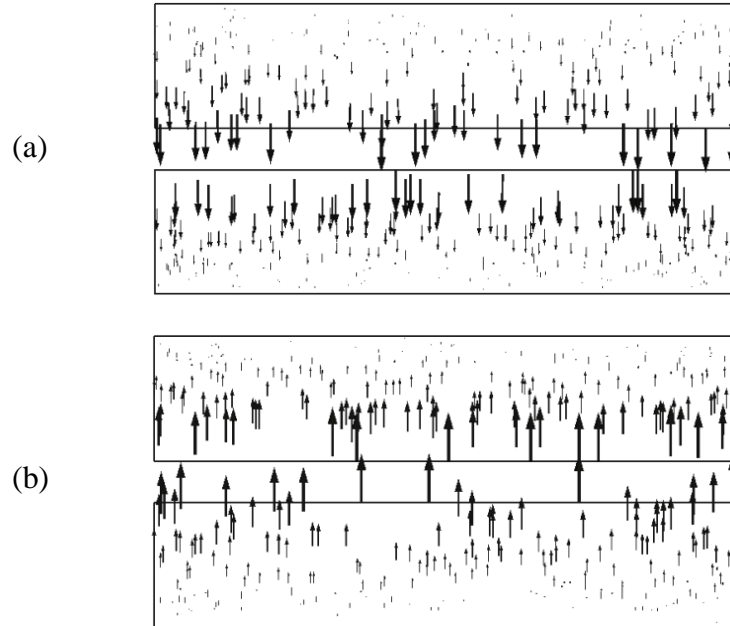


**Figure 4.10. (a) Protonic current from anode to cathode in electrolyte phase. The vectors length indicate the current magnitude which varies from 0 to  $120 \text{ mA cm}^{-2}$  in this case. (b) Electronic current from cathode to anode in electrolyte phase. The vectors length indicate the current magnitude which varies from 0 to  $2e^{-14} \text{ mA cm}^{-2}$  in the same case as Figure 4.10 a.**

Figure 4.11 shows the variation in the propane and oxygen mole fractions at the anode and cathode respectively. The concentrations of the reactants decrease along the land as the reactants flow from the inlet to the outlet. Therefore, changing the land's width can control the conversion of the reactants. This is an important benefit of interdigitated flow fields for DPFCs. Even if the feed channels are dead-ended so that all of the reactants must flow through the catalyst layer, as shown in Figure 4.1, it would be undesirable for un-reacted propane to contaminate the product gas stream that ideally should consist only of carbon dioxide and water vapour. The water

concentration at the anode entrance was specified to exceed the stoichiometric ratio because it is needed for both reaction and to assist proton transport (osmotic drag).

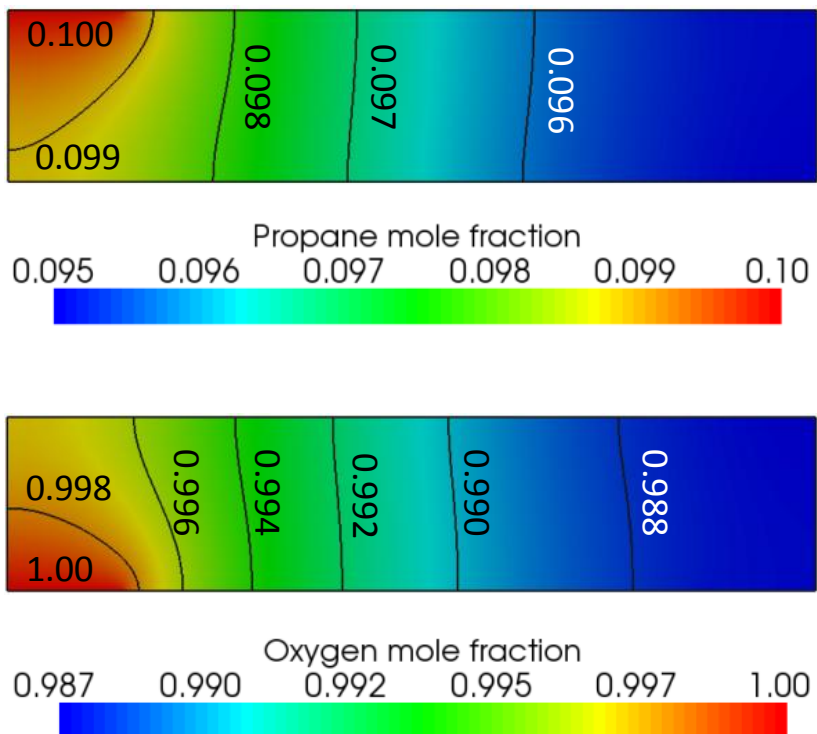


**Figure 4.11. Propane and oxygen mole fraction at the anode and cathode respectively.**

Figure 4.12 shows the velocity vectors in the gas phase of the anode and cathode catalyst layers. Arrows in x-direction on the land represent a slip flow regime in the catalyst layer. This suggests that the Ergun equation describes momentum conservation appropriately, since the catalyst layers have been modeled as packed beds and flow through a packed bed is possible even at the wall of a land. Finally, the small velocity vectors indicate poor catalyst utilization.

Figure 4.13 shows that the propane conversion increases as the land width increases. The fact that 100% propane conversion can be approached with interdigitated flow fields is important. As explained previously un-reacted propane in the product stream would be undesirable. A 100% conversion result is unlikely with a serpentine flow field. In a serpentine flow field the carbon dioxide products would mix with the hydrocarbon feedstock. The smaller propane concentration

in the channels of serpentine flow fields would decrease the driving force that pushes the hydrocarbons into the catalyst layer.

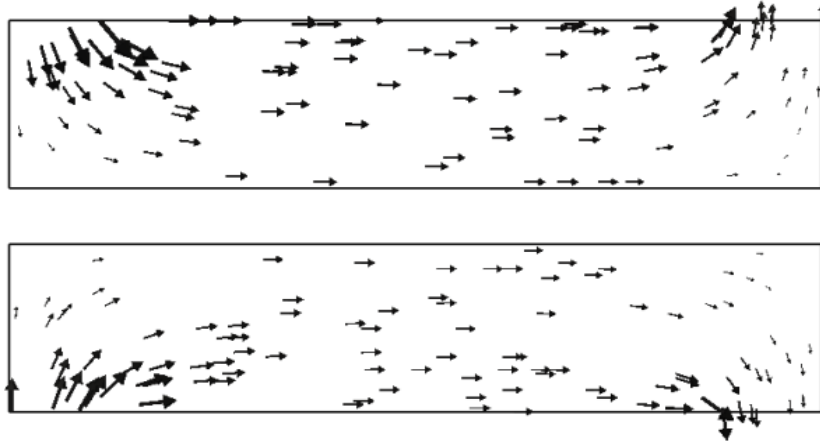


Figure 4.12. Velocity vectors showing movement of fluid in the anode and cathode catalyst layers.

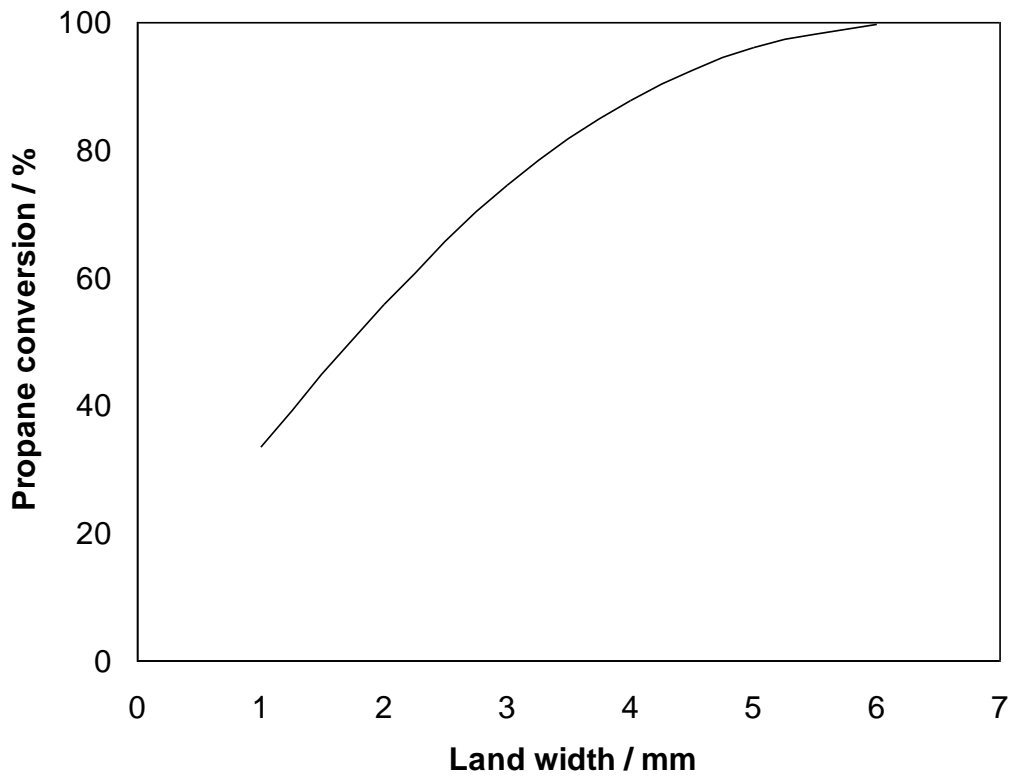


Figure 4.13. Propane conversion at different anode and cathode land widths

#### 4.4. Conclusion

The performance predicted for a DPFC at 150°C using a polytetrafluoroethylene membrane with its pores filled with zirconium phosphate (ZrP-PTFE) was similar to experimental results obtained with Nafion, aqueous H<sub>3</sub>PO<sub>4</sub>, and H<sub>2</sub>SO<sub>4</sub> doped polybenzimidazole electrolytes, when they were used in DPFCs. Because a ZrP-PTFE membrane operating at 150°C does not require water in the liquid phase, corrosion will be much less severe, and the use of non-precious metal catalysts may be possible. It was found that the thickness of the catalyst layer could be increased sufficiently so that the pressure drop between the reactant and product channels of interdigitated flow fields was small. By increasing the width of the lands and therefore the reactant's contact time with the catalyst it was possible to approach 100% propane conversion, thereby ensuring that there will be a minimum concentration of propane in the product stream from the fuel cell. Finally neglecting the diffusion term in the equation for the conservation of protons causes serious errors in computations of the electrical potential in the ZrP phase, the electron flux in the Pt/C phase, and the overpotential in both the anode and cathode catalyst layers.

#### 4.5. Acknowledgements

Financial assistance is gratefully acknowledged: A Discovery Grant was awarded from the Canadian federal government's Natural Sciences and Engineering Research Council. A project within the Ontario Fuel Cell Research and Innovation Network (OFCRIN) was funded both by the Ontario provincial government's Ontario Research Fund and by the Network's industrial sponsors. One of us (H.K.) is grateful to the Ontario government for the award of an Ontario Graduate Scholarship.

#### 4.6. Nomenclature

$A_{Pt}$ : platinum surface area per catalyst volume ( $m^2_{Pt} m^{-3}_{catalyst}$ )

$A_{CAT}$ : specific surface area of catalyst support(Vulcan carbon) in the anode and cathode  
( $m^2_{catalyst} g^{-1}_{catalyst}$ )

$c_G$ : total-concentration of the gas phase ( $mol m^{-3}$ )

$c_{i, ELY}$ : concentration of charged-species  $i$  in electrolyte ( $mol m^{-3}$ )

$D_i$ : diffusion coefficient of species  $i$  ( $cm^2 s^{-1}$ )

$D_p$ : effective particle diameter ( $\mu\text{m}$ )  
 $F$ : Faraday's constant, 96485 ( $\text{C mol}^{-1}_{\text{charge}}$ )  
 $f_{\text{Pt/CAT}}$ : fraction of catalyst support surface area covered by platinum ( $\text{m}^2_{\text{Pt}} \text{m}^{-2}_{\text{catalyst}}$ )  
 $\Delta G^\ddagger$ : activation energy for the exchange current density ( $\text{kJ mol}^{-1}$ )  
 $j$ : volumetric current density; rate of production of proton in electrode ( $\text{A m}^{-3}_{\text{catalyst}}$ )  
 $\mathbf{j}$ : current density, vector quantity ( $\text{A m}^{-2}_{\text{electrode face area}}$ )  
 $j_0$ : exchange current density at operating conditions ( $\text{A m}^{-2}_{\text{Pt}}$ )  
 $j_{0\text{-ref}}$ : reference exchange current density at the reference conditions ( $\text{A m}^{-2}_{\text{Pt}}$ )  
 $J$ : total current density ( $\text{mA cm}^{-2}$ )  
 $J_i$ : diffusion flux of species  $i$  ( $\text{mol m}^{-2} \text{s}^{-1}$ )  
 $L_w$ : land width in the flow field (mm)  
 $MW_i$ : molecular weight of species  $i$  ( $\text{g mol}^{-1}$ )  
 $n$ : normal direction  
 $\mathbf{N}_{i, \text{ELY}}$ : flux of species  $i$  in electrolyte, vector quantity ( $\text{mol cm}^{-2} \text{s}^{-1}$ )  
 $p$ : partial pressure of species  $i$  (Pa)  
 $P$ : total pressure (Pa)  
 $R$ : universal gas constant ( $\text{J mol}^{-1} \text{K}^{-1}$ )  
 $S_i$ : consumption rate of the reactant species  $i$  ( $\text{mol m}^{-3} \text{s}^{-1}$ )  
 $T$ : temperature (K)  
 $Th$ : thickness of catalyst layers and membrane ( $\mu\text{m}$ )  
 $t$ : time (s)  
 $\mathbf{u}$ : velocity of gas mixture, vector quantity (m/s)  
 $\mathbf{u}_{\text{ELY}}$ : velocity of electrolyte (m/s)  
 $u_i$ : mobility of species  $i$  ( $\text{cm}^2 \cdot \text{mol} / \text{J} \cdot \text{s}$ )  
 $u_n$ : velocity of gas mixture in normal direction ( $\text{m s}^{-1}$ )  
 $x$ : Cartesian coordinate  
 $y$ : Cartesian coordinate  
 $y_i$ : mole fraction of species  $i$  in the gas phase (-)  
 $z$ : moles of electron in anode and cathode reactions ( $\text{mol}_{\text{electrons}} \text{mol}^{-1}_{\text{propane}}$ )  
 $z_i$ : charge number of species  $i$  ( $\text{mol}_{\text{charge}} \text{mol}^{-1}_{\text{species}}$ )

**Greek letters:**

$\alpha_A$  and  $\alpha_C$ : anodic and cathodic charge transfer coefficients (-)

$\alpha_1$ ,  $\alpha_2$  and  $\alpha_3$ : relaxing parameters in boundary conditions

$\eta$ : overpotential (V)

$\varepsilon$ : volume fraction (-)

$\rho$ : mass density ( $\text{kg m}^{-3}$ )

$\rho_{\text{CAT}}$ : apparent bulk density of catalyst support ( $\text{g}_{\text{catalyst}} \text{m}^{-3}_{\text{catalyst}}$ )

$\rho_i$ : mass density of species  $i$  ( $\text{kg m}^{-3}$ )

$\mu_G$ : dynamic viscosity of gas mixture ( $\text{kg m}^{-1} \text{s}^{-1}$ )

$\nu_i$ : stoichiometric coefficient of species  $i$  (-)

$\sigma$ : ionic conductivity ( $\text{S m}^{-1}$ )

$\Phi$ : electrical potential (V)

$\Phi_{\text{Pt-EQ}}$ : equilibrium potential of conductor phase (V)

$\Phi_{\text{ELY-EQ}}$ : equilibrium potential of electrolyte phase (V)

$\Delta\Phi_{\text{CELL}}$ : cell potential difference (V)

$\Sigma(\nu_i)$ : sum of the atomic volumes for each of the  $i$  species ( $\text{m}^3 \text{kg}^{-1} \text{atom}^{-1}$ )

**Subscripts and superscripts:**

A: anode

av: phase-averaged quantity

C: cathode

C<sub>3</sub>: propane

C<sub>3</sub>O<sub>x</sub>: propane oxidation reaction on Pt catalyst

CO<sub>2</sub>: carbon dioxide

ELY: electrolyte phase in the anode or cathode catalyst layers

EQ: equilibrium state

G: gas mixture

H<sub>2</sub>O: water

$i$ : species in gas phase; propane, water, CO<sub>2</sub> and O<sub>2</sub>,

ML: membrane layer

n: normal direction

O<sub>2</sub>: oxygen

O<sub>2</sub>Rd: oxygen reduction reaction on platinum catalyst

Pt: platinum catalyst

ref: reference conditions

### **Abbreviations:**

ACL: anode catalyst layer

DPFC: direct propane fuel cell

FEM : finite element method

MEA: membrane electrode assembly

PAFC : phosphoric acid fuel cells

PEM: polymer electrolyte membrane or proton exchange membrane

PEMFC: polymer electrolyte membrane or proton exchange membrane fuel cell

PTFE: polytetrafluoroethylene

ZrP: zirconium phosphate

### **4.7. References**

[1] H.A. Liebhafsky, E.J. Cairns, The direct hydrocarbon fuel cell with aqueous electrolytes, In: Fuel Cells and Fuel Batteries, Wiley, New York, 1968, pp. 458-523.

[2] J.O. Bockris, S. Srinivasan, Fuel cells: their electrochemistry, In: Electrochemical Combustion of Organic Substances, McGraw-Hill, New York, 1969, pp. 357-411.

[3] E.J. Cairns, The anodic oxidation of hydrocarbons and the hydrocarbon fuel cell, Adv Electrochem and Electrochem Eng, 8 (1971) 337-391.

[4] Y. Si, R. Jiang, J. Lin, H.R. Kunz, J.M. Fenton, CO tolerance of carbon-supported platinum-ruthenium catalyst at elevated temperature and atmospheric pressure in a PEM fuel cell, J.Electrochem.Soc., 151 (2004) A1820-A1824.

- [5] W. Yan, S. Mei, C. Soong, Z. Liu, D. Song, Experimental study on the performance of PEM fuel cells with interdigitated flow channels, *J. Power Sources*, 160 (2006) 116-122.
- [6] W. Yan, C. Yang, C. Soong, F. Chen, S. Mei, Experimental studies on optimal operating conditions for different flow field designs of PEM fuel cells, *J. Power Sources*, 160 (2006) 284-292.
- [7] H. Khakdaman, Y. Bourgault, M. Ternan, Direct propane fuel cell anode with interdigitated flow fields: Two-dimensional model, *Ind Eng Chem Res*, 49 (2010) 1079-1085.
- [8] A. Faghri, Y. Zhang, *Transport Phenomena in Multiphase Systems*, Elsevier/Academic Press, Boston; 2006, p. 244.
- [9] W.T. Grubb, C.J. Michalske, A high performance propane fuel cell operating in the temperature range of 150-200°C, *J. Electrochem. Soc.*, 111 (1964) 1015-1019.
- [10] G. Psfogiannakis, Y. Bourgault, B.E. Conway, M. Ternan, Mathematical model for a direct propane phosphoric acid fuel cell, *J. Appl. Electrochem.*, 36 (2006) 115-130.
- [11] A.Z. Weber, J. Newman, Modeling transport in polymer-electrolyte fuel cells, *Chem. Rev.*, 104 (2004) 4679-4726.
- [12] A.Z. Weber, J. Newman, Transport in polymer-electrolyte membranes: II. Mathematical model, *J. Electrochem. Soc.*, 151 (2004).
- [13] J.J. Baschuk, X. Li, A comprehensive, consistent and systematic mathematical model of PEM fuel cells, *Appl. Energy*, 86 (2009) 181-193.
- [14] J.J. Baschuk, X. Li, Modeling of ion and water transport in the polymer electrolyte membrane of PEM fuel cells, *Int J Hydrogen Energy*, 35 (2010) 5095-5103.
- [15] P.C. Sui, S. Kumar, N. Djilali, Advanced computational tools for PEM fuel cell design. Part 1. Development and base case simulations, *J. Power Sources*, 180 (2008) 410-422.

- [16] T. Berning, D.M. Lu, N. Djilali, Three-dimensional computational analysis of transport phenomena in a PEM fuel cell, *J.Power Sources*, 106 (2002) 284-294.
- [17] Z.H. Wang, C.Y. Wang, K.S. Chen, Two-phase flow and transport in the air cathode of proton exchange membrane fuel cells, *J.Power Sources*, 94 (2001) 40-50.
- [18] J. Newman, K.E. Thomas-Alyea, *Electrochemical Systems*, 3rd ed., Wiley-Interscience, New Jersey, USA; 2004, pp. 672.
- [19] Hecht F, Pironneau O, LeHyaric A, Ohtsuka K. FreeFEM<sup>++</sup> Version 3.9. Available at: <http://www.freefem.org/ff++/>, 2010.
- [20] ParaView 3.8- Open Source Scientific Visualization. Available at: <http://www.paraview.org/>, 2010.
- [21] O. Savadogo, F.J. Rodriguez Varela, Low-temperature direct propane polymer electrolyte membranes fuel cell (DPFC), *J.New Mater.Electrochem.Syst.*, 4 (2001) 93-97.
- [22] D. Dobos, *Electrochemical Data : a handbook for electrochemists in industry and universities*, Elsevier, New York; 1975, pp. 339.
- [23] O.P. Panwar, A. Kumar, R. Amet, S.C. Amet, *Macedonian J. Chem Chem. Eng.* 27 (2008)133-139
- [24] A. Many, Y. Goldstein, N.B. Grover, *Semiconductor Surfaces*, North-Holland, Amsterdam, 1971, p.128.
- [25] M. Doyle, G. Rajendran, Perfluorinated Membranes, in *Handbook of Fuel Cells*, (eds. W. Vielstich, A. Lamm, H.A. Gasteiger) Wiley, England, 2003, vol. 3, p.373.

## CHAPTER 5

---

# MATHEMATICAL MODELING OF PROTON AND WATER TRANSPORT IN THE ELECTROLYTE PHASE OF DIRECT PROPANE FUEL CELLS<sup>1</sup>

H. Khakdaman, Y. Bourgault, M. Ternan

### ABSTRACT

A rigorous mathematical model for direct propane fuel cells (DPFCs) was developed using a computational fluid dynamics approach. The modeling results suggest that a specific combination of operating temperature and flow field design can overcome the main deficiency of DPFCs, high activation overpotential. Concentrated solution theory was applied by using the Generalized Maxwell-Stefan (GMS) equations in order to predict proton and water transport in the electrolyte phase of the anode and cathode catalyst layers and membrane layer. The GMS equations included both migration and diffusion phenomena for the proton and water transport in the electrolyte layer. It was shown that models accounting for proton migration only without diffusion have serious errors in their predictions of the electrical potential, proton concentration, water concentration and overpotential in the electrolyte phase. This finding can be generalized to all types of PEM fuel cells.

---

<sup>1</sup> This paper was submitted to the Journal of Power Sources

## 5.1. Introduction

The focus of this study is on the Direct Propane Fuel Cell (DPFC), which belongs to the Polymer Electrolyte Membrane Fuel Cell (PEMFC) family, but consumes propane instead of hydrogen as its feedstock. The generation of electrical energy in rural areas is our primary target application for DPFCs. The cost of delivering electrical energy to rural areas is substantially greater than to urban areas, because longer transmission lines are required to serve a comparatively small number of customers. Therefore more costly fuel cells can be justified for use in rural areas compared to urban areas. In addition, the infrastructure for delivering Liquefied Petroleum Gas (LPG) or propane to rural areas already exists. Two major advantages of DPFCs over hydrogen fuel cells are that the expense of hydrogen production plants and of hydrogen transport/storage will be eliminated from the fuel cell energy production cycle. However, a drawback associated with DPFCs is that the propane reaction rate is much slower than that of hydrogen. Liebhafsky and Cairns [1], Bockris and Srinivasan [2], and Cairns [3] reviewed the majority of the DPFC experimental research that had been done in the 1960's.

The approaches to the modeling of fuel cells are summarized below. Weber and Newman [4] have reviewed four groups of fuel cell models that consider transport of water and protons in the electrolyte phase: simple models, diffusive models, hydraulic models and combination models. The simple models [5-8] describe proton transfer using Ohm's law with a constant ionic conductivity. These models cannot predict phenomena such as membrane dehydration, in which water content and thus ionic conductivity are variables. For water movement, a numerical value of the net water flux has to be determined as the boundary condition at the interface between the catalyst layers and the membrane.

The diffusive models [9-14] predict the movement of dissolved water and protons within the membrane as a result of concentration and electrical potential gradients. They are applicable for the electrolyte systems with low water content ( $\lambda < 14$ , where  $\lambda$  is moles of water per mole of sulfonic acid sites in the Nafion membrane) where liquid water does not exist. The diffusive models are referred to as single phase models of membranes and can predict proton distribution in the electrolyte phase and membrane dehydration.

At high water contents, membrane pores are completely filled with liquid water, and the water content is assumed to be uniform everywhere. Therefore, water diffusion does not occur and the convection mechanism causes proton and water transport. The hydraulic models [15-18] were developed for membranes with high water content. Two phases, liquid water and membrane, are described by the hydraulic models. Water velocity is calculated by Schlögl's equation [18] which is a function of electrical potential gradient and pressure gradient. Finally, the hydraulic and diffusive models are merged in the combination models [19-21] when calculations covering the whole range of water content are desirable. This approach considers concentration and pressure gradients as driving forces for water and proton transport.

There are two possible approaches to deal with the transport properties in the diffusive models, i.e., dilute solution theory and concentrated solution theory [22]. Mass transport in dilute electrolyte systems is usually described by the Nernst-Planck equation [22] in which the flux of a charged species is a function of the concentration gradient of that species as well as the electrical potential gradient. For a non-charged species, the potential gradient term in the Nernst-Planck equation disappears. The membrane transport properties are not required to be constant in this approach.

Employing concentrated solution theory leads to rigorous models that consider the interactions between all species. Krishna [14] used Generalized Maxwell-Stefan (GMS) equations to implement this approach for multicomponent electrolyte systems in general. Wöhr et al. [12] also used Maxwell-Stefan (MS) equations to model proton and water transport in PEM fuel cells in which the MS diffusion coefficients are modified as a function of temperature and humidity. Fuller and Newman [23] used the electrochemical potential of each species as the driving force in the MS equations. Fimrite et al. [11] developed a transport model for water and protons based on the binary friction model. The mole fraction and potential gradients were considered in the electrochemical potential gradient expression. Baschuk and Li [10] also used MS equation and calculated the MS diffusion coefficients based on experimental data available in the literature. Then, they validated those coefficients with experimental data for the electro-osmotic drag coefficient.

A diffusive model has been developed in the present study to investigate the movement of water and protons in the electrolyte phase of a DPFC where the operation temperature is above the boiling point of water. One possible strategy for increasing the reaction rate in DPFC is to operate at temperatures of 150°C or higher. A membrane that can resist high temperature and show acceptable conductivity ( $5.0 \text{ S m}^{-1}$ ) has been developed in our research group [24]. This membrane is composed of porous polytetrafluoroethylene (PTFE) that contains zirconium phosphate ( $\text{Zr}(\text{HPO}_4)_2 \cdot \text{H}_2\text{O}$  or ZrP) in its pores. ZrP-PTFE is a known proton conductor [25]. Concentrated solution theory was used in which the binary interactions between water, protons and ZrP species were described.

We are developing mathematical models of DPFCs in order to understand the phenomena involved and hopefully make some improvements. The results reported here are major improvements over our previous model [5]. Like the vast majority of fuel cell models, our previous model only accounted for migration caused by an incorrect electrical potential gradient used to account for proton transport through the electrolyte layer. It neglected the influence of proton concentration on transport in the electrolyte phase. As we noted previously [5], that neglect caused serious errors. The overpotential gradient and the electrical potential gradient in the electrolyte phase were incorrect. This model, unlike the majority of fuel cell models, includes both a valid electrical potential gradient and a proton concentration gradient to account for proton transport by a combination of migration and diffusion. This model accounts for the influence of the proton concentration in the electrolyte phase and thereby overcomes the deficiencies mentioned above.

## **5.2. Model development**

This model solved the governing equations for the Membrane Electrode Assembly (MEA), consisting of the membrane layer, anode layer and cathode layer. A schematic of a typical DPFC is shown in Figure 5.1. The cell is composed of two bi-polar plates, two catalyst layers and a membrane layer. Each bipolar plate has two sets of channels: one for reactants and one for products. They are connected to each other through the catalyst layer. Figure 5.1 shows these channels for the anode bi-polar plate. The interdigitated flow fields show a symmetric geometry with repetitive pieces. In order to increase the computational speed, only one of these pieces was

considered as the modeling domain. Therefore, the modeling domain can be defined as the MEA that is located between the middle of a feed channel and the middle of its adjacent product channel. Figure 5.2 shows the modeling domain and boundaries.

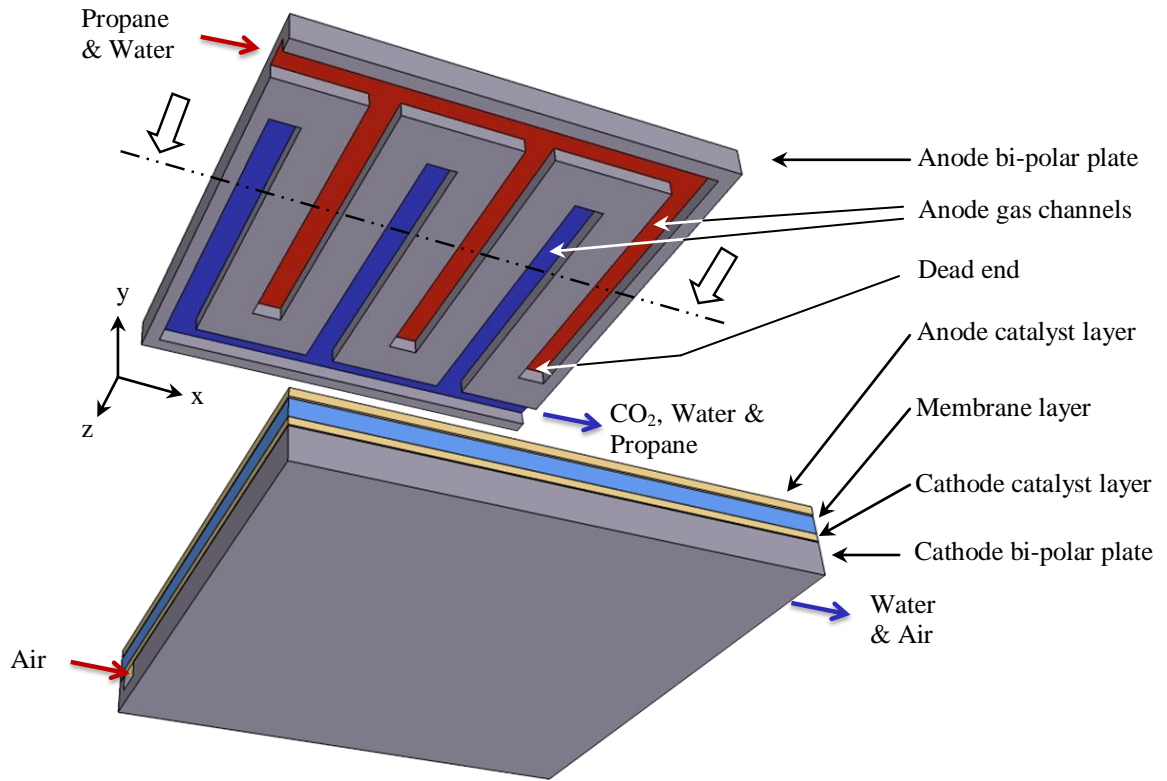


Figure 5.1. A 3-D schematic of a DPFC showing interdigitated flow-fields at the anode bi-polar plate.

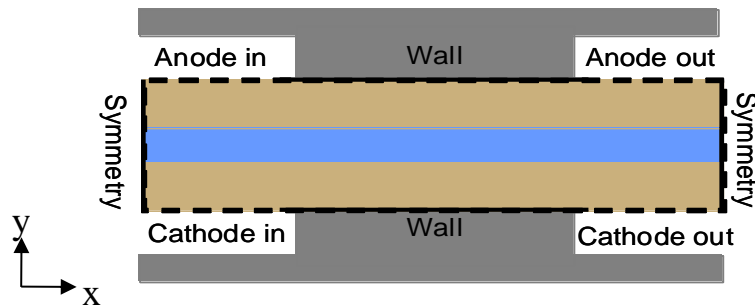


Figure 5.2. Boundaries in the modeling domain

Previously, it was shown that neglecting proton diffusion in the proton conservation equation led to incorrect results for the electrolyte potential and overpotential profiles even though the polarization curve was predicted correctly [5]. The present model includes both proton diffusion and migration.

### 5.2.1. Governing equations

Three phases are present in the anode and cathode catalyst layers. They are the "gas phase" containing reactants and products, the "solid catalyst phase" containing the carbon support and platinum, and the "solid electrolyte phase". The later consists of stationary ZrP matrix ( $\text{Zr}(\text{HPO}_4)_2 \cdot \text{H}_2\text{O}$ ) containing mobile  $\text{H}_2\text{O}$  ( $\text{Zr}(\text{HPO}_4)_2 \cdot 2\text{H}_2\text{O}$ ) and  $\text{H}^+$  ( $\text{Zr}(\text{HPO}_4)_2 \cdot \text{H}_3\text{O}^+$ ) species that can be transferred. The membrane layer contains the electrolyte phase as well as PTFE.

Conservation equations for momentum, total mass, and mass of non-charged species were solved for the gas phase in each of the catalyst layers. A list of equations that were used for the gas phase of both anode and cathode catalyst layers is shown in Table 5.1. Eq. (5-17) describes the total mass conservation in the gas phase of the catalyst layers. The second term in this equation is the sink or source term describing the mass consumption or production in the gas phase caused by electrochemical reactions. Eq. (5-18), is the linear form of the Ergun equation. It was used to calculate the pressure profiles in the gas phase of the catalyst layers because they are packed beds. At the conditions used in this study, the magnitude of the quadratic velocity term in the Ergun equation was much smaller than the linear term. Hence only the linear term in velocity was used in Eq. (5-18). Eqs. (5-17) and (5-18) were solved together to calculate the velocity and pressure profiles in the gas phase of the catalyst layers. Mass balances for each of the individual gas phase species account for convection, diffusion, and reaction, as shown in Eq. (5-19).

Eqs. (5-20) and (5-21) describe, respectively, water and proton conservation in the electrolyte phase of the membrane and catalyst layers. Diffusion was described by concentrated solution theory through the use of the GMS equations. The following paragraphs illustrate the derivation of Eqs. (5-20) and (5-21).

A general procedure for the calculation of mass fluxes in multicomponent electrolyte systems was presented by Krishna [14]. It has been proven that the Nernst-Planck equation is a limiting case of the GMS equations. The GMS equations can be written as follows:

$$\vec{d}_i = \sum_{\substack{j=1 \\ j \neq i}}^n \frac{x_i \vec{J}_j - x_j \vec{J}_i}{c_{ELY} \mathcal{D}_{ij}} \quad i = 1, 2, \dots, n - 1 \quad (5 - 1)$$

where  $\vec{d}_i$  is a generalized driving force for mass transport of species  $i$ . Because the summation of the  $n$  driving forces is equal to zero due to the Gibbs-Duhem limitation [26], only  $n-1$  driving forces are independent. The equation to calculate the generalized driving force has been derived based on non-equilibrium thermodynamics [26]. A simplified expression for a solid stationary electrolyte (no convection term) [14] can be written as:

$$\vec{d}_i = \nabla x_i + x_i z_i \frac{F}{RT} \nabla \phi_{ELY} \quad (5 - 2)$$

For a non-charged species such as water  $z_i$  is equal to zero, and according to Eq. (5-2), the concentration gradient will be the only driving force.

The migration term in Eq. (5-2) was obtained by representing ion mobility by the Nernst-Einstein relation ( $\mathcal{D}_i = RTu_i$ ). This equation is applicable only at infinite dilution. However, it can be used in concentrated solutions if additional composition-dependent transport parameters, such as the  $B'$  parameters in Eq. (5-12), are used to calculate the flux of ions [22]. It will be shown in the following paragraphs that Eqs. (5-8) to (5-11) represent the composition-dependent parameters.

Eq. (5-1) results in  $(n-1)$  independent equations that can be written in matrix form for convenience:

$$c_{ELY} \begin{pmatrix} \vec{d}_1 \\ \vdots \\ \vec{d}_{n-1} \end{pmatrix} = - \begin{pmatrix} B_{11} & \cdots & B_{1,n-1} \\ \vdots & \ddots & \vdots \\ B_{n-1,1} & \cdots & B_{n-1,n-1} \end{pmatrix} \begin{pmatrix} \vec{J}_1 \\ \vdots \\ \vec{J}_{n-1} \end{pmatrix} \quad (5-3)$$

where the elements of the matrix of inverted diffusion coefficients [B] are given by

$$B_{ii} = \sum_{\substack{j=1 \\ j \neq i}}^n \frac{x_j}{D_{ij}} \quad i = 1, 2, \dots, n-1 \quad (5-4)$$

$$B_{ij} = \frac{-x_j}{D_{ij}} \quad i = 1, 2, \dots, n-1; (i \neq j) \quad (5-5)$$

The fluxes of species,  $\vec{J}_i$ , can be calculated from Eq. (5-6) which is the inversion of Eq. (5-3).

$$\begin{pmatrix} \vec{J}_1 \\ \vdots \\ \vec{J}_{n-1} \end{pmatrix} = -c_{ELY} \begin{pmatrix} B_{11} & \cdots & B_{1,n-1} \\ \vdots & \ddots & \vdots \\ B_{n-1,1} & \cdots & B_{n-1,n-1} \end{pmatrix}^{-1} \begin{pmatrix} \vec{d}_1 \\ \vdots \\ \vec{d}_{n-1} \end{pmatrix} \quad (5-6)$$

For the present electrolyte system containing three species, mobile H<sub>2</sub>O and H<sup>+</sup> plus immobile solid ZrP, Eq. (5-6) may be written as

$$\begin{pmatrix} \vec{J}_{H_2O} \\ \vec{J}_{H^+} \end{pmatrix} = -c_{ELY} \begin{pmatrix} B'_{H_2O-H_2O} & B'_{H_2O-H^+} \\ B'_{H^+-H_2O} & B'_{H^+-H^+} \end{pmatrix} \begin{pmatrix} \vec{d}_{H_2O} \\ \vec{d}_{H^+} \end{pmatrix} \quad (5-7)$$

where [B'] is the inverse of the matrix of inverted diffusion coefficients. Because  $D_{H_2O-H^+} = D_{H^+-H_2O}$ , the elements of [B'] are calculated using Eqs. (5-8) to (5-11) which are functions of the GMS diffusivities and the species mole fractions in the electrolyte phase.

$$B'_{H_2O-H_2O} = \frac{x_{H_2O} \mathfrak{D}_{H^+-ZrP} + \mathfrak{D}_{H_2O-H^+}}{x_{H^+} + \frac{\mathfrak{D}_{H^+-ZrP}}{\mathfrak{D}_{H_2O-ZrP}} x_{H_2O} + \frac{\mathfrak{D}_{H_2O-H^+}}{\mathfrak{D}_{H_2O-ZrP}}} \quad (5-8)$$

$$B'_{H_2O-H^+} = \frac{x_{H_2O} \mathfrak{D}_{H^+-ZrP}}{x_{H^+} + \frac{\mathfrak{D}_{H^+-ZrP}}{\mathfrak{D}_{H_2O-ZrP}} x_{H_2O} + \frac{\mathfrak{D}_{H_2O-H^+}}{\mathfrak{D}_{H_2O-ZrP}}} \quad (5-9)$$

$$B'_{H^+-H_2O} = \frac{x_{H^+} \mathfrak{D}_{H_2O-ZrP}}{x_{H_2O} + \frac{\mathfrak{D}_{H_2O-ZrP}}{\mathfrak{D}_{H^+-ZrP}} x_{H^+} + \frac{\mathfrak{D}_{H_2O-H^+}}{\mathfrak{D}_{H^+-ZrP}}} \quad (5-10)$$

$$B'_{H^+-H^+} = \frac{x_{H^+} \mathfrak{D}_{H_2O-ZrP} + \mathfrak{D}_{H_2O-H^+}}{x_{H_2O} + \frac{\mathfrak{D}_{H_2O-ZrP}}{\mathfrak{D}_{H^+-ZrP}} x_{H^+} + \frac{\mathfrak{D}_{H_2O-H^+}}{\mathfrak{D}_{H^+-ZrP}}} \quad (5-11)$$

Combining sets of Eqs. (5-7) and (5-2) results in two independent equations that can be used to calculate the fluxes of mobile species ( $\vec{J}_{H_2O}$  and  $\vec{J}_{H^+}$ ) within the electrolyte phase:

$$\vec{J}_{H_2O} = -c_{ELY} B'_{H_2O-H_2O} (\nabla x_{H_2O}) - c_{ELY} B'_{H_2O-H^+} \left( \nabla x_{H^+} + \frac{F x_{H^+}}{RT} \nabla \phi_{ELY} \right) \quad (5-12)$$

$$\vec{J}_{H^+} = -c_{ELY} B'_{H^+-H_2O} (\nabla x_{H_2O}) - c_{ELY} B'_{H^+-H^+} \left( \nabla x_{H^+} + \frac{F x_{H^+}}{RT} \nabla \phi_{ELY} \right) \quad (5-13)$$

Eqs. (5-12) and (5-13) show that diffusion flux of each species is a function of the concentration gradient of all species as well as of the potential gradient. There are five unknowns in Eqs. (5-12) and (5-13),  $\vec{J}_{H_2O}$ ,  $\vec{J}_{H^+}$ ,  $x_{H_2O}$ ,  $x_{H^+}$  and  $\phi_{ELY}$ . Therefore, three more equations are required.

ZrP is immobile. As a result the diffusion phenomenon will effectively be the interchange of  $H^+$  and  $H_2O$  species. Therefore, for diffusion purposes we will only consider the domain of the mobile species,  $H^+$  and  $H_2O$ , and will ignore the immobile species, ZrP. On that basis Eq. (5-14) can be used as a third equation. Nevertheless, the presence of ZrP is important because of its interaction with the mobile species. Specifically, the values of the  $B'$  coefficients for  $H^+$  and  $H_2O$  were influenced by the presence of ZrP.

$$x_{H_2O} + x_{H^+} = 1.0 \quad (5 - 14)$$

The differential equations for  $H_2O$  and  $H^+$  mass conservation in the electrolyte phase can be expressed in molar units as:

$$\nabla \cdot \vec{J}_{H_2O} = \frac{-j}{zF} \quad (5 - 15)$$

$$\nabla \cdot \vec{J}_{H^+} = \frac{j}{zF} \quad (5 - 16)$$

where  $j$  is the volumetric current production. This quantity which appears in Eqs. (5-15) to (5-17) and (5-19) to (5-21) is the rate of production of protons in the anode. Therefore, it is positive in the anode,  $j_A$ , and negative in the cathode,  $j_C$ . It was calculated using the Butler-Volmer equation for the anode and cathode, Eqs. (5-22) and (5-25), respectively. Exchange current densities at the anode and cathode are a function of the reactants' partial pressure and the operating temperature as shown in Eqs. (5-23) and (5-26). The Butler-Volmer equation and its parameters for both propane oxidation and oxygen reduction were described in our previous communication [5]. Eqs. (5-12) to (5-16) were combined and are shown as Eqs. (5-20) and (5-21) in Table 5.1.

Table 5.1. List of equations

Equations	Eq. No.
<b>Conservation of mass in gas phase:</b>	
$\nabla \cdot (\varepsilon_G \rho_G \vec{\mathbf{u}}) + \sum_i^n \frac{\nu_i MW_i j}{zF} = 0$	(5-17)
$i = \text{C}_3\text{H}_8, \text{H}_2\text{O}$ and $\text{CO}_2$ for the anode; $\text{O}_2$ and $\text{H}_2\text{O}$ for the cathode	
<b>Conservation of momentum in gas phase:</b>	
$-\nabla P = 150 \left[ \frac{\mu_G (1 - \varepsilon_G)^2}{D_p^2 \varepsilon_G^3} \right] \vec{\mathbf{u}}$	(5-18)
<b>Conservation of non-charged species in gas phase:</b>	
$\nabla \cdot (\varepsilon_G c_G \vec{\mathbf{u}} y_i) - \nabla \cdot (\varepsilon_G c_G D_i \nabla y_i) + \frac{\nu_i j}{zF} = 0$	(5-19)
$i = \text{C}_3\text{H}_8$ and $\text{CO}_2$ for the anode; $\text{O}_2$ and $\text{H}_2\text{O}$ for the cathode	
<b>Conservation of species in the electrolyte phase:</b>	
<b>For water:</b>	
$-\nabla \cdot (c_{ELY} (B'_{\text{H}_2\text{O}-\text{H}_2\text{O}} - B'_{\text{H}_2\text{O}-\text{H}^+}) \nabla x_{\text{H}^+}) + \nabla \cdot (c_{ELY} B'_{\text{H}_2\text{O}-\text{H}^+} \frac{F x_{\text{H}^+}}{RT} \nabla \phi_{ELY}) - \frac{j}{zF} = 0$	(5-20)
<b>For proton:</b>	
$\nabla \cdot (c_{ELY} (B'_{\text{H}^+-\text{H}^+} - B'_{\text{H}^+-\text{H}_2\text{O}}) \nabla x_{\text{H}^+}) + \nabla \cdot (c_{ELY} B'_{\text{H}^+-\text{H}^+} \frac{F x_{\text{H}^+}}{RT} \nabla \phi_{ELY}) + \frac{j}{zF} = 0$	(5-21)
<b>Butler-Volmer equation in the anode:</b>	
$j_A = j_A^0 A_{Pt} \left[ \exp\left(\frac{\alpha_A F \eta_A}{RT}\right) - \exp\left(\frac{-\alpha_C F \eta_A}{RT}\right) \right]$	(5-22)
$\text{where, } j_A^0 = j_{\text{C}_3\text{Ox}}^{0.ref} \left( \frac{p_{\text{C}_3}}{p_{\text{C}_3}^{ref}} \right) \exp \left[ \frac{\Delta G_{\text{C}_3\text{Ox}}^\ddagger}{R} \left( \frac{1}{T^{ref}} - \frac{1}{T} \right) \right]$	(5-23)
$\text{and } \eta_A = \Delta \phi_A - \Delta \phi_A^{EQ} = (\phi_{Pt_A} - \phi_{ELY_A}) - (\phi_{Pt_A}^{EQ} - \phi_{ELY}^{EQ})$	(5-24)
<b>Butler-Volmer equation in the cathode:</b>	
$j_C = j_C^0 A_{Pt} \left[ \exp\left(\frac{\alpha_A F \eta_C}{RT}\right) - \exp\left(\frac{-\alpha_C F \eta_C}{RT}\right) \right]$	(5-25)
$\text{where, } j_C^0 = j_{\text{O}_2\text{Rd}}^{0.ref} \left( \frac{p_{\text{O}_2}}{p_{\text{O}_2}^{ref}} \right) \exp \left[ \frac{\Delta G_{\text{O}_2\text{Rd}}^\ddagger}{R} \left( \frac{1}{T^{ref}} - \frac{1}{T} \right) \right]$	(5-26)
$\text{and } \eta_C = \Delta \phi_C - \Delta \phi_C^{EQ} = (\phi_{Pt_C} - \phi_{ELY_C}) - (\phi_{Pt_C}^{EQ} - \phi_{ELY}^{EQ})$	(5-27)

### 5.2.2. Numerical procedure

The numerical solution procedure is illustrated in Figure 5.3. The equations in Table 5.1 define the problem at steady state. However, a time-derivative was appended to each partial differential equation and a backward Euler time stepping method was used to increase stability while converging to the steady state solution. The Finite Element Method was used to discretize the partial differential equations in space, with all dependant variables discretized by a linear finite element except for the pressure that is taken as a quadratic.

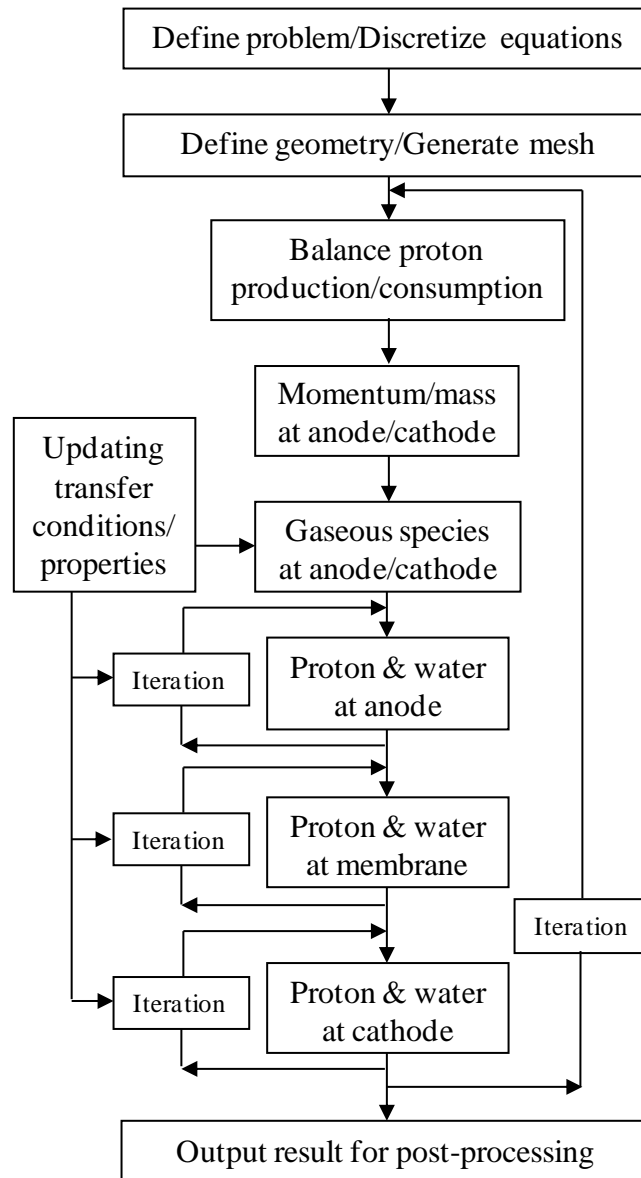


Figure 5.3. Modeling procedure

FreeFEM<sup>++</sup> software has been successfully used to solve the two-dimensional partial differential equations in Table 5.1. It is open-source software and is based on the Finite Element Method developed by Hecht et al. [27]. The calculated results from FreeFEM<sup>++</sup> were exported to ParaView visualization software [28] for post-processing. ParaView is also open-source software.

There is no proton loss through the exterior boundaries of the domain (Figure 5.2). Therefore, the total rate of proton production in the anode,  $\int_{\text{Anode}} j \, dV$ , has to be equal to the total rate of proton consumption in the cathode,  $\int_{\text{cathode}} (-j) \, dV$ . In each case, the electrical potential of the catalyst phase of the anode,  $\phi_{\text{Pt}_A}$ , and that of the cathode,  $\phi_{\text{Pt}_C}$ , had individual constant values. Then all the variables in the whole domain were calculated. However, having fixed electrical potentials of the anode and cathode catalyst phases does not guarantee that the proton production at the anode will equal the proton consumption at the cathode. The difference between the rate of proton production and consumption can be minimized by shifting  $\phi_{\text{ELY}}$  by a constant value because the production and consumption rates are functions of the electrical potential in both of their respective catalyst phases,  $\phi_{\text{Pt}_A}$  and  $\phi_{\text{Pt}_C}$ , and in the electrolyte phase,  $\phi_{\text{ELY}}$ . Therefore, the Newton method was used to force equal proton production and consumption. In other words, balancing  $\int_{\text{Anode}} j \, dV$  and  $\int_{\text{cathode}} (-j) \, dV$  acts as a constraint for the conservation of protons in the electrolyte phase.

The equations for the conservation of momentum, total mass and individual species in the gas phase of the anode and cathode were solved by assuming there was no species crossover through the membrane. Electrical potential, proton and water concentrations in the electrolyte phase of the anode, cathode and membrane layers were coupled to each other. These variables were calculated by solving Eq. (5-20), (5-21) and (5-14) iteratively in each layer. Then, the Robin method [5] was used to couple the solutions between layers. In the Robin method, both of the following transfer conditions are progressively satisfied on the anode catalyst/membrane interface and the membrane/cathode catalyst interface through iterations: (a) the continuity of the variable (e.g. potential) and (b) the continuity of the flux (e.g. electrical current).

Figure 5.2 shows four types of boundary conditions for the modeling domain, i.e., inlet, outlet, wall of the land, and the mid-channel symmetry boundaries. The flux of species in the gas phase is zero in the normal direction of the walls because there is no transfer through walls. The zero flux condition is also true at the mid-channel symmetry boundaries. The compositions of the gaseous species are known at the inlet of the anode and cathode catalyst layers. It was assumed that no change in the composition of gas mixture occurred after leaving the catalyst bed. Therefore, the composition gradients are zero in the direction normal to the catalyst layer at the outlet boundaries. The zero flux condition is applied at all exterior boundaries for the species in the electrolyte phase.

### 5.2.3. Input parameters

The parameters used for the simulations are shown in Table 5.2. The GMS diffusivities,  $\mathfrak{D}_{ij}$ , which are used in Eqs. (5-8) to (5-11) have to be calculated from the Fickian diffusion coefficients,  $D_{ij}$ . For ideal solutions, the Fickian diffusion,  $D_{ij}$ , can be used as  $\mathfrak{D}_{ij}$  in the GMS equations [26] because the concentration dependence of Fickian diffusion coefficients is ignored. Experimental values for  $D_{\text{H}^+-\text{ZrP}}$  and  $D_{\text{H}_2\text{O}-\text{H}^+}$  are given in Table 5.2. No experimental data were available for the diffusivity of water in ZrP. Therefore, it was set equal to the known value for the diffusivity of protons in ZrP [29]. This assumption is consistent with one water molecule being dragged by each proton that travels from anode to cathode. These were the three diffusivities used to calculate the  $B'$  parameters in Eqs. (5-8) to (5-11).

**Table 5.2. Operational, electrochemical and design parameters for simulations**

<b>Property</b>	<b>Value</b>
Temperature, T	423 – 503K
Pressure, P	101.3 k Pa
Proton–ZrP diffusivity, $D_{H^+-ZrP}$	$3.1 \times 10^{-12} \text{ m}^2 \text{ s}^{-1}$ [29]
Proton–water diffusivity, $D_{H_2O-H^+}$	$2.9 \times 10^{-10} \text{ m}^2 \text{ s}^{-1}$ [12]
Ionic conductivity in membrane, $\sigma_{ZrP/PTFE}$	$5.0 \text{ S m}^{-1}$ [24]
Electrical resistivity in membrane, $R_{PTFE}$	$1.0 \times 10^{16} \text{ } \Omega \text{ m}$
Charge transfer coefficients, $\alpha_A$ and $\alpha_C$	1.0 [30]
Equilibrium potential of catalyst phase at the anode, $\Phi_{Pt\_A}^{EQ}$	0.136 V [1]
Equilibrium potential of catalyst phase at the cathode, $\Phi_{Pt\_C}^{EQ}$	1.229 V
Equilibrium potential of electrolyte phase, $\Phi_{ELY}^{EQ}$	0.136 V
Apparent bulk density of carbon catalyst support, $\rho_{CAT}$	$0.259 \text{ g}_{\text{catalyst}} \text{ mL}^{-1}_{\text{catalyst}}$
Specific surface area of carbon catalyst support in the anode and cathode, $A_{CAT}$	$255 \text{ m}^2_{\text{catalyst}} \text{ g}^{-1}_{\text{catalyst}}$
Gas phase volume fraction in anode and cathode, $\varepsilon_G$	0.5
Electrolyte phase volume fraction in anode and cathode, $\varepsilon_{ELY}$	0.4
Effective particle diameter in anode and cathode, $D_p$	5 $\mu\text{m}$
Land width, $L_w$	2 – 8 mm
Anode and cathode thickness, $Th_A, Th_C$	200 – 400 $\mu\text{m}$
Membrane thickness, $Th_M$	100 – 200 $\mu\text{m}$
Fluid channels width in bi-polar plates	0.4 mm

#### 5.2.4. Model Validation

The model predicts the performance of a DPFC that has (i) interdigitated flow fields, (ii) zirconium phosphate as the electrolyte, and (iii) operates over a temperature range of 150-230°C. As there are no experimental data for DPFCs having zirconium phosphate electrolytes and interdigitated flow fields, the model results have been compared to published results for DPFCs with other types of electrolytes and flow fields.

Figure 5.4 compares the modeling results for zirconium phosphate electrolyte with the experimental data for other types of electrolytes [31, 32]. Figure 5.4 shows that the polarization curve for ZrP-PTFE electrolyte is somewhat comparable to that for the other electrolytes. The difference between the polarization curves can be partially explained by the difference between conductivities of the electrolytes. The proton conductivity of a non-modified Nafion 117 approaches  $10 \text{ Sm}^{-1}$  at 80°C [33]. The conductivity of the 95%  $\text{H}_3\text{PO}_4$  electrolyte is  $35 \text{ Sm}^{-1}$  at 200°C [34]. However, the proton conductivity for the best ZrP-PTFE that has been developed in our laboratory is about  $5 \text{ Sm}^{-1}$  at 150°C.

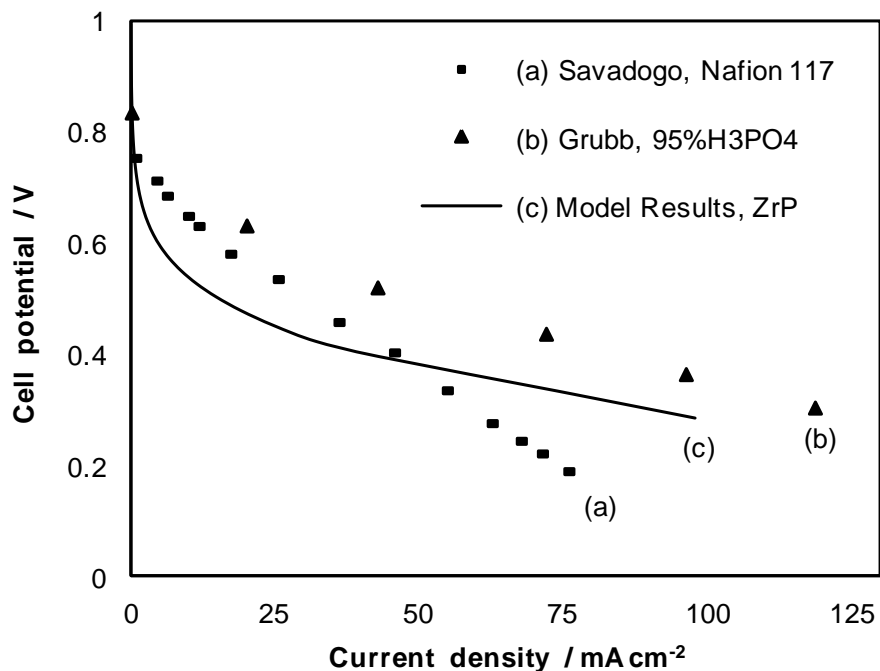


Figure 5.4. Polarization curves of direct propane/oxygen fuel cell using Pt anode and cathode; (a) experimental results [31] using Nafion 117 at 95°C; (b) experimental results [32] using 95%  $\text{H}_3\text{PO}_4$  at 200°C; (c) the present proton migration and diffusion model results for a solid ZrP-PTFE electrolyte at 150°C.

### 5.3. Results and discussion

Figure 5.5a shows the two-dimensional variation of the proton concentration in the electrolyte phase of the entire domain, that is the anode catalyst layer, the membrane layer, and the cathode catalyst layer. The proton concentration at the anode inlet close to the feed gas channel has the highest value. This would be expected because the propane's partial pressure is higher at the anode inlet and that causes a higher propane oxidation reaction rate, according to the Butler-Volmer equation, Eq. (5-22). Because protons are produced in the anode catalyst layer and consumed in the cathode catalyst layer, the proton concentration must be higher at the anode than the cathode. This proton concentration gradient provides a driving force for protons to diffuse from the anode to the cathode.

The electrical potential variation in the electrolyte phase of the catalyst layers and membrane is shown in Figure 5.5b. As the reaction rate in the catalyst layers is not uniform, current density and electrical potential will be variable. Figure 5.5b shows that the electrical potential is higher at the cathode electrolyte phase than at the anode electrolyte phase. That electrical potential gradient provides a driving force for protons to migrate from the cathode to the anode. This proton migration (caused by the electrical potential gradient) is in the opposite direction to the proton diffusion (caused by the proton concentration gradient) that was discussed above.

Figure 5.5c shows the magnitude and direction of protonic flux in the electrolyte phase of the anode, cathode and membrane layers. Protons are produced in the anode, travel from the anode, through the membrane layer, and to cathode, where they are consumed. As discussed above, in Figure 5.5a, the concentration driving force for proton flux was from the anode to the cathode and in Figure 5.5b the electrical potential driving force was in the opposite direction, from the cathode to the anode. Finally, Figure 5.5c demonstrates that the net flux of protons is from the anode toward the cathode. As the net flux is the summation of two driving forces that are in opposite directions, one can conclude that proton diffusion is dominant over proton migration. For the fuel cell to operate, the net transport of protons must be from the anode to the cathode. Therefore, the rate of proton diffusion must exceed the rate of proton migration. Figure 5.5c also shows that the arrows' length are becoming longer (indicating that the proton flux increases) in the y-direction from the anode land/anode catalyst interface to the anode catalyst/membrane

interface as more protons are produced throughout the anode catalyst layer. Similarly, the arrows' length becomes shorter (as the proton flux decreases) in the y-direction from membrane/cathode catalyst interface to the cathode catalyst/cathode land interface.

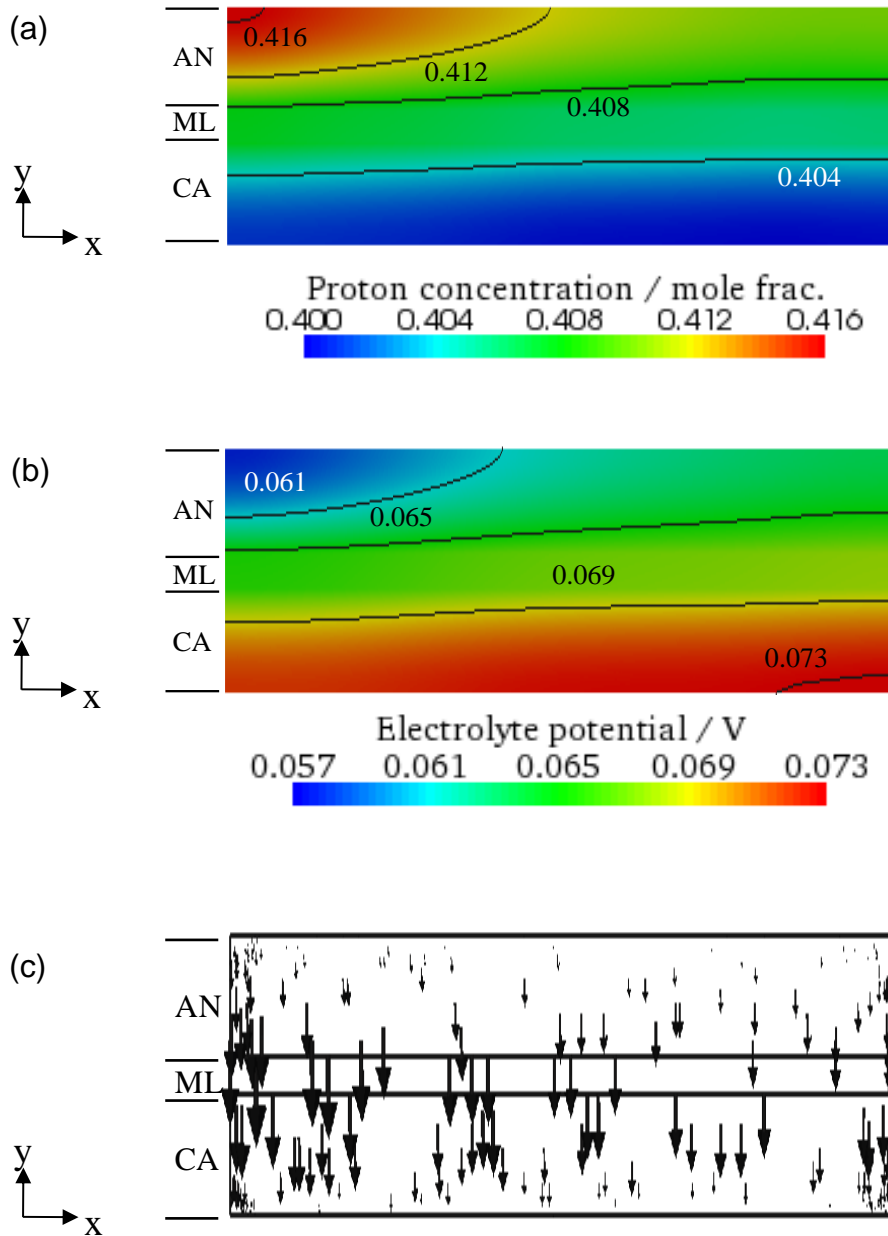
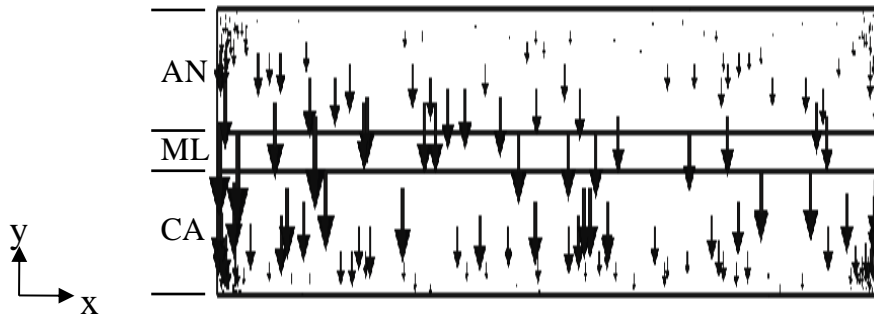


Figure 5.5. (a) Proton concentration in the electrolyte phase of the anode, membrane and cathode layers; (b) Electrical potential profile for the electrolyte phase of the anode, membrane and cathode layers; (c) Protonic flux from the anode to the cathode in the electrolyte phase (The vectors length indicate the flux magnitude which varies from 0 to 17 mA cm<sup>-2</sup> in this case).

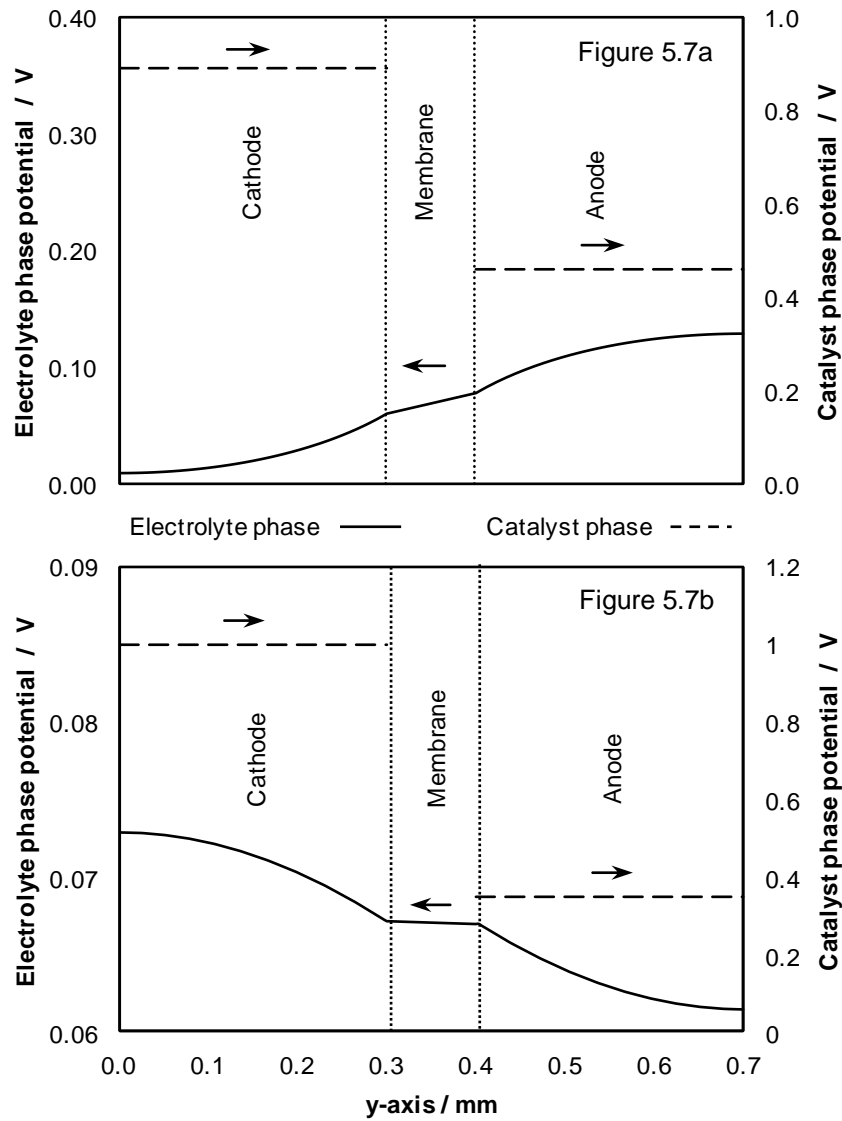
Electrons flow from anode to cathode of fuel cells, both through the external circuit and through the electrolyte. The electron flow rate will be many orders of magnitude smaller through the electrolyte than through the external circuit. The electron flux (current) through the electrolyte as shown in Figure 5.6 is generally similar to the proton flux in Figure 5.5c. Although the vast majority of electrons flow through the external circuit, the production and consumption of the miniscule number of electrons that flow through the electrolyte have a distribution (Figure 5.6) that is similar to the distribution of protons (Figure 5.5c).



**Figure 5.6. Electronic flux from the anode to the cathode in the electrolyte phase. The vectors length indicate the flux magnitude which varies from 0 to  $1 \times 10^{-11} \text{ mA cm}^{-2}$  in the same case as Figure 5.5c.**

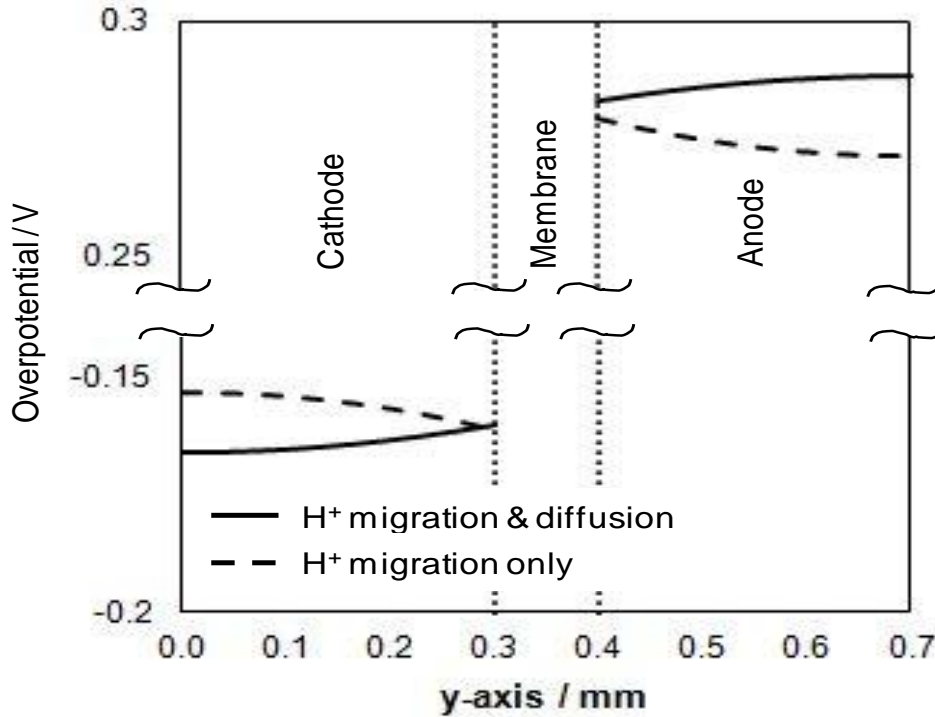
It is constructive to compare this model (migration and diffusion) with our previous model (migration only). A cross-section of Figure 5.5b along the y-direction at the middle of the domain ( $x=L_w/2$ ) is shown in Figure 5.7b, where the electrical potential in the electrolyte phase (the left axis in Figure 5.7b- solid line) is compared with that in the two solid catalyst phases (the right axis in Figure 5.7b- dashed lines). The electrical potentials in the two solid catalyst phases are almost constant because of the high electrical conductivity of these phases. Because the electrical potential in the catalyst phase at the anode is less than that at the cathode, negatively charged electrons are forced to flow from the anode to the cathode through the external circuit. Similarly, the electrical potential in the electrolyte phase of the anode will be less than that at the cathode so that there will be a miniscule flow rate of negatively charged electrons through the electrolyte phase from the anode to the cathode. This reasoning is in agreement with the results of migration and diffusion model that are shown in Figure 5.7b. In contrast, the results from the migration only model are erroneous, as shown in Figure 5.7a from our previous work [5]. Figure

5.7b shows that the electrical potential difference drives negatively charged electrons from the anode to the cathode while driving the positively charged protons from the cathode to the anode. In the migration only model the electrical potential difference driving force for proton transfer would have caused protons to travel from the cathode to the anode which is the wrong direction.



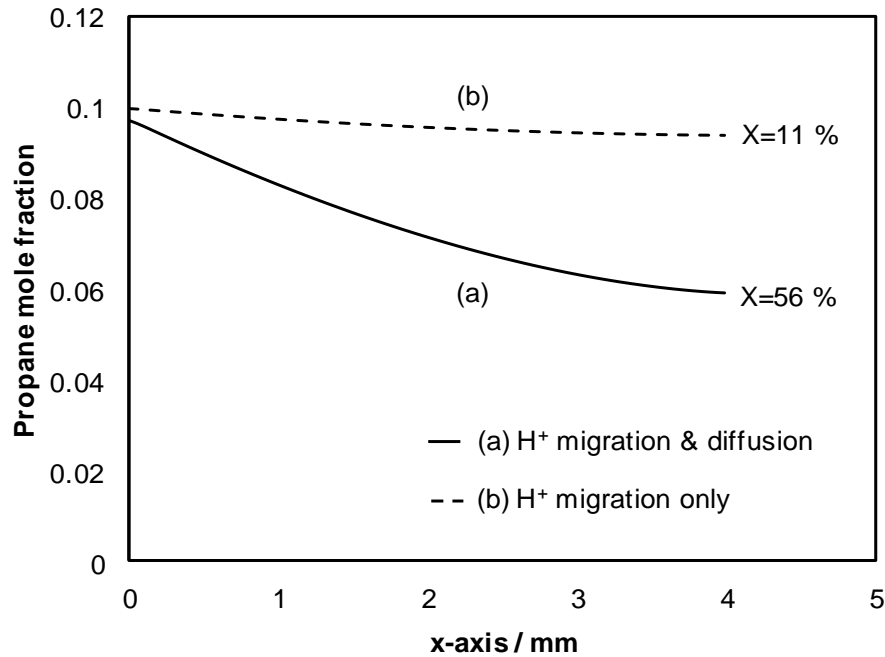
**Figure 5.7. Electrical potential profiles in the y-direction for the electrolyte and catalyst phases located at the middle of the domain x-direction for the cathode and anode catalyst layers and membrane layer. The arrows point in the direction of the ordinate scale that applies to each of the three curves; (a) Proton migration only within the electrolyte phase [5]; (b) Proton migration and diffusion within the electrolyte phase [the present model].**

Figure 5.8 compares the anodic and cathodic overpotential for two cases. The solid lines are the results from this model (migration and diffusion). The dashed lines are the results from our previous model (migration only) and they indicate the opposite trend with respect to the solid lines. Since the overpotential is the electrical driving force (see Eqs. (5-22) and (5-24)), it will always have its largest value adjacent to the land and decreases toward the membrane. This migration plus diffusion model predicts the correct behaviour, but the previous migration only model predicts an invalid result. Moreover, reaction rates in the anode and cathode are functions of overpotential. Therefore, an incorrect species distribution within the gas phase of the catalyst layers would have been predicted if proton diffusion had been ignored in the electrolyte phase. In other words, the migration only model can neither correctly calculate the species concentration in the electrolyte phase nor in the gas phase.



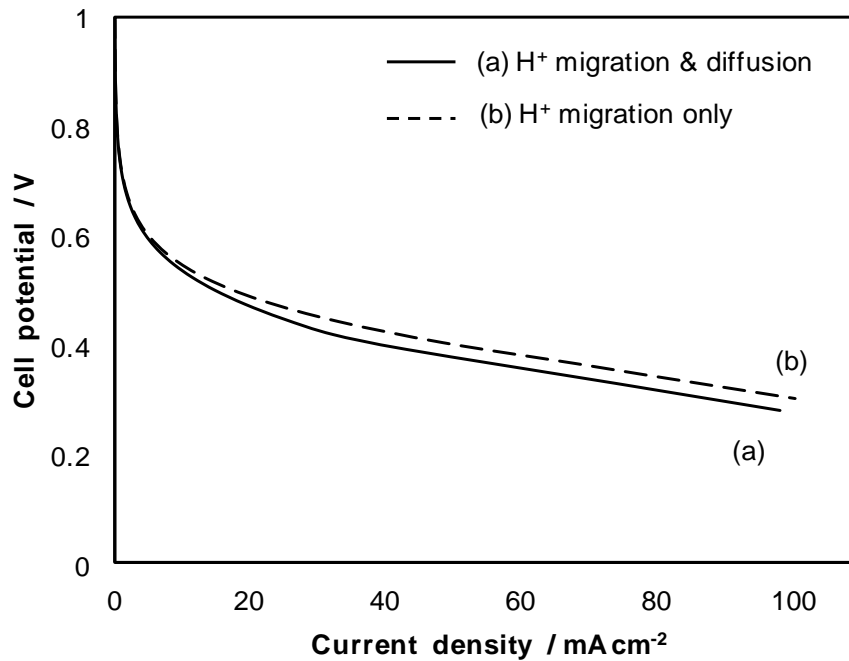
**Figure 5.8. Overpotential profile in the anode and cathode along y-axis at the middle of the modeling domain. Solid lines: migration and diffusion; Dashed lines: migration only [5].**

Figure 5.9 shows the propane mole fraction in the gas phase of the anode catalyst layer along the x-direction. For the similar operating conditions, the present model (migration and diffusion) predicts more propane conversion ( $X=56\%$ ) than the previous model does ( $X=11\%$ ). This difference is caused by the different overpotential profiles predicted by the two models. The difference in overpotentials, for migration and diffusion compared to migration only is shown in Figure 5.8. Because those differences are small there is relatively little difference between the two polarization curves shown in Figure 5.10. However for reaction, those small differences are in exponential terms, as shown in Eqs. (5-22) and (5-25). It is the exponential terms that cause the large differences in conversion shown in Figure 5.9.



**Figure 5.9. Propane mole fraction in the gas phase of the anode catalyst layer along the x-direction at the middle of the anode catalyst layer (a) Proton migration and diffusion within the electrolyte phase [the present model] (b) Proton migration only within the electrolyte phase [5].**

In Figure 5.10 the polarization curve for the migration and diffusion model is compared with the migration only model. At a specific cell potential, the cell current density predicted by the migration and diffusion model is slightly lower than that of the migration only model. This deviation is not very large, and one can conclude that a reasonable prediction of the fuel cell overall performance can be obtained using simple models that ignore the proton diffusion phenomenon in the electrolyte. However, as discussed above, there are other phenomena for which the migration only model predicts results that are completely erroneous. The migration and diffusion model provides insight to fuel cell performance that goes beyond that provided by polarization curves.



**Figure 5.10. Modeling results for polarization curves of direct propane/oxygen fuel cells using a solid ZrP-PTFE electrolyte at 150°C. (a) Proton migration and diffusion within the electrolyte phase [the present model] (b) Proton migration only within the electrolyte phase [5].**

Concentration polarization, caused by liquid water will not exist in a DPFC as the cell operating temperature is far above the water boiling point. Therefore, activation overpotential and ohmic polarization are the sources of potential drop in a direct propane fuel cell. Any change in the operating conditions or cell design that results in a decrease in activation overpotential and

ohmic polarization will improve the cell performance. Figure 5.11 shows the performance of a DPFC predicted by the model at different operating temperatures. It also shows the performance of a hydrogen PEM fuel cell at 80°C [35] and that of a DPFC at 200°C having a phosphoric acid electrolyte [32]. As temperature is increased from 150°C to 230°C, the rate of reaction increases according to Eqs. (5-23) and (5-26). This leads to a decrease in the overpotential term in the Butler-Volmer equation and a major improvement in the cell performance. It can be concluded that a DPFC operating at 230°C has comparable performance to a hydrogen PEMFC at 80°C when both operate at low current densities less than 40 mA cm<sup>-2</sup>.

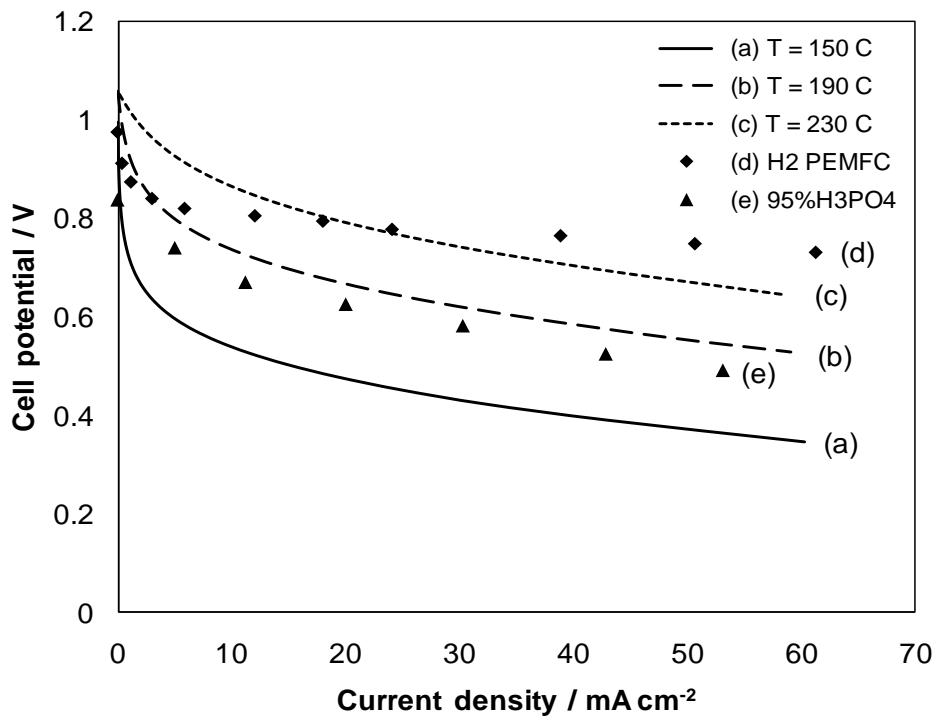


**Figure 5.11.** (a), (b) and (c) predicted polarization curves for a direct propane/oxygen fuel cell at different operating temperatures, (d) experimental data for a typical hydrogen/oxygen PEMFC [35], (e) experimental data for the best performed DPFC at 200°C [32].

Based on the results of the present model, the total flux of water moving from the anode to the cathode through the electrolyte phase is equal to that moving from the cathode to the anode through the electrolyte. This means that diffusion of each proton from the anode to the cathode drags one water molecule with it in the form of H<sub>3</sub>O<sup>+</sup>. During the diffusion of the two mobile species, an H<sub>3</sub>O<sup>+</sup> species will trade places with an H<sub>2</sub>O species. There is a balance in the

electrolyte phase of water molecules traveling as  $\text{H}_3\text{O}^+$  from the anode to the cathode and traveling as  $\text{H}_2\text{O}$  from the cathode to the anode. It can be concluded that water molecules are not transferred by diffusion from the electrolyte phase to the gas phase of the anode or cathode.

#### **5.4. Conclusions**

Proton and water transport in the electrolyte phase of a direct propane fuel cell was investigated using the concentrated solution theory and the Generalized Maxwell-Stefan (GMS) equations. The GMS equations permitted the development of a rigorous model that described the contributions of both diffusion and migration phenomena to proton transport within the electrolyte phase.

Ignoring the diffusion mechanism, as is done in simple models, leads to an incorrect overpotential distribution within the catalyst layers. This will result in an incorrect concentration profile for species in both the gas and the electrolyte phases. Although simple models can predict polarization curves correctly, they do not describe many of the phenomena in fuel cells. This reasoning is valid for all types of fuel cells.

The performance of DPFCs was shown to be similar to that of hydrogen fuel cells at certain conditions (low current densities and elevated temperatures). Although the operating temperature for the ZrP-PTFE membrane which has been developed in our research group is  $150^\circ\text{C}$ , the model prediction encourages improving the membrane so it will be suitable for higher temperatures up to  $230^\circ\text{C}$ .

#### **5.5. Acknowledgements**

Financial assistance is gratefully acknowledged: A Discovery Grant was awarded from the Canadian federal government's Natural Sciences and Engineering Research Council. A project within the Ontario Fuel Cell Research and Innovation Network (OFCRIN) was funded both by the Ontario provincial government's Ontario Research Fund and by the Network's industrial sponsors. One of us (H.K.) is grateful to the Ontario government for the award of Ontario Graduate Scholarships.

## 5.6. Nomenclature:

$A_{Pt}$ : platinum surface area per catalyst volume ( $m^2_{Pt} m^{-3}_{catalyst}$ )

$A_{CAT}$ : specific surface area of catalyst support (Vulcan carbon) in the anode and cathode  
( $m^2_{catalyst} kg^{-1}_{catalyst}$ )

[B]: matrix of inverted binary diffusion coefficients ( $s m^{-2}$ )

[B'] = [B]<sup>-1</sup>: inverse of the matrix of inverted binary diffusion coefficients ( $m^2 s^{-1}$ )

$c$ : molar concentration of mixture ( $kmol m^{-3}$ )

$c_i$ : molar concentration of species  $i$  ( $kmol m^{-3}$ )

$\vec{d}_i$ : generalized driving force for mass diffusion ( $m^{-1}$ )

$D_i$ : diffusion coefficient of species  $i$  in the gas mixture ( $m^2 s^{-1}$ )

$\mathcal{D}_i$ : diffusion coefficient of ion  $i$  in a solution ( $m^2 s^{-1}$ )

$D_{ij}$ : Fickian binary diffusion coefficient ( $m^2 s^{-1}$ )

$\mathcal{D}_{ij}$ : generalized Maxwell-Stefan diffusivities for the pair  $i-j$  in multicomponent mixture ( $m^2 s^{-1}$ )

$D_p$ : effective particle diameter ( $\mu m$ )

$F$ : Faraday's constant, 96485 ( $C kmol^{-1}_{charge}$ )

$\Delta G^\ddagger$ : activation energy for the exchange current density ( $kJ kmol^{-1}$ )

$j$ : volumetric current density; rate of production of proton in electrodes ( $A m^{-3}_{catalyst}$ )

$j^0$ : exchange current density at operating conditions ( $A m^{-2}_{Pt}$ )

$j^{0.ref}$ : reference exchange current density at the reference conditions ( $A m^{-2}_{Pt}$ )

$J$ : current density ( $mA cm^{-2}$ )

$\vec{J}_i$ : molar diffusion flux of species  $i$  with respect to  $n$ th component (solvent) velocity ( $kmol m^{-2} s^{-1}$ )

$L_w$ : land width in the flow field (mm)

$MW_i$ : molecular weight of species  $i$  ( $kg mol^{-1}$ )

$n$ : number of species

$p_i$ : partial pressure of species  $i$  (kPa)

$P$ : total pressure (kPa)

$R$ : universal gas constant, 8.314 ( $kJ kmol^{-1} K^{-1}$ )

$R_{PTFE}$ : electrical resistivity in membrane ( $\Omega m$ )

$T$ : temperature (K)

$Th$ : thickness of catalyst layers and membrane ( $\mu m$ )

$\vec{u}$ : superficial velocity of gas mixture (m/s)

$u_i$ : mobility of ion  $i$  in a solution ( $\text{cm}^2 \cdot \text{mol} / \text{J} \cdot \text{s}$ )

X: propane conversion (%)

x: Cartesian coordinate

y: Cartesian coordinate

$y_i$ : mole fraction of species  $i$  in the gas phase

$x_i$ : mole fraction of species  $i$  in the electrolyte phase

z: moles of transferred electrons in anode and cathode reactions ( $\text{kmol}_{\text{electrons}} \text{kmol}_{\text{propane}}^{-1}$ )

$z_i$ : charge number of species  $i$  ( $\text{kmol}_{\text{charge}} \text{kmol}_{\text{species}}^{-1}$ )

### Greek letters:

$\alpha_A$  and  $\alpha_C$ : anodic and cathodic charge transfer coefficients

$\varepsilon$ : volume fraction

$\eta$ : overpotential (V)

$\lambda$ : moles of water per mole of sulfonic acid sites

$\mu$ : dynamic viscosity ( $\text{kg m}^{-1} \text{s}^{-1}$ )

$\nu_i$ : stoichiometric coefficient of species  $i$ , positive for reactants and negative for products

$\rho$ : mass density ( $\text{kg m}^{-3}$ )

$\rho_{\text{CAT}}$ : apparent bulk density of catalyst support ( $\text{kg}_{\text{catalyst}} \text{m}^{-3}_{\text{catalyst}}$ )

$\sigma_{\text{ZrP/PTFE}}$ : ionic conductivity in membrane ( $\text{S m}^{-1}$ )

$\phi$ : electrical potential (V)

$\phi_{\text{Pt}}^{\text{EQ}}$ : equilibrium potential of catalyst phase (V)

$\phi_{\text{ELY}}^{\text{EQ}}$ : equilibrium potential of electrolyte phase (V)

### Subscripts and superscripts:

A: anode

C: cathode

C<sub>3</sub>: propane

C<sub>3</sub>Ox: propane oxidation reaction on Pt catalyst

ELY: electrolyte phase in the membrane, anode and cathode catalyst layers containing solid ZrP and mobile H<sub>2</sub>O and H<sup>+</sup>

EQ: equilibrium state

G: gas mixture

*i*: species in gas or solid phase; propane, water, CO<sub>2</sub>, O<sub>2</sub>, H<sup>+</sup> and ZrP

ML: membrane layer

O<sub>2</sub>Rd: oxygen reduction reaction on platinum catalyst

Pt: platinum catalyst

ref: reference conditions

ZrP: zirconium phosphate in the electrolyte phase

### **Abbreviations:**

FEM: finite element method

GMS: Generalized Maxwell-Stefan

MEA: membrane electrode assembly

MS: Maxwell-Stefan

PTFE: polytetrafluoroethylene

ZrP: zirconium phosphate

### **5.7. References**

[1] H.A. Liebhafsky, E.J. Cairns, The direct hydrocarbon fuel cell with aqueous electrolytes, In: Fuel Cells and Fuel Batteries, Wiley, New York, 1968, pp. 458-523.

[2] J.O. Bockris, S. Srinivasan, Fuel cells: their electrochemistry, In: Electrochemical Combustion of Organic Substances, McGraw-Hill, New York, 1969, pp. 357-411.

[3] E.J. Cairns, The anodic oxidation of hydrocarbons and the hydrocarbon fuel cell, Adv Electrochem and Electrochem Eng, 8 (1971) 337-391.

[4] A.Z. Weber, J. Newman, Modeling Transport in Polymer-Electrolyte Fuel Cells, 104 (2004) 4679-4726.

[5] H. Khakdaman, Y. Bourgault, M. Ternan, Computational modeling of a direct propane fuel cell, J.Power Sources, 196 (2011) 3186-3194.

[6] E. Carcadea, H. Ene, D.B. Ingham, R. Lazar, L. Ma, M. Pourkashanian, I. Stefanescu, Numerical simulation of mass and charge transfer for a PEM fuel cell, Int.Communicat. Heat Mass Transf., 32 (2005) 1273-1280.

- [7] D. Cheddle, N. Munroe, Parametric model of an intermediate temperature PEMFC, *J.Power Sources*, 156 (2006) 414-423.
- [8] S. Um, C.Y. Wang, Three-dimensional analysis of transport and electrochemical reactions in polymer electrolyte fuel cells, *J.Power Sources*, 125 (2004) 40-51.
- [9] J.C. Amphlett, R.M. Baumert, R.F. Mann, B.A. Peppley, P.R. Roberge, T.J. Harris, Performance modeling of the Ballard Mark IV solid polymer electrolyte fuel cell I. Mechanistic model development, *J.Electrochem.Soc.*, 142 (1995) 1-8.
- [10] J.J. Baschuk, X. Li, Modeling of ion and water transport in the polymer electrolyte membrane of PEM fuel cells, *Int J Hydrogen Energy*, 35 (2010) 5095-5103.
- [11] J. Fimrite, B. Carnes, H. Struchtrup, N. Djilali, Transport phenomena in polymer electrolyte membranes II. Binary friction membrane model, *J.Electrochem.Soc.*, 152 (2005) A1815-A1823.
- [12] M. Wöhr, K. Bolwin, W. Schnurnberger, M. Fischer, W. Neubrand, G. Eigenberger, Dynamic modelling and simulation of a polymer membrane fuel cell including mass transport limitation, *Int J Hydrogen Energy*, 23 (1998) 213-218.
- [13] J.J. Baschuk, X. Li, A comprehensive, consistent and systematic mathematical model of PEM fuel cells, *Appl.Energy*, 86 (2009) 181-193.
- [14] R. Krishna, Diffusion in multicomponent electrolyte systems, *The Chemical Engineering Journal*, 35 (1987) 19-24.
- [15] T. Berning, D.M. Lu, N. Djilali, Three-dimensional computational analysis of transport phenomena in a PEM fuel cell, *J.Power Sources*, 106 (2002) 284-294.
- [16] J.J. Baschuk, X. Li, Modelling of polymer electrolyte membrane fuel cells with variable degrees of water flooding, *J.Power Sources*, 86 (2000) 181-196.
- [17] S. Um, C. Wang, K.S. Chen, Computational fluid dynamics modeling of proton exchange membrane fuel cells, *J.Electrochem.Soc.*, 147 (2000) 4485-4493.
- [18] M.W. Verbrugge, R.F. Hill, Ion and solvent transport in ion-exchange membranes. I. A macrohomogeneous mathematical model, *J.Electrochem.Soc.*, 137 (1990) 886-893.
- [19] A.Z. Weber, J. Newman, Transport in polymer-electrolyte membranes: II. Mathematical model, *J.Electrochem.Soc.*, 151 (2004).
- [20] C. Ziegler, H.M. Yu, J.O. Schumacher, Two-phase dynamic modeling of PEMFCs and simulation of cyclo-voltammograms, *J.Electrochem.Soc.*, 152 (2005) A1555-A1567.
- [21] A.Z. Weber, J. Newman, Effects of microporous layers in polymer electrolyte fuel cells, *J.Electrochem.Soc.*, 152 (2005) A677-A688.

- [22] J. Newman, K.E. Thomas-Alyea, *Electrochemical Systems*, 3rd ed., Wiley-Interscience, New Jersey, USA; 2004, pp. 271 to 315.
- [23] T.F. Fuller, J. Newman, Water and thermal management in solid-polymer-electrolyte fuel cells, *J.Electrochem.Soc.*, 140 (1993) 1218-1225.
- [24] A. Al-Othman, A.Y. Tremblay, W. Pell, S. Letaief, T.J. Burchell, B.A. Peppley, M. Ternan, Zirconium phosphate as the proton conducting material in direct hydrocarbon polymer electrolyte membrane fuel cells operating above the boiling point of water, *J.Power Sources*, 195 (2010) 2520-2525.
- [25] Y.I. Park, J.D. Kim, M. Nagi, High proton conductivity in ZrP-PTFE composites, *J. Mater. Sci. Lett.*, 19 (2000) 1735-1738.
- [26] R. Taylor, R. Krishna, *Multicomponent Mass Transfer*, Wiley, NY; 1993, pp. 24, 28 and 67.
- [27] F. Hecht, O. Pironneau, A. LeHyaric, K. Ohtsuka, FreeFEM<sup>++</sup> Version 3.12. Available at: <http://www.freefem.org/ff++/index.htm>, 2011.
- [28] ParaView 3.9- Open Source Scientific Visualization. Available at: <http://www.paraview.org/>, 2011.
- [29] S. Sang, Q. Wu, K. Huang, Preparation of zirconium phosphate (ZrP)/Nafion1135 composite membrane and H<sup>+</sup>/VO<sub>2</sub><sup>+</sup> transfer property investigation, *J.Membr.Sci.; J.Membr.Sci.*, 305 (2007) 118-124.
- [30] G. Psfogiannakis, Y. Bourgault, B.E. Conway, M. Ternan, Mathematical model for a direct propane phosphoric acid fuel cell, *J.Appl.Electrochem.*, 36 (2006) 115-130.
- [31] O. Savadogo, F.J. Rodriguez Varela, Low-temperature direct propane polymer electrolyte membranes fuel cell (DPFC), *J.New Mater.Electrochem.Syst.*, 4 (2001) 93-97.
- [32] W.T. Grubb, C.J. Michalske, A high performance propane fuel cell operating in the temperature range of 150-200°C, *J. Electrochem. Soc.*, 111 (1964) 1015-1019.
- [33] W. Vielstich, A. Lamm, H.A. Gasteiger (Eds.), *Handbook of Fuel Cells*, Wiley, England, 2003.
- [34] D. Dobos, *Electrochemical data : a handbook for electrochemists in industry and universities*, Elsevier, New York; 1975, pp. 339.
- [35] C. Tori, M. Baleztina, C. Peralta, R. Calzada, E. Jorge, D. Barsellini, G. Garaventa, A. Visintin, W.E. Triaca, Advances in the development of a hydrogen/oxygen PEM fuel cell stack, *Int J Hydrogen Energy*, 33 (2008) 3588-3591.

## CHAPTER 6

---

### GLOBAL SUMMARY AND ANALYSIS

This chapter integrates the material addressed in the three publications presented in Chapters 3, 4 and 5, and illustrates how the primary objective was met.

The principal objective of this dissertation was to identify parameters that would improve the performance of direct propane fuel cells by taking the advantages of computational analysis. A rigorous mathematical model was created to investigate the effect of the main parameters, including operating conditions, engineering design, and material, on the DPFCs' performance. This model was developed in three stages which are described in sections 6.1 to 6.3. Each stage has its own objectives supporting the principal goal of the research.

#### 6.1. Model for the Anode

Several phenomena affect the maximum power that can be generated by a fuel cell. Two of the most important phenomena are the rates of reaction at the anode catalyst layer and at the cathode catalyst layer. They control the rate of proton generation and consumption. The cathodic reaction in a DPFC, which is oxygen or air reduction, is similar to that in a hydrogen fuel cell. Hence, the anodic reaction, the slow rate of propane oxidation, is responsible for the poor performance of DPFCs. As a consequence, the rate of the anodic reaction in a DPFC needs to be improved in order to enhance the overall cell performance.

In order to improve the reaction rate at the anode catalyst layer some ideas were proposed including (i) operation at a temperature range that is higher than the conventional temperatures used for PEM fuel cells, 70-85°C; (ii) employing zirconium phosphate (ZrP) as the electrolyte material instead of Nafion, a commercial electrolyte for PEM fuel cells; and (iii) using interdigitated flow fields instead of serpentine flow fields, that are often used.

Operating at high temperatures, within the range of 150°C to 200°C, would improve the anodic reaction rate because reaction kinetics become faster when the temperature is increased. Moreover, no liquid water is present at these temperatures so that gaseous propane can reach the catalyst sites without interference from a liquid phase diffusion layer.

A necessary requirement for operation at high temperatures is to employ electrolyte materials, such as ZrP, which poses an acceptable proton conductivity at high temperatures. The proton conductivity of Nafion is significantly affected by the level of water content and declines substantially as the temperature is increased toward the boiling point of water.

Finally, the anodic rate of reaction is a linear function of the propane partial pressure. Thus, maintaining the partial pressure of the propane at the maximum possible value (inlet partial pressure) will be beneficial. This can be done by using interdigitated flow fields to distribute propane throughout the anode catalyst layer and to collect products from the anode catalyst layer. As a result, the concentration of reactants remains constant along the length of the feedstock channel. In contrast, in the conventional serpentine flow fields, reactants diffuse from the feedstock channel to the catalyst layer and products return from the catalyst layer to the same feedstock channel. Therefore, partial pressures of reactants in the feedstock channel decrease along the length of the feedstock channel.

An isothermal mathematical model for the anode catalyst layer was developed during the first stage of the work. Other parts of the fuel cell, i.e., cathode catalyst layer and the membrane layer were not considered in this preliminary model. The specific objective was to investigate possible improvement in the anodic reaction rate without dealing with a mathematically complex model for the whole fuel cell. The outcome of this step was expected to indicate whether or not DPFCs could be improved in comparison with hydrogen fuel cells.

There are three coexisting phases in the anode catalyst layer. They are the "gas phase" containing reactants and products, the "solid catalyst phase" containing the carbon support and platinum, and the "solid electrolyte phase". The later consists of stationary ZrP containing mobile H<sub>2</sub>O and H<sup>+</sup> that can be transferred. The governing equations were developed to represent the physical

behaviour of the anode catalyst layer. More specifically, these equations were developed for the "gas phase" and the "solid electrolyte phase". Electron transport in the "solid catalyst phase" was assumed to be infinitely fast by giving the electrical potential within this phase a constant value. Finally, the model is isothermal, and heat transfer effects were not included.

There are two possible approaches to model the "solid electrolyte phase", i.e., simple approach and rigorous approach. The former has been used in the vast majority of fuel cell models and was also used in this model of the electrolyte phase. In this approach, species transport in the electrolyte phase is described by migration phenomenon only. In other words, electrically charged species such as protons move in the electrolyte phase in response to an electric field (i.e. an electrical potential gradient).

The anode model predicted a lower anodic overpotential compared to previously published DPFC results. Indeed, a lower anodic overpotential results in a higher cell potential. This improvement was due to the modifications, including different reaction conditions (100% gas phase at 150°C), a different electrolyte material (ZrP), and a different type of flow fields (interdigitated).

In summary, the results showed that a major improvement in the anodic reaction rate is attainable by applying the above mentioned modifications. The conclusion was that the proposed modified DPFC could be promising as an alternative to hydrogen fuel cells. This investigation was published in a journal paper presented in Chapter 3.

## **6.2. Fuel Cell Model, Simple Approach**

In the second stage of the work, the anode model, described in section 6.1, was expanded to include the entire fuel cell including the three sub-domains, i.e., the anode catalyst layer, the cathode catalyst layer and the membrane layer. Three specific objectives for this development were: to predict the performance of an isothermal DPFCs at different operating conditions, to conduct parametric studies, and to develop a mathematical procedure for sub-domain coupling.

A comparison of polarization curves, plots showing cell potential as a function of electrical current density, is one criterion for assessing fuel cell performance. To perform this evaluation, the whole fuel cell has to be modeled. It must include the anode catalyst layer, the cathode catalyst layer and the membrane layer. In this work, the assessment was done at different operating conditions.

In addition to the examination of the fuel cell polarization curves, parametric studies can also be performed by using a fuel cell model in order to optimize desirable variables. The effects of independent variables (such as flow field dimensions and temperature) on key dependent variables (such as power generated by the fuel cell and reactant conversion) were investigated.

Finally, a general mathematical procedure was required for coupling sub-domains. The "solid electrolyte phase" is present in the anode catalyst layer, the membrane layer, and the cathode catalyst layer. In order to calculate a continuous profile for dependent variables in the solid electrolyte phase, a method had to be developed to couple the anode catalyst layer to the membrane layer, and the membrane layer to the cathode catalyst layer. This method had to satisfy an important constraint within the fuel cell. It had to force the amount of protons produced in the anode to be equal to those consumed in the cathode.

Governing equations and boundary conditions were developed for the anode and cathode catalyst layers and the membrane layer. There were three phases in the cathode catalyst layer which were similar to those already explained in section 6.1 for the anode catalyst layer. The membrane layer consisted of polytetrafluoroethylene (PTFE) as membrane support and ZrP as electrolyte material. Consistent with the previous stage of the work, the simple approach was used to model transport in the solid electrolyte phase throughout the whole fuel cell.

The model, that was developed during this stage of the work, was able to predict polarization curves for a DPFC having interdigitated flow fields, a ZrP-PTFE electrolyte, and an operating temperature of 150°C. As there were no experimental data for such a DPFC, the model results were compared to published data for DPFCs with other types of electrolytes and flow fields. The reasonable agreement of the polarization curves indicated that (i) the simple model could be used

for overall evaluation of the DPFCs, when polarization curve prediction was the criterion for the validity of the model, and (ii) the mathematical approach to couple the sub-domains was successful. The results pertinent to this research were published in a journal paper presented in Chapter 4.

It is desirable to decrease the propane concentration in the outlet stream of the direct propane fuel cells as much as possible. The unconverted propane at the outlet stream cannot be released in the environment where the fuel cell is used. In Chapter 4, it was also shown that the propane concentration in the outlet stream of the fuel cell could be controlled by using interdigitated flow-fields. Using this type of flow-fields, it is possible to choose the residence time by adjusting the distance between the feedstock channels and the product channels so that propane conversion can approach 100%.

Although the simple model could predict the polarization curves, it was not able to correctly calculate other important variables (overpotential and electrical potential gradient in the electrolyte phase). This issue also was discussed in Chapter 4. The reason was attributed to the representation of proton transport by proton migration only and the absence of proton diffusion. Therefore, a more rigorous model that accounted for the proton diffusion phenomena was developed in the last step of the work.

The problems discussed in Chapter 4 (the second paper) as the result of migration only model do not affect polarization curves. Since Chapter 3 (the first paper) did not discuss anything other than polarization curves, the problems identified in Chapter 4 did not have any impact on Chapter 3.

### **6.3. Fuel Cell Model, Rigorous Approach**

The simple model, which was described in section 6.2, was able to predict the overall performance of DPFCs such as polarization curves. However, as shown in Chapter 4, the simple model was erroneous in prediction of some important variables within the cell such as potential gradient and overpotential profiles. The reason for this deviation was attributed to the limitation of the simple models in describing the species transport in the electrolyte phase. In a more

comprehensive model, the transport of ionic species was described in response to both the electrical potential gradient and the concentration gradient. The specific objective for this stage of the work was to successfully predict the variation of all the desired variables within the fuel cell.

A rigorous approach was employed in order to account for both driving forces involved in proton and water transport in the proton conductor phase, i.e., electrical potential gradient and proton concentration gradient. In this approach, concentrated solution theory was applied by using the generalized Stefan-Maxwell equations. An isothermal model was developed and the results presented in Chapter 5 were submitted to a journal for publication.

The results of the rigorous model showed that protons are driven from the cathode to the anode as a result of electrical potential gradient (Figure 6.1) and from the anode to the cathode as a result of proton concentration gradient (Figure 6.2). The net proton flux is influenced by both electrical potential gradient and proton concentration gradient which is shown in Figure 6.3. It can be concluded that the proton flux in the electrolyte phase caused by the proton concentration gradient was greater than that caused by the electrical potential gradient. Moreover, the proton flux caused by the electrical potential gradient predicted by the simple models was opposite to the direction known to be correct. Therefore, the electrical potential profile and consequently the overpotential profile in the simple model were incorrect. As the rate of anodic and cathodic reactions are exponential functions of overpotential, a small deviation in overpotential can cause substantial error in the rate of reactions. Consequently, the conversion of propane and oxygen calculated by the simple model had a significant error.

The rigorous model was used to predict polarization curves and to conduct parametric studies for DPFC having interdigitated flow fields and ZrP-PTFE electrolyte. At low current densities, the performance of DPFCs at 230°C was shown to be similar to that of hydrogen fuel cells. The improvement in fuel cell potential at low current densities indicated that the activation overpotential had decreased significantly. However, the potential loss due to the ohmic resistance of the electrolyte phase will have to be decreased if further improvement in DPFC performance is to be achieved. In other words, DPFCs would be competitive if a membrane with acceptable conductivity at high temperatures (230°C) could be developed.

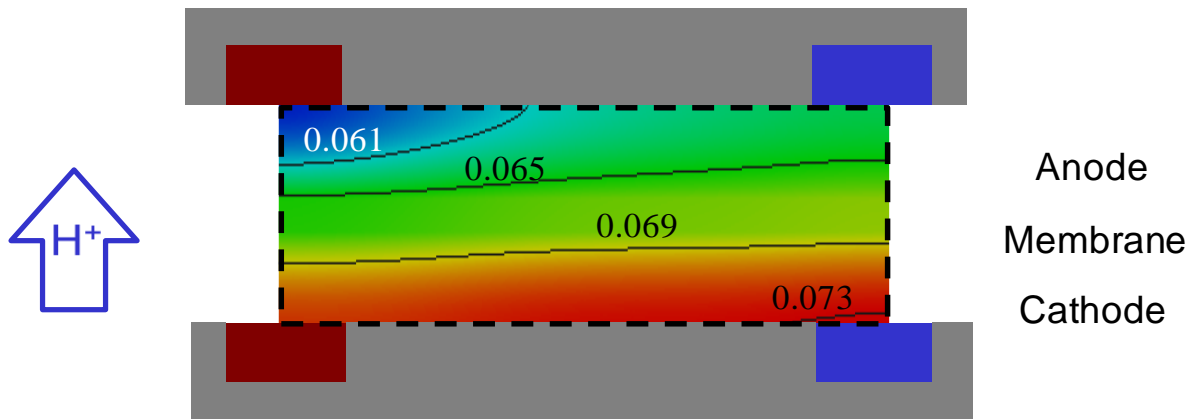


Figure 6.1. electrical potential gradient (V), higher at the cathode.

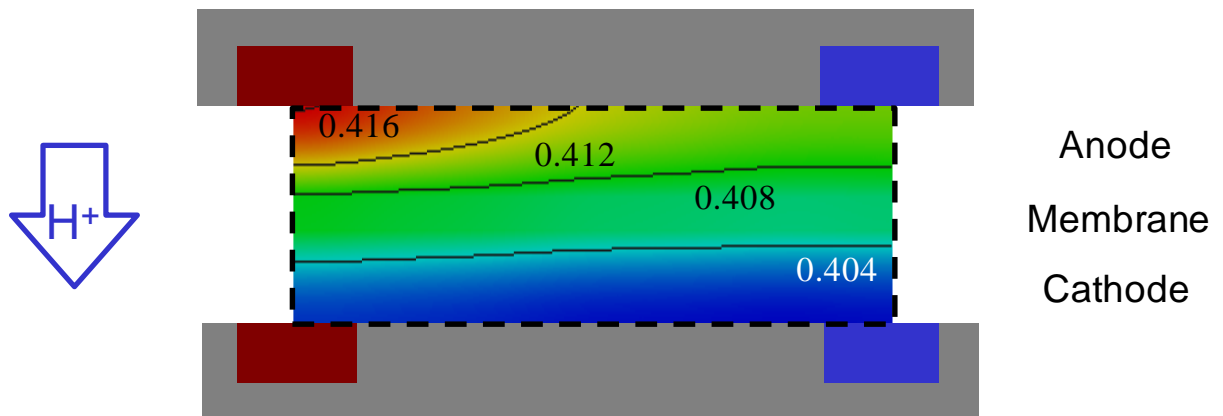


Figure 6.2. proton concentration gradient (mole fraction), higher at the anode.

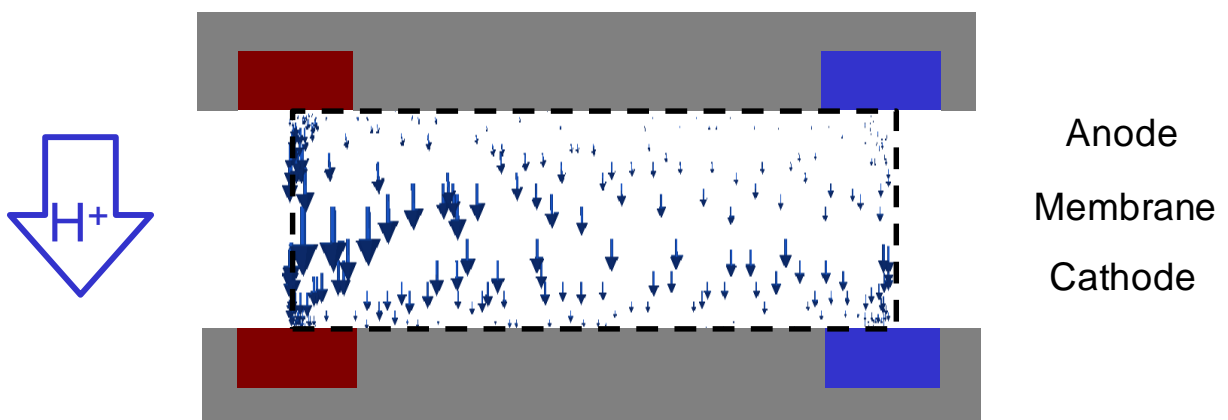


Figure 6.3. net proton flux from the anode to the cathode influenced by both electrical potential gradient and proton concentration gradient

## CHAPTER 7

---

### CONCLUDING REMARKS

This research focused on the development of a computational tool to assess the performance of direct propane fuel cells as a possible alternative to hydrogen fuel cells. Two isothermal mathematical models were developed from conservation principles and constitutive equations. The systems of equations were solved numerically by implementing a finite element method in FreeFEM<sup>++</sup> software. For this implementation, developing code in C<sup>++</sup> and using the existing library of C<sup>++</sup> classes and tools in FreeFem<sup>++</sup> were required. Model validation was performed using the experimental data which were available in the literature for DPFCs having different types of electrolyte materials. Results generated by the models illustrated how the various transport mechanisms occurring within the electrolyte phase influenced the model predictions. Some parametric studies were conducted to propose operating conditions and equipment design parameters that would lead to an improved performance for DPFCs.

Details of the investigations were presented in journal papers in the previous chapters. Section 7.1 highlights the most important findings of these investigations. Section 7.2 underscores the major contributions made in each paper. Section 7.3 provides a list of research topics that are suggested for further improvements in the present models and better understanding of DPFCs.

#### 7.1. Conclusions

The main conclusions from the dissertation are summarized below.

1- It was shown that the performance of a DPFC could be equivalent to that of a hydrogen fuel cell operating at 30 mA/cm<sup>2</sup>. This performance was predicted for a DPFC having a ZrP-PTFE composite membrane with a proton conductivity of 0.05 S/cm, interdigitated flow fields with a land width of 4mm and perating conditions of 230°C and 1 atm.

2- Both migration and diffusion phenomena contribute to proton transport in the electrolyte phase. Therefore, both of them must be considered to correctly calculate the distribution of electrical potential and overpotential in the electrolyte phase of the electrodes.

3- A simple model which considers only the migration phenomenon as the mechanism of proton transport can predict the polarization curve with an acceptable accuracy.

4- A large fuel utilization at the anode (approximately 100% propane conversion) can be achieved by using interdigitated flow fields and adjusting its land width. Hence, a major concern about direct hydrocarbon fuel cells, that of the emission of unconverted fuel at the user's site, was addressed by employing interdigitated flow fields.

5- Acceptable pressure drops (0.1 kPa/mm) in the fuel cells equipped with interdigitated flow fields can be obtained by increasing the thickness of the catalyst layer. High pressure drop is considered to be a drawback for interdigitated flow fields.

6- Increasing land width leads to a minor negative effect on the DPFC's polarization curve.

7- The combination of two factors, an operating temperature greater than 150°C and an electrolyte material (ZrP-PTFE) that would conduct protons at these temperatures, eliminated the presence of water in the liquid phase. The absence of liquid phase water leads to less severe corrosion. That makes the use of non-precious metal catalysts possible. Specifically, the platinum anode catalyst can probably be replaced by a nickel catalyst.

8- The present model can be used to design a preliminary DPFC having interdigitated flow fields and ZrP-PTFE electrolyte.

9- In order to make the performance of DPFCs equivalent to that of hydrogen fuel cells at high current densities (beyond 30 mA/cm<sup>2</sup>), it will be necessary to develop a membrane with a higher proton conductivity than the ZrP-PTFE membrane used here.

## 7.2. Contribution to Knowledge

A summary of original contributions to knowledge is presented in this section:

- 1- The first two-dimensional model for an anode catalyst layer of a DPFC was developed (Chapter 3).
- 2- The combination of specific operating conditions (150°C, 1 atm, 0.0186 cm<sup>3</sup>/sec propane per feed channel), engineering design (interdigitated flow field with a land width of 10 mm and catalyst thickness of 400µm), and materials (ZrP-PTFE membrane having a proton conductivity of 0.04 S/cm, and Pt/C catalyst with 41.4 m<sup>2</sup>Pt/cm<sup>3</sup> catalyst) predicted a major improvement in the DPFC's performance. This improvement was caused by the predicted decrease in the anode overpotential, when compared to published data for DPFCs (Chapter 3).
- 3- The proposed flow-fields (interdigitated) permitted the dimension of the reaction zone, that is the distance between the feed channels and product channels, to be adjusted. It was shown that with suitable adjustments a 98% propane conversion was obtained (Chapter 3).
- 4- The first two-dimensional model for a DPFC was developed. Like the vast majority of fuel cell models, migration was the only mechanism of transport for charged species. This model neglected diffusion of charged species in the electrolyte phase. (Chapter 4).
- 5- A unique mathematical approach was developed. Three sub-domains were coupled within the main domain in such a way that the flux of specific variables at the exterior boundaries was zero. This approach is applicable to all types of fuel cells (Chapter 4).
- 6- The first rigorous mathematical model for a DPFC was developed in which both diffusion and migration phenomena were combined as the mechanisms of charged species transport in the electrolyte phase. The Generalized Stefan-Maxwell equations were used to account for both migration and diffusion phenomena within the electrolyte phase. Again, this method can be applied in all types of fuel cells (Chapter 5).

7- This is the first time that the results of the migration-only model and those of the rigorous model (diffusion plus migration) were compared. More importantly, some instructive calculated results were shown within the electrolyte phase, including the variations of proton concentration, electrical potential, overpotential, and net flux of protons. Most fuel cell models are simple models and cannot correctly calculate key variables such as electrical potential and overpotential within the electrolyte phase, and concentration of reactants in the gas phase of the catalyst layers. The model developed in this thesis overcomes those deficiencies (Chapter 5).

8- It was shown that a DPFCs' performance can be similar to hydrogen fuel cells at low current densities. More specifically, at low current densities, the power generated by a DPFC is close to that generated by a hydrogen fuel cell (Chapter 5).

### **7.3. Recommendations**

More research effort is required for direct propane fuel cells to become promising alternatives to hydrogen fuel cells. The following could be performed:

1- Experimental data should be produced by a DPFC having interdigitated flow fields and ZrP electrolyte. It is essential to tune the model using experimental data so that it predicts the dependent variables accurately.

2- The proton conductivity of the electrolyte material should be measured as a function of water content and temperature. Experimental measurements for diffusivity of water in ZrP-PTFE, and propane cross-over are also required to enhance the accuracy of the model results.

3- Heat balance calculations to design the coolant channels in the stack are required. In order to model a fuel cell stack composed of several direct propane fuel cells, a non-isothermal model is necessary. The reactions in the anode and cathode of a DPFC are endothermic and exothermic, respectively, yet the whole fuel cell generates heat. Thus, some part of the generated heat at the cathode of a fuel cell may be transferred to the anode of its adjacent fuel cell to be consumed at the endothermic anodic reaction. The excess heat has to be removed from the fuel cell stack.

4- In order to develop a more robust model especially at high current densities, it is recommended that the reaction term be solved implicitly.

## APPENDIX

---

To implement a partial differential equation (PDE) in FreeFEM software, it has to be written in variational form. Consider the following general equation and boundary conditions:

$$\frac{\partial u}{\partial t} - k \Delta u = 0 \quad \text{in } \Omega(0, t) \quad (1)$$

$$u(x, y, 0) = f(x) \quad \text{initial condition} \quad (2)$$

$$k \frac{\partial u}{\partial n} = f(u) \quad \text{boundary condition} \quad \text{on } \Gamma(0, t) \quad (3)$$

where,

$\Omega$ : modeling domain

$\Gamma$ : modeling boundary

$f(x)$ : arbitrary function

$k$ : constant

$n$ : normal direction

$t$ : time

$u$ : arbitrary variable, function of  $x$ ,  $y$ , and time

Variational formulation of equation (1) is shown in equation (4):

$$\int_{\Omega} u^n \omega \, dx \, dy - \int_{\Omega} u^{n-1} \omega \, dx \, dy + dt \int_{\Omega} k \nabla u^n \cdot \nabla \omega \, dx \, dy - \int_{\Gamma} f(u) \omega \, dx = 0 \quad (4)$$

where,

$u^n$ : value of  $u$  at time  $n$

$u^{n-1}$ : value of  $u$  at time  $n-1$

$\omega$ : test function

Two examples are presented in the following paragraphs in order to show how a PDE is written in variational form. The anode catalyst layer has been chosen for this purpose.

1- Conservation of momentum is solved by the linear term of the Ergun equation, Equation (5):

$$-\nabla P = 150 \left[ \frac{\mu_G (1-\varepsilon_G)^2}{D_p^2 \varepsilon_G^3} \right] \vec{\mathbf{u}} \quad (5)$$

Considering the constant coefficient  $150 \left[ \frac{\mu_G (1-\varepsilon_G)^2}{D_p^2 \varepsilon_G^3} \right]$  to be equal to  $K_{Ergun}$  results in Equation (6):

$$-\nabla P = K_{Ergun} \vec{\mathbf{u}} \quad (6)$$

Divergence of Equation (6) will result in:

$$-\nabla \cdot (\nabla P) = K_{Ergun} \nabla \cdot \vec{\mathbf{u}} \quad (7)$$

Divergence of velocity  $\nabla \cdot \vec{\mathbf{u}}$  can be calculated from the continuity equation, Equation (8):

$$\frac{\partial(\varepsilon_G \rho_G)}{\partial t} + \nabla \cdot (\varepsilon_G \rho_G \vec{\mathbf{u}}) + \sum_i^n \frac{\nu_i MW_i j}{zF} = 0 \quad (8)$$

$$\varepsilon_G \frac{\partial \rho_G}{\partial t} + \varepsilon_G \vec{\mathbf{u}} \cdot \nabla \rho_G + \varepsilon_G \rho_G \nabla \cdot \vec{\mathbf{u}} + \sum_i^n \frac{\nu_i MW_i j}{zF} = 0$$

$$\nabla \cdot \vec{\mathbf{u}} = \frac{1}{\varepsilon_G \rho_G} \left[ -\varepsilon_G \frac{\partial \rho_G}{\partial t} - \varepsilon_G \vec{\mathbf{u}} \cdot \nabla \rho_G - \sum_i^n \frac{\nu_i MW_i j}{zF} \right] \quad (9)$$

Combining Equations (7) and (9) results in:

$$-\Delta P = \frac{K_{Ergun}}{\rho_G} \left[ -\frac{\partial \rho_G}{\partial t} - \vec{u} \cdot \nabla \rho_G - \sum_i^n \frac{\nu_i MW_i j}{\varepsilon_G z F} \right] \quad (10)$$

$$-\Delta P = \frac{K_{Ergun}}{\rho_G} \left[ -\frac{\partial \rho_G}{\partial t} - \mathbf{u}_x \frac{\partial \rho_G}{\partial x} - \mathbf{u}_y \frac{\partial \rho_G}{\partial y} - \sum_i^n \frac{\nu_i MW_i j}{\varepsilon_G z F} \right] \quad (11)$$

Gas density is to be calculated by ideal gas law:

$$\rho_G = PM/RT$$

Eq. 12 shows the variational form of Eq. 11:

$$\begin{aligned} \int_{\Omega} \left( \frac{\partial P}{\partial x} \frac{\partial \omega}{\partial x} + \frac{\partial P}{\partial y} \frac{\partial \omega}{\partial y} \right) dx dy &= - \int_{\Omega} \left( \frac{K_{Ergun}}{\rho_G^{n-1}} \right) \left( \frac{\rho_G^n - \rho_G^{n-1}}{dt} \right) \omega dx dy \\ &- \int_{\Omega} \left( \frac{K_{Ergun}}{\rho_G^n} \right) \left( \mathbf{u}_x \frac{\partial \rho_G}{\partial x} + \mathbf{u}_y \frac{\partial \rho_G}{\partial y} \right) \omega dx dy \\ &- \left( \frac{K_{Ergun}}{\rho_G^n} \right) \left( \frac{MW_P j}{1000 \varepsilon_G z F} + \frac{6MW_{H2O} j}{1000 \varepsilon_G z F} - \frac{3MW_{CO2} j}{1000 \varepsilon_G z F} \right) \omega dx dy \\ &+ \int_{\Gamma} \frac{\partial P}{\partial y} \omega dy \end{aligned} \quad (12)$$

- 2- Conservation of species (water and proton) in the electrolyte phase is expressed by Equations (13) and (14).

$$-\nabla \cdot \left( c_{ELY} (B'_{H_2O-H_2O} - B'_{H_2O-H^+}) \nabla x_{H^+} \right) + \nabla \cdot \left( c_{ELY} B'_{H_2O-H^+} \frac{F x_{H^+}}{RT} \nabla \phi_{ELY} \right) - \frac{j}{zF} = 0 \quad (13)$$

$$\nabla \cdot \left( c_{ELY} (B'_{H^+-H^+} - B'_{H^+-H_2O}) \nabla x_{H^+} \right) + \nabla \cdot \left( c_{ELY} B'_{H^+-H^+} \frac{F x_{H^+}}{RT} \nabla \phi_{ELY} \right) + \frac{j}{zF} = 0 \quad (14)$$

Using the format in Equation (4), variational form of Equations (13) and (14) could be written as Equations (15) and (16), respectively:

$$\begin{aligned} & \int_{\Omega} \frac{c_{ELY} F}{RT} \phi_{ELY}^n \omega \, dx \, dy \\ & - \int_{\Omega} \frac{c_{ELY} F}{RT} \phi_{ELY}^{n-1} \omega \, dx \, dy \\ & + dt \int_{\Omega} c_{ELY} (B'_{H_2O-H_2O} - B'_{H_2O-H^+}) \left( \frac{\partial x_{H^+}^n}{\partial x} \frac{\partial \omega}{\partial x} + \frac{\partial x_{H^+}^n}{\partial y} \frac{\partial \omega}{\partial y} \right) dx \, dy \\ & - dt \int_{\Omega} c_{ELY} B'_{H_2O-H^+} \frac{F x_{H^+}}{RT} \left( \frac{\partial \phi_{ELY}^n}{\partial x} \frac{\partial \omega}{\partial x} + \frac{\partial \phi_{ELY}^n}{\partial y} \frac{\partial \omega}{\partial y} \right) dx \, dy \\ & - dt \int_{\Omega} \frac{j}{zF} \omega \, dx \, dy - \int_{\Gamma} f(u) \omega \, dx = 0 \end{aligned} \quad (15)$$

$$\begin{aligned} & \int_{\Omega} \frac{c_{ELY} F}{RT} x_{H^+}^n \omega \, dx \, dy \\ & - \int_{\Omega} \frac{c_{ELY} F}{RT} x_{H^+}^{n-1} \omega \, dx \, dy \\ & + dt \int_{\Omega} c_{ELY} (B'_{H^+-H^+} - B'_{H^+-H_2O}) \left( \frac{\partial x_{H^+}^n}{\partial x} \frac{\partial \omega}{\partial x} + \frac{\partial x_{H^+}^n}{\partial y} \frac{\partial \omega}{\partial y} \right) dx \, dy \\ & - dt \int_{\Omega} c_{ELY} B'_{H^+-H^+} \frac{F x_{H^+}}{RT} \left( \frac{\partial \phi_{ELY}^n}{\partial x} \frac{\partial \omega}{\partial x} + \frac{\partial \phi_{ELY}^n}{\partial y} \frac{\partial \omega}{\partial y} \right) dx \, dy \\ & + dt \int_{\Omega} \frac{j}{zF} \omega \, dx \, dy - \int_{\Gamma} f(u) \omega \, dx = 0 \end{aligned} \quad (16)$$